NTNU
Norwegian University of
Science and Technology

Press Form Hardening of Aluminium Alloys 7021 and 6082. A Feasibility Study.

Synnøve Krog

Materials Science and Engineering
Submission date: June 2016
Supervisor: Ola Jensrud, IMTE

Norwegian University of Science and Technology
Department of Materials Science and Engineering

Preface

This Master's thesis is submitted as the product of «TMT4905 – Materials Technology, Master's Thesis» in fulfillment of the degree Master of Science (MSc). The work was conducted at the Department of Materials Science and Engineering at the Norwegian University of Science and Technology (NTNU) throughout the 2016 spring semester.

The work is part of a larger industrial project by Raufoss Technology, aiming to develop an integrated hot forming and hardening process for aluminium called the press form hardening process. Hydro Aluminium, SINTEF and AP&T are partners in this project.

I thank my supervisor Ola Jensrud for guidance throughout this project, and Ketill Pedersen for participating in discussions and providing feedback. I wish to thank Vidar Hjelmen at the SINTEF Materials and Chemistry lab for conducting the high temperature formability experiments described in sections 3.3.3 and 3.2.1 together with me, for always providing help on short notice, and for working long hours to get my tests finished.

I also thank Terje Iveland and Ole Andersen at Hydro Aluminium Sunndalsøra for advice regarding testing with the Gleeble Thermal System and for conducting the experiments described in sections 3.2.2 and 3.4.3 together with me. Further, I would like to thank Trygve Lindahl Schanche for assistance in the mechanical laboratories, and Yingda Yu for assistance in the EM-laboratory.

Finally, I thank classmate Pål Rist for providing valuable help when my hard disk broke down beyond repair 48 hours before the deadline of this thesis.

Trondheim, December 2015

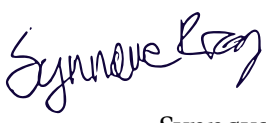

Synnøve Krog

Abstract

Aluminium alloys 6082.25 and 7021.50 were evaluated and compared as potential base materials for processing by press form hardening. Both extruded profiles and rolled sheets were assessed, however the rolled 7021 material was neglected early in the project due to time constraints. The effect of deformation at the relevant high temperatures and strain rates on the workability and microstructure of the materials was assessed. The artificial age hardening response subsequent to hot deformation was investigated for the 6082 rolled material.

The flow stress and workability of all investigated materials was highly favorable for forming at all temperatures relevant to press form hardening. These properties were *most* favorable at the solution heat treatment temperatures of the respective alloys. Materials that do not recrystallize during solution heat treatment appeared to give an advantageous grain structure in the finished parts. The extruded materials in this work did not recrystallize in bulk during solution heat treatment nor hot deformation, however recrystallization in the surface layers was not assessed. No disfavor of the fibrous grain structure associated with extruded materials was observed regarding workability at the relevant temperatures, thus extruded materials could be particularly suitable as base materials for press form hardening.

The AA7021.50 extruded material appeared especially suitable for press form hardening due to a particularly high workability and low flow stress at the relevant forming conditions. The superior resistance to recrystallization in this material further favored it as a suitable base material for press form hardening.

No detrimental effect of the hot deformation on the artificial ageing response was observed in the AA6082.25 rolled material. This should however be further and more thoroughly assessed for all potential base materials.

Sammendrag

Aluminiumslegeringene AA6082.25 og AA7021.50 ble evaluert og sammenlignet som potensielle grunnmaterialer for prosessering ved pressformherding. Både ekstruderte profiler og valsede plater ble undersøkt, men det valsede 7021 materialet ble nedprioritert tidlig i prosjektet grunnet tidsbegrensninger. Effekten av deformasjon ved de aktuelle høye temperaturene og tøyningshastighetene på formbarheten og mikrostrukturen til materialene ble undersøkt. Utherdingspotensialet etter varmdeformasjon ble undersøkt for det valsede 6082 materialet.

Flytemotstanden og formbarheten til alle de aktuelle materialene var veldig gunstige for forming på alle temperaturer og tøyningshastigheter relevant for pressformherding. Disse egenskapene var *best* ved innherdingstemperaturene til de respektive legeringene. Det ser ut som at materialer som ikke rekrystalliserer under innherding gir en ønsket kornstruktur i de ferdige delene. De ekstruderte materialene som ble vurdert i dette arbeidet, rekrystalliserte ikke i bulk under innherding; merk at overflatesjiktet ikke ble undersøkt. Ingen ulemper ved den fibrige kornstrukturen som assosieres med ekstruderte materialer ble observert for formbarheten på de relevante temperaturer og tøyningshastigheter, dermed kan ekstruderte materialer være spesielt egnede for prosessering ved pressformherding.

Det ekstruderte materialet av AA7021.50 virket spesielt egnet for pressformherding på grunn av spesielt høy formbarhet og lav flytemotstand ved de aktuelle forholdene. Den overlegne motstanden mot rekrystallisering i dette materialet fremstiller også materialet som ekstra egnet for pressformherding.

Varmdeformasjon hadde ikke en betydelig ødeleggende effekt på utherdingspotensialet for det valsede materialet av AA6082.25. Effekten av varmdeformasjon på den etterfølgende presipiteringsherdingen må likevel undersøkes grundigere for alle potensielle materialer.

Contents

1 Introduction

1.1 Background

In the process of developing more fuel efficient cars, making the cars lighter is essential. A weight reduction of 10% in a vehichle is estimated to lower the fuel consumption with as much as 8-10% [1]. Lowering the weight of a car may also provide additional advantages like increased performance during acceleration, increased lifetime of accelerating parts and increased safety and driving comfort due to lower unsprung mass [2, 3].

An important contribution to make cars lighter can be made by replacing more steel parts with high strength aluminium parts. It has been estimated that substitution of the steel parts that can be replaced by aluminium may reduce the total vehicle weight by 20-30% [1]. An additional advantage of using aluminium is that it is possible to recycle 85-95% of the spent material [4], and that recycling of aluminium requires little energy [5]. The use of aluminium in cars *is* increasing today [6], however, the growth is restrained as production processes for aluminium car parts today are not efficient enough to make them further competitive with the equivalent steel parts [1, 4].

The press form hardening process for sheet forming of aluminium was proposed by Lin et al. [7] in 2008 (commonly also called solution heat treatment and cold die quenching). This new process has the potential to overcome several challenges encountered in the traditional forming processes like low formability, springback, thermal distortion and poor geometric precision, thus providing more efficient production of aluminium car parts [8].

Several previous studies have assessed the different aspects of the press form hardening process [9–13]. In summary, the previous studies have concluded that this new process is indeed feasible. However, the process is not yet fully assessed and developed for implementation on an industrial scale [8].

1.2 Aim

In the present feasibility study, the materials in Table 1.1 will be evaluated and compared as potential base materials for the press form hardening process. Essential properties determining the suitability of the alloys for press form hardening will be investigated – that is the effect of deformation at relevant high temperatures and strain rates on:

- The formability and yielding behavior of the materials.
- The microstructure of the material.
- The precipitation potential during subsequent artificial age hardening.

The results will be assessed and combined in order to elucidate the most favorable material properties and corresponding process parameters for processing by press form hardening. The results will also elucidate the capability of the press form hardening technology.

As no standard test procedures or equipment was available, test methods were developed along the experimental work.

Table 1.1: Materials to be tested

AA6082.25	**AA7021.50**
Rolled sheet	Rolled sheet
Extruded profile	Extruded profile

2 Theory

In the following section, the relevant theory for understanding and interpretation of the results will be presented. As there is not much work done regarding the material response during the specific conditions relevant for press form hardening, the relevant mechanisms will mainly be presented in general terms.

2.1 Process route for sheet formed components

A variety of shapes and geometries can be produced by sheet forming of aluminium [14]. However, the traditional forming technologies are not effective enough to make formed sheet components in aluminium further competitive with the corresponding steel components in the automotive industry [1, 4]. The overall process route for producing sheet formed components from the 6xxx- and 7xxx series of aluminium alloys will be introduced in the present section, with special attention to important challenges in traditional sheet forming and how the proposed Press Form Hardening process overcomes these challenges. Further properties of the 6xxx- and 7xxx series of aluminium alloys will be presented later in sections 2.6 and 2.7.

2.1.1 Homogenization

During casting of the molten aluminium, both macro- and microsegregation of alloying elements occur. In addition, several different primary intermetallic particles commonly form.

After casting, the microsegregations are leveled out by a process called homogenization. During homogenization, the ingot or billet is heated to a temperature between 450°C and 600°C for a certain period of time [15, 16]. The increased diffusion rates at this temperature allow the concentration of alloying elements to level out, and consequently low melting point eutectics also dissolve. In addition, small particles called dispersoids precipitate [15, 16]. The homogenization process may also cause both structural and chemical changes of the primary intermetallic phases [15].

2.1.2 Production of sheet metal

Sheet metal may be produced from the cast aluminium amongst other by rolling or extrusion. Rolled sheets are typically produced by passing a piece of aluminum back and forth between two rolls that exert compressive stresses on the metal [17]. This is commonly done first at an enhanced temperature and subsequently at room temperature [18].

Extruded sheets are produced by forcing a piece of aluminium through a smaller die shaped as a sheet [17]. The thickness of the sheet may be varied along the cross section of the sheet by using a die with a more complex orifice. This alternating cross section cannot be achieved by rolling, thus extruded sheets are more flexible than rolled sheets regarding shape.

2.1.3 Precipitation hardening

The 6xxx- and 7xxx series aluminium alloys achieve strength and hardness through a heat treatment process called *precipitation hardening*. Further forming of the sheets may be integrated with this process.

The goal of the precipitation hardening process is to achieve strengthening precipitates finely dispersed in the aluminium matrix [19]. The process consists of three main steps: solution heat treatment, quenching and age hardening. In the solution heat treatment, the alloy is first heated to a specified temperature between the solidus and the solvus temperature, dependent on the alloying content. The alloy is held at this temperature long enough for all alloying elements to go into solid solution, giving one homogeneous phase [19].

When the alloy has been solution heat treated for the appropriate amount of time, the alloy is rapidly quenched to a temperature close to room temperature. The quenching prevents formation of equilibrium phases during cooling, thus keeping the alloying elements in solid solution down to room temperature. The alloy is then in a supersaturated state, optimal for the subsequent precipitation [19].

The final step in the precipitation hardening process is the artificial age hardening. In this step, the alloy is reheated to an intermediate temperature, typically between 115°C and 190°C [19]. This elevated temperature increases the diffusion rates and thus allow the alloying elements to form precipitates that significantly increase the strength of the material.

2.1.4 Traditional sheet forming

The forming operation is today mostly done by cold-forming [9]. Rolled sheets or extruded profiles are formed at room temperature between solution heat treatment and artificial ageing. The formability of aluminium at room temperature is limited, thus there are severe limitations to what geometries can be obtained. Springback further complicates the production process and obtainable geometries.

The challenges related to springback and formability can be overcome by doing the forming at an elevated temperature, i.e. hot-forming. However, the cooling rates during hot-forming are too low to keep the solid solution required for subsequent age hardening. Solution heat treatment and quenching are thus required after forming. The quenching often result in thermal distortion of the part, and the geometric precision of the part is consequently a challenge [11].

2.1.5 Sheet forming by press form hardening

Aiming to overcome the challenges above, an integrated forming and quenching process was first proposed by Lin et al. [7]. In this process, here called the press form hardening process (commonly also called solution heat treatment and cold die quenching), the aluminium sheet is first heated to the solution heat treatment temperature and kept there until solution heat treatment is complete. Then, water cooled dies simultaneously quench and form the sheet. The dies are kept closed until the part is cold [7]. Subsequently, the part is artificially age hardened.

Several previous studies have assessed the different aspects of this process. As the final shape of the part is set at hot-forming temperatures [9], high formability is expected in terms of both low flow stress and high ductility. This was confirmed in a feasibility study by Garrett et al. [10].

Consequently, springback is also significantly reduced. Fan et al. [11] found that if a further increase in formability is desired, the forming die temperature could be increased to 250°C without any observable decrease in strength for a 6A02 alloy.

Higher cooling rates after solution heat treatment give a more desirable state for the subsequent ageing [12]. Jensrud et al. [9] and [10] found that the quench rates during cooling with water cooled dies were higher than what is obtained with conventional water cooling. [10] also found that the quench rate can be tailored by altering the die pressure.

Thermal distortion is expected to be restricted as the dies maintain pressure on the part during cooling [13]. This was successfully demonstrated by Fan et al. [12].

These advantages suggests that the Press Form Hardening process provides the possibility to produce high quality components with complex geometries within narrow tolerances. The integrated heat treatment, quenching and forming allows cost- and energy effective production in addition to high productivity [8].

2.2 Mechanical properties

A challenge in replacing steel with aluminium in cars, is to obtain sufficiently strong aluminium components. In this section, some important strengthening mechanisms for the 6xxx- and 7xxx series aluminium alloys will be described.

In general, most metals deform plastically by movement of dislocations [14]. Impeding dislocation movement thus increase the yield strength and hardness of a metal. Important mechanisms for obstruction of dislocation movement will be described in this section.

2.2.1 Solid solution strengthening

Pure metals are always weaker than metals that contain another element in solid solution [14]. Several mechanisms contribute to the solid solution strengthening of aluminium, however the most important are the effects of differences in size and elastic modulus between the solute atoms and the atoms of the matrix [20].

The size difference between the solute atoms and the solvent atoms induces elastic stress fields around the solute atoms. These stress fields may interact with the elastic stress fields that surround dislocations and impede dislocation motion, thus increasing the strength of the material. The magnitude of this strengthening effect is directly proportional to the misfit of the solute atoms [14].

The difference in elastic modulus between the solvent and the solute atoms also contribute to strength. If a solute atom has a lower elastic shear modulus than the matrix, the energy of the elastic strain field surrounding a dislocation in the vicinity of this atom will be lower, thus there will be an attraction between the dislocation and the solute atom [14]. This opposes movement of the dislocation and thus contribute to increased strength.

2.2.2 Strengthening from precipitates and particles

As the 6xxx- and 7xxx series aluminium alloys are precipitation hardened, the strengthening from precipitates and particles are responsible for a considerable amount of the strength of the alloys. The strengthening effect from second phase particles is highly dependent on the distribution of these particles in the matrix. An important parameter regarding the particle distribution is the mean inter-particle spacing, λ, which in tu rn is dependent on the average radius (r) of the particles and the volume fraction of particles (f) according to equation 2.1 [14].

$$\lambda = \frac{4(1-f)r}{3f} \tag{2.1}$$

It can be seen from the equation that a high volume fraction of small particles give small inter-particle spacing. A low inter-particle spacing gives higher strength as the dislocation then would encounter a particle more often.

Shearable precipitates

Dislocation movement can be obstructed by second phase particles in two ways, depending on wether the particles are shearable or not [14]. Shearable precipitates act as coherent particles that allow the dislocations to pass through or cut them. Moving a dislocation through a particle requires a higher stress levels than moving the dislocation freely in the matrix, thus the strength of the material is enhanced [21].

There are several properties of a shearable precipitate that determines the stress required to cut it. For example, coherent precipitates may generate stress fields in the matrix (see Figure 2.1) that interact with the elastic stress fields that surround dislocations. This interaction induces forces that oppose dislocation motion, and thus increase the strength of the material.

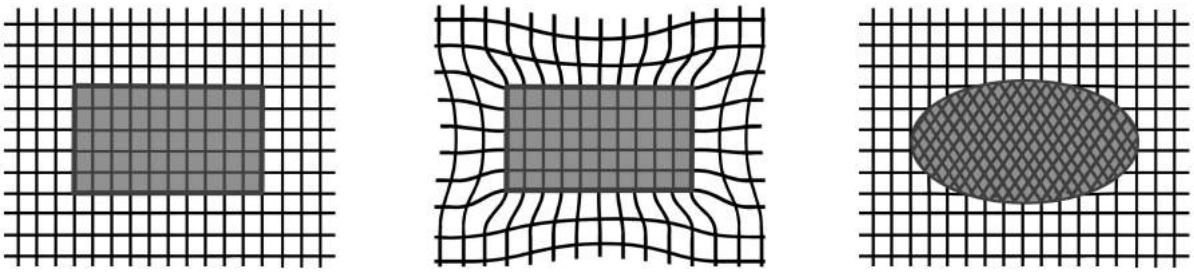

(a) Precipitate that is fully coherent with the matrix.

(b) Coherent precipitate with low coherency with the matrix.

(c) Precipitate that is non-coherent with the matrix.

Figure 2.1: Precipitates with varying degree of coherency with the matrix.

Another property that determines the strengthening effect of a shearable precipitate is the energy of the interface between the matrix and the particle [14]. If a dislocation cuts a precipitate, a step is created at the particle surface, see Figure 2.2. This increases the surface area of the particle, thus the surface energy also increases. For a dislocation to cut a particle, this energy must be supplied by the external stress [14], consequently the strength of the material is increased.

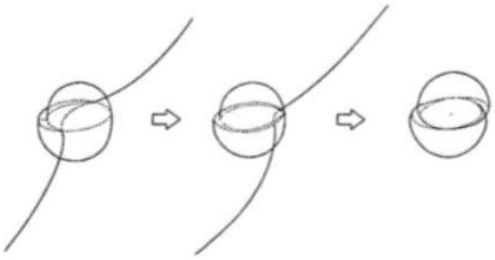

Figure 2.2: Dislocation cutting a shearable particle [22].

Unshearable precipitates

Unshearable precipitates are particles that the dislocations cannot cut, thus they are forced to move around them. In order to bypass these particles, the dislocations have to bend out between and around them. This requires higher stress than moving the dislocation unobstructed, and the strength of the material is consequently increased. The dislocations bend out between the particles and dislocation segments of opposite signs meet and annihilate on the other side of the particles. The original dislocation line is then free to move further, but a dislocation loop around the particle is left behind [14]. See Figure 2.3.

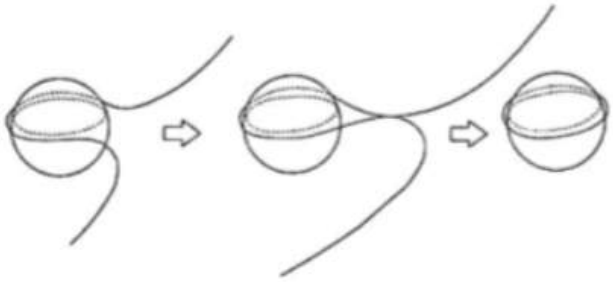

Figure 2.3: Dislocation passing around an unshearable particle [22].

Each dislocation passing by an unshearable particle leaves a dislocation loop around it [14]. As a consequence, plastic deformation leaves the particles surrounded by a collection of dislocation loops. These loops exert stresses on dislocation sources that must be overcome for additional slip to take place, and this further causes the material to strain harden [14].

2.2.3 Grain structure

As previously mentioned, impeding dislocation movement enhances the yield strength and hardness of a metal. Grain boundaries are another feature that obstruct movement of dislocations, thus the grain structure of a material has great influence on its strength.

In order to traverse across a grain boundary, a dislocation would have to change its direction of motion, as adjacent grains usually have different crystallographic directions. In addition, the grain boundaries are regions of atomic disorder, thus the slip planes are not continuous from grain to grain [17]. These factors restrain the dislocation movement from one grain to another. Dislocation movement across a grain boundary becomes increasingly difficult with increasing misalignment angle between the grains. However, plastic deformation may proceed from grain to grain even though the dislocations themselves cannot pass the boundary. Dislocations then pile up at the boundary rather than traversing across. These pile-ups induce stresses ahead of their slip plane, which may generate new, unobstructed dislocation in the neighbouring grains [17].

A small grain size corresponds to a high amount of grain boundaries available to impede dislocation motion [17]. In addition, small grains contain less dislocations than large ones, thus the pile-ups at the grain boundaries will be smaller in a fine grained material. The stress concentration ahead of the pile-up is proportional to the number of dislocations it contains [23]. Consequently, a fine grained material is stronger than a coarse grained material.

Moreover, a grain structure where a few grains are significantly larger than the rest may be detrimental to the mechanical properties of the material [24]. This will be further discussed in Section 2.3.5.

2.2.4 Anisotropy and texture

Most materials are anisotropic [25]. This means that they have distinctive properties in different directions. In contrast, a completely isotropic material would have equal properties in all directions.

Anisotropy occurs because most properties of one particular crystal are anisotropic. (For example, deformation of a single crystal is easier in directions that have a favorable orientation with the available slip systems.) For a polycrystalline material, the overall anisotropy will thus depend on how the grains that comprise the material are crystallographically oriented. The statistical distribution of these orientations is called the texture of the material. This distribution is not commonly random, thus few materials have random texture [25].

Anisotropy and texture may significantly influence the behavior of a material during deformation. Even weak textures may have great influence on how a material responds to stress in terms of plastic flow. If a material is weaker in one particular direction, applied stress may result in plastic flow only in this direction.

If a material has *planar* anisotropic properties, plastic flow will vary with direction in the rolling plane. This may be a challenge in forming operations as it could result in irregularities around the periphery of a formed part. *Normal* anisotropy is a difference in plastic flow between the thickness and the directions in the rolling plane. Normal anisotropy may improve resistance to thinning during sheet forming, and may thus be beneficial, depending on the forming operation [26].

2.3 Deformation and static restoration of grain structures

As previously stated, the grain structure influences the strength and mechanical properties of a metal (see Section 2.2.3). Both temperature and deformation affect the grain structure [27] and thus in turn also affect the strength of the material.

2.3.1 Cold deformation structures

Deformation of a metal affects the microstructure in several ways [27]. During deformation, the shape of the grains is changed in a manner corresponding to the macroscopic shape change [27]. Consequently, both extruded and rolled aluminium sheets typically have a microstructure where the grains are shaped as laths or needles along the extrusion or rolling direction.

Deformation of the metal also induce generation of dislocations, thus deformation results in an increased dislocation density in the material. As deformation continues, these dislocations interact with each other and arrange in patterns. In aluminium, this pattern consists of cells divided by walls of densely tangled dislocations. Increasing strain causes further entanglement, thus these cells are further partitioned and the cell size decreases towards a lower limit size. When the lower limit cell size is reached, further straining only increases the density and thickness of the tangles [28]. See Figure 2.4.

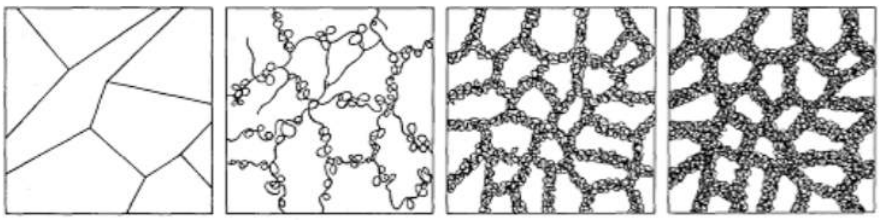

Figure 2.4: Development of the dislocation cell structure in aluminium.
From McQueen and McGregor Tegart [28].

The generation of dislocations stores some of the work applied through deformation as energy within the aluminium matrix. This storage of energy leaves the material in an energetically unstable state, even though the alloy is *mechanically* stable at room temperature and the microstructure thus remains unchanged until heat is applied [29].

2.3.2 Static recovery

At elevated temperatures, dislocations become more mobile, and the deformed structure is no longer mechanically stable. The energy stored in the material by deformation acts as a driving force for processes restoring the microstructure of the material. The mechanical properties of the alloy may change significantly throughout this process [29].

For aluminium, the first step in the restoration process is recovery. Due to the increased diffusion rates at elevated temperatures, the dislocations may climb or cross-glide to accommodate the forces they exert on each other. They may either annihilate (see Figure 2.5) or arrange in arrays that allow some cancelation their elastic distortions [28].

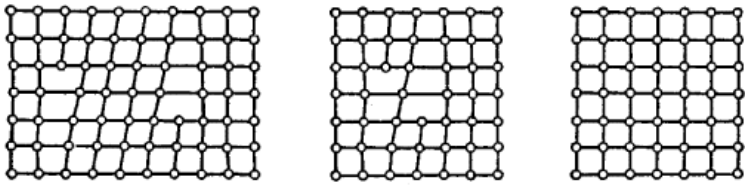

Figure 2.5: Annihilation of dislocations. From The Free Dictionary By Farlex [30].

These processes releases som of the energy stored in the material during deformation [27]. The dislocation tangles and rough dislocation cells introduced during deformation gradually changes into ordered arrays of dislocations or subgrains. Eventually the subgrains grow as some sub-boundaries combine [28]. See Figure 2.6. During recovery, the deformed grain structure is still preserved, but the dislocation density is significantly reduced [29].

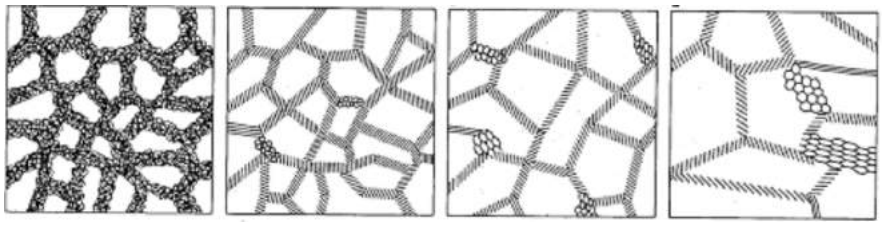

Figure 2.6: Development of the cell structure and subgrains in aluminium during recovery. From McQueen and McGregor Tegart [28].

2.3.3 Static recrystallization

The second step of the restoration process is recrystallization (i.e. primary recrystallization). After recovery, the remaining dislocation density is still higher than equilibrium values. This stored energy drives the recrystallization process [29]. During recrystallization, new, undeformed grains gradually replace the deformed microstructure. Recrystallization initiates as small crystallites of low internal energy appear. These are surrounded by high-angle grain boundaries, and as they grow and consume the adjacent grains by grain boundary migration the deformed microstructure is gradually replaced [27]. When these new grains touch, the material consists of undeformed grains with equilibrium dislocation density. The material is then fully recrystallized [29]. The temperature required for recrystallization of a deformed material is lowered with increasing degree of deformation [27].

2.3.4 The effect of second phase particles

The presence of second phase particles in a metal may strongly affects the recrystallization behavior. During deformation, areas of enhanced dislocation density typically form around the particles. Nucleation of recrystallized grains are promoted in these areas (particle stimulated nucleation, PSN), and the recrystallization process is thus promoted [27]. The presence of particles may also increase the general multiplication of dislocations in the material during deformation, and thus increase the overall driving force for recrystallization. Particle stimulated nucleation of recrystallized grains is most effective following deformation at room temperature [27]. If the deformation temperature is increased sufficiently, the dislocations are more mobile and may thus be able to bypass the particles without generating deformation zones.

On the other hand, second phase particles also tend to impede migration of grain boundaries by a mechanism called the *Zener drag* [27]. When a grain boundary intersects with a particle, the grain boundary area corresponding to the intersection area is removed. This reduces the energy of the boundary, thus the boundary is attracted to the particle and grain boundary migration is restricted. This may restrain the growth of recrystallized grains or nuclei, and may thus prevent

recrystallization. The magnitude of the Zener drag depends on the shape, size, spacing and volume fraction of the second phase particles in addition to the nature of the particle and the particle/matrix interface [27].

2.3.5 Normal and abnormal grain growth

When the grain structure of the material is restored, further annealing will result in either normal grain growth or abnormal grain growth (sometimes called secondary recrystallization). The driving force for grain growth is the decrease in the grain boundary energy accompanying the reduction of grain boundary area. During normal grain growth, many grains grow by consuming their neighboring grains by migration of high angle grain boundaries [29]. This results in a homogeneous grain structure with an increased average grain size.

Abnormal grain growth may happen if grain growth is obstructed for most, but not all grains [29]. During abnormal grain growth, a few grains experience a much higher growth rate than most grains. These grains thus grow excessively at the expense of the regular grains, and the resulting grain structure consists of some large grains in a matrix comprised of much smaller grains. This type of grain structure may be detrimental to the mechanical properties [24], thus abnormal grain growth is undesirable.

2.4 Anisotropy and texture

Most materials are anisotropic [25]. This means that they have distinctive properties in different directions. In contrast, a completely isotropic material would have equal properties in all directions. Anisotropy occurs because most properties of one particular crystal structure are anisotropic. (For example, deformation of a single crystal requires lower stress in directions that have a favorable orientation with the available slip systems.) For a polycrystalline material, the overall anisotropy will thus depend on how the grains that comprise the material are crystallographically oriented. The statistical distribution of these orientations is called the texture of the material. This distribution is not commonly random, thus few materials have random texture [25].

Anisotropy and texture may significantly influence the behavior of a material during forming. Even weak textures may greatly affect how a material respond to stress in terms of plastic flow. If a material has *planar* anisotropic properties, plastic flow will vary with direction in the rolling plane. This is a challenge in forming operations as it may lead to irregularities around the periphery of a formed part. *Normal* anisotropy is a difference in plastic flow between the thickness and the directions in the rolling plane. Normal anisotropy may improve a material's resistance to thinning during sheet forming, and may thus be beneficial depending on the forming operation [26].

The texture, and thus anisotropy of a material can be generated or changed by deformation. Subsequent recrystallization also tends to produce certain textures.

2.4.1 Texture evolution during deformation

Texture arise during deformation as there are a limited number of slip systems (or twinning systems) available to accommodate the plastic strains [26].

When stress is applied, the slip systems with the most favorable orientation with the direction of stress will be activated first. The resulting shape change of the crystal, in combination with

the geometrical constraints from the surroundings, induce a rotation of the crystal planes. The crystal planes tend to rotate towards certain orientations that can accommodate the strains more easily. This principle is shown for a monocrystalline sample in tensile tension in Figure 2.7.

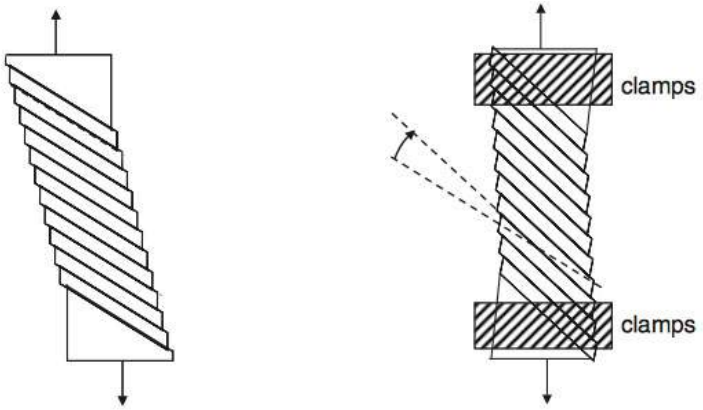

(a) Activation of most favorable slip system in an unconstrained single crystal

(b) Rotation of the crystal as geometrical constrains are introduced as clamps.

Figure 2.7: From Verlinden et al. [25]

In a polycrystalline material, the situation is more complex as each grain is constrained by all surrounding grains [25]. However, the principles remain the same.

The texture arising from deformation depend on the imposed stress, the degree of deformation and the activated deformation mechanisms [26].

2.4.2 Texture evolution during recrystallization

During recrystallization, nucleation of new grains with particular orientations occurs preferentially in regions that contain certain deformation features and orientations. Further, the ability of a nucleus to grow is affected by the orientation of the adjacent grains [27]. Consequently, recrystallization textures often relates in a certain way to their preceding deformation textures [26]. However, recrystallization behavior is influenced by microscopic variations in the deformed structure, thus a complete description of the mechanisms of texture evolution during recrystallization is difficult to obtain [25].

During particle stimulated nucleation of recrystallized grains, recrystallized grains nucleate in the deformation zones around second phase particles (see section 2.3.2). The possible orientations for these nuclei are limited to the crystallographic orientations that already exist in these zones. In a heavily deformed material, these deformation zones may contain severe misorientations. Consequently, the available orientations for recrystallization nuclei is widely spread around the original grain orientations. Particle stimulated nucleation thus typically results in a weakening of the texture after recrystallization [27].

2.5 Hot forming and formability

An important property when forming a product is the formability of the relevant material. The term formability refers to the ability of a metal to undergo plastic deformation without failure. High formability is thus required in a metal sheet in order for it to sustain a large shape change associated with forming of a component with complex geometry.

The formability of a material is strongly influenced by the forming temperature, in addition to the stress state and the deformation rate [31]. Aluminium has limited formability at room temperature. However, the formability may increase significantly with increasing temperature [27, 31]. Hot forming or hot working of aluminium may thus be beneficial compared to cold forming if severe plastic deformation is required to obtain the desired geometry. The term hot working refers to plastic deformation of materials at high temperatures (above $0.5T_m$) and high strain rates (typically 10^{-3} to 10^3 s^{-1}) [32]. In summary, forming a material at a these high temperatures may have the following major advantages:

- The flow stress of the material is low at high temperatures, greatly due to dynamic restoration processes [27]. Consequently, the forces or work required by the forming tools are significantly lower than at room temperature.
- The achievable straining of the material without fracture is larger at higher temperatures [32], thus the material can be more severely deformed than at room temperature. This gives higher flexibility regarding the obtainable geometries of the formed component.

2.5.1 Deformation mechanisms at high temperature

Deformation of metals at high temperature may occur by different mechanisms than deformation room temperature. High temperature increases the mobility of atoms, and thus also the dislocation mobility by the mechanism of climb [14]. Another effect of increasing the temperature is the activation of additional slip planes. In aluminium, slip happens on the {111} planes at room temperature. However, above 260°C, slip may occur on both the {111}, {100} and {211} planes [14], thus more slip systems are available to accommodate the induced strains at high temperatures.

At the highest stress levels, deformation occurs by dislocation glide comparable to deformation at room temperature. However, the flow stress for dislocation glide decreases with increasing temperature because the shear modulus of the material decreases, and because thermal fluctuations assist the applied stress in moving dislocations past short-range obstacles like coherent precipitates, solute atoms and other dislocations [14].

At high temperature and slightly lower stress levels, the dominating deformation mechanism is dislocation creep [14]. The deformation process during hot working of aluminium are commonly considered a dislocation-creep process [32]. The dislocations still glide, but obstacles are overcome by thermally assisted mechanisms involving diffusion. Steady-state dislocation creep occurs when the strain hardening and dynamic recovery processes reach a balance [14]. This process will be more closely described in the following section (Section 2.5.2).

At high temperature and low stress levels, deformation occurs through diffusion creep or grain boundary sliding. During grain boundary sliding, the grains slide relative to each other by shearing along the boundaries [14].

2.5.2 Deformation and dynamic recovery

When a material is deformed at elevated temperatures, restoration processes similar to those described in Section 2.3 may occur simultaneously with the deformation. The restoration processes are then called *dynamic* recovery and *dynamic* recrystallization. In aluminium, dynamic recovery is rapid [27], while dynamic recrystallization is uncommon [28] as the dynamic recovery process typically is too effective for the material to reach the dislocation density required to stimulate dynamic recrystallization [32].

When hot deformation initiates, dislocations are generated and begin to entangle at the onset of plastic flow. The flow stress thus starts to increase as in cold forming. However, these dislocations are mobile due to the high temperature, thus as the dislocation density rises, the driving force for restoration increases simultaneously and the previously described recovery process initiates [27]. The high temperature allows a high rate of dynamic recovery, which continuously eliminates the strain hardening [14]. If the temperature and strain rate balance, the generation and annihilation of dislocations reach a dynamic equilibrium where the dislocation density remains constant [28]. The flow stress ceases to increase and reaches the characteristic steady-state [27], see Figure 2.8.

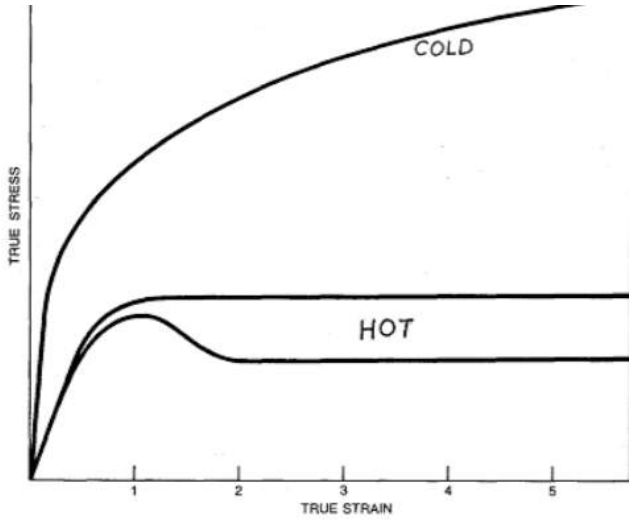

Figure 2.8: Characteristic flow curves for cold and hot deformation. For hot deformation, the upper curve represents a typical flow curve when dynamic recovery occurs, while the lower curve represents a typical flow curve when dynamic recrystallization occurs. From McQueen and McGregor Tegart [28].

During the steady-state of the deformation process, the subgrains remain the same size up to large strains, even though the grains they make up elongate as in cold deformation processes. This is possible because the continuous recovery allows the sub-boundaries to be continuously broken down and formed elsewhere while their spacing remains constant. The size of these subgrains, and thus the steady-state flow stress is dependent on the temperature and strain rate during deformation. At high temperatures, the annihilation process is very rapid, and the subgrain size at steady-state is consequently high. This gives low steady-state flow stress. High strain rates result in rapid generation of dislocations and thus smaller subgrain size. This correspondingly gives a high steady-state flow stress [28]. In summary, the steady-state flow stress of a given material then tend to depend mainly on the strain *rate* ($\dot{\varepsilon}$) and the temperature (T), while the effect of the strain itself (ε) disappears [33].

If the recovery process keeps up with the deformation, very large deformations may be obtained before fracture [14]. In order to achieve high formability, the deformation should thus be carried out at a temperature and strain rate where the recovery mechanisms are sufficiently fast to cancel the strain hardening.

The dynamically recovered structure arising during hot deformation is fairly stable and may be retained down to room temperature if the aluminium is cooled from the working temperature relatively quickly. This dynamically recovered structure is considerably stronger than the recrystallized structure [28].

2.5.3 Strain instability at high temperature

Aluminium sheet typically fail by either strain instability or fracture [19]. Strain instabilities may be either diffuse or local, of which the onset of local necking is regarded as failure as it results in a visible, structural weaknes [34]. Deformation is considered stable if a difference in area between any two cross sections remains constant or decreases [35].

Strain instabilities arise as aluminium alloys, like all other materials, contain inhomogeneities. These include pores, inclusions, second phase particles or irregularities in the surface.

Consequently, during tensile deformation, strain is localized in weaker regions, accompanied by a locally greater enhanced reduction in area. If this reduction in area is accompanied by sufficient hardening of the material, strain proceeds elsewhere. This occurs continuously in the material during a tensile test. However, the rate of work hardening decreases with increasing strain [32]. When the work hardening capacity becomes too low to compensate for the decrease in area, diffuse necking initiates [36]. When diffuse necking occurs in a tensile sample, the region of reduced area extends over a substantial part of the sample length [35]. The necked region is not significantly affected by the adjacent parts of the sample [35], and the stress state within the diffuse neck will be close to uniaxial tension [36].

At onset of diffuse necking, a maximum is reached for the applied force. The mathematical condition is shown in equations 2.2 and 2.3 [32] where F is the applied force, σ is the true stress, A is the instantaneous cross sectional area and ε is the true strain of the sample.

$$dF = \sigma \cdot dA + A \cdot d\sigma = 0$$

$$\implies \frac{d\sigma}{\sigma} = -\frac{dA}{A} \tag{2.2}$$

Given that the volume of the deformed area is constant, $-\frac{dA}{A} = d\varepsilon$ [35], thus diffuse necking initiates when:

$$d\varepsilon = \frac{d\sigma}{\sigma} \tag{2.3}$$

For fcc metals such as aluminium, the flow stress decreases with increasing temperature. However, the rate of work hardening simultaneously decreases more severely [32]. As seen from Equation 2.3, a steeper decrease in $d\sigma$ than σ shifts the onset of necking towards lower strains. Consequently, the strain at onset of diffuse necking is reduced with increasing temperature [37]. From these considerations, it would thus seem as the strainability of aluminium decreases with increasing temperature. However, materials may become *strain rate sensitive* at elevated temperatures, and an increased strain rate sensitivity of the material will both delay the onset of necking [32] and increase the useful deformation that may occur after the onset of diffuse nekcing [35].

The strain rate sensitivity of a material determines the extent to which the flow stress of the material changes with strain rate. At room temperature, strain rate sensitivity is typically negligible [35], however this property is a strong function of temperature [32]. The strain rate sensitivity is commonly described by the strain rate sensitivity parameter (m), defined as the change in steady-state flow stress with strain rate at constant strain and temperature. The mathematical definition is shown in Equation 2.4 [21].

$$m = \left[\frac{\partial(\log\sigma)}{\partial(\log\dot{\varepsilon})}\right]_{\varepsilon,T} \tag{2.4}$$

The strain rate sensitivity parameter may vary between 0 and 1, were 0 represents no change in flow stress with strain rate and 1 represents a linear increase in stress as a function of strain rate [32]. The flow stress of a material that both work hardens and is strain rate sensitive can be described by Equation 2.5 [32], where K'' is a constant specific to the material, ε is the true stress, $\dot{\varepsilon}$ is the true strain rate, m is the strain rate sensitivity parameter and n is the strain hardening coefficient of the material.

$$\sigma = K'' \cdot (\varepsilon)^n \cdot (\dot{\varepsilon})^m \tag{2.5}$$

From Equation 2.5 it can be seen that strain rate sensitivity affects the flow stress due to changes in strain rate in the same manner as strain hardening affects the flow stress due to changes in strain. A strain rate sensitive material is thus correspondingly capable of "strain rate hardening". This phenomenon can be physically interpreted as an increase in flow stress in a developing neck due to increased strain rate in the necking region [32]. This increase in flows stress opposes neck development. It is emphasized that the physical mechanisms causing strain rate sensitivity are not the same mechanisms as those responsible for work hardening.

In summary, the decreased strain hardening at high temperatures encourages neck development, while the increased strain rate sensitivity opposes it. However, the strain rate sensitivity of a material has additional effects on the necking behavior. As earlier mentioned, the useful deformation that may occur after the onset of diffuse necking significantly increases

with increasing strain rate sensitivity [35, 37]. The uniform strain that can be obtained after the onset of diffuse necking actually increases more with increasing strain rate sensitivity than it does with an increase in the work hardening parameter (n) [35]. A high strain rate sensitivity thus enables more strain in the diffuse neck than what a corresponding work hardening parameter does. However, there is a synergistic effect of combined work hardening and strain rate hardening; a material that both work hardens and is strain rate sensitive is able to undergo a significantly greater uniform strain after onset of diffuse necking than a material that only exhibits one of these properties.

The tensile deformation of a diffused neck will be terminated by either fracture or by *local necking* [35]. Local necking occurs within the diffuse neck, and has a size scaling with the thickness of the sample [36]. Substantial interaction between the material in the necked region and the adjacent regions occurs, thus the stress state in the neck becomes triaxial. The state of strain in the local neck is plane strain, and the direction of zero strain is along the width of the neck, thus the cross sectional area within the local neck only decreases in thickness [35].

Similar to the criterion for onset of diffuse necking, local necking occurs when the decrease in cross sectional area in a potential localized neck can no longer be balanced by the rate of strain hardening within the diffuse neck. However, the rate of geometrical softening in a local neck is different from the rate of softening in a diffuse neck, thus the mathematical criterion becomes different [35]. The mathematical condition for onset of local necking in a tensile strip is presented in Equation 2.6 [35].

$$\frac{d\sigma}{d\varepsilon} = \frac{\sigma}{2} \tag{2.6}$$

2.5.4 Fracture at high temperature

The way that aluminium fractures is also affected by temperature (in addition to stress level, stress state and strain rate) [14, 32]. The three main fracture modes at high temperature are rupture, transgranular creep fracture and intergranular creep fracture [32].

Fracture by rupture occurs at the highest stress levels and temperatures. Such stress levels are common in hot working processes with high strain rates [32]. Rupture happens if no other fracture mechanism is triggered, so that the material is deformed until it becomes mechanically unstable and necking essentially proceeds down to a point where there is no material left [14]. Consequently, rupture is characterized by a reduction in area close to 100%. For such large strains to be sustained without onset of fracture, either nucleation of internal cavities or growth of nucleated cavities must be suppressed so that the cavities cannot join and grow into an internal crack [32]. Dynamic restoration of the microstructure may restrain coalescence of voids to such a degree that the material experience rupture [14].

Ordinary ductile fracture may occur at the highest stress levels and at relatively high temperatures, however at lower temperatures than where rupture is observed [14].

Transgranular creep fracture typically occurs at high stress levels and temperatures, but at stress levels lower than required for crystallographic flow to alone cause ordinary ductile fracture. Fracture is rather promoted by diffusional flow. Transgranular fracture is thus associated with a considerable reduction in area, however not as severe as for rupture fractures. Comparable to ductile fracture at lower temperature, the first stage of transgranular creep fracture is nucleation of internal cracks and voids around inclusions or in other microscopic regions of heterogeneous strains. Failure proceeds with growth and coalescence of these voids. Recovery processes occurring at the high temperatures associated with transgranular creep fracture obstruct the nucleation of internal voids, thus fracture is delayed and the ductility is increased. However, when a void first nucleates, diffusional flow and dislocation creep accelerates the void growth, correspondingly promoting fracture and lowering the ductility. The total result is that the ductility of a material that exhibits transgranular creep fracture is comparable to the ductilities observed in low-temperature ductile fractures [32].

Intergranular creep fracture is observed at low stress levels and strain rates, and is thus not very relevant in high strain rate forming operations. This type of fracture occurs when grain boundary sliding contributes to accommodation of the strain, causing wedge cracks and voids

to grow on grain boundaries. Low strain rates and high temperatures promote growth of eliptical cavities on grain boundaries aligned normal to the tensile axis [14].

2.6 Aluminium alloy 6082.25

The aluminium alloy 6082.25 is an alloy within the 6xxx series of aluminium alloys. The 6xxx series are often called Al-Mg-Si-alloys, as Mg and Si are the main alloying elements. Alloys in the 6xxx series generally have medium to high strength, good formability and machineability and high corrosion resistance [15], and they are strengthened by heat treatment. The alloying window for AA6082 is presented in Table 2.1.

Table 2.1: Alloying window for AA6082 [38].

Si	**Fe**	**Cu**	**Mn**	**Cr**	**Ti**	**Mg**	**Zn**
0.7 - 1.3	< 0.5	< 0.1	0.40 - 1	< 0.25	< 0.1	0.60 - 1.20	< 0.20

As the chemical composition may vary considerably within the AA6082 alloying window, alloys can be further classified within the AA6082 category. AA6082.25 is an alloy within AA6082, with a representative composition presented in Table 2.2.

Table 2.2: Typical chemical composition of AA6082.25 [38].

Si	**Fe**	**Cu**	**Mn**	**Cr**	**Ti**	**Mg**	**Zn**
0.92	0.17	0.01	0.55	0.15	-	0.64	0.02

The major elements in the strengthening precipitates in the 6xxx are main alloying elements Mg and Si. These elements precipitate from solid solution upon artificial age hardening, and develops with time until the equilibrium phase Mg_2Si (β) is reached [39]. In summary, the precipitation sequence in the 6xxx series may be written as [40–44]:

$$\begin{matrix}\text{Mg-clusters}\\ \text{Si-clusters}\end{matrix} \rightarrow \text{Co-clusters} \rightarrow \text{GP-zones} \rightarrow \beta'' \rightarrow \beta' \rightarrow \beta$$

In addition to the main alloying elements in AA6082.50 (Mg and Si), several other elements are commonly present. Mn and Cr contribute to grain refinement. These elements are included in different types of precipitates called dispersoids, which have limited direct effect on the mechanical properties of the alloy [15]. However, the dispersoids may greatly affect the microstructure of the alloy during heat treatment by preventing recrystallization. Mn or Cr based dispersoids are small particles that are incoherent with the matrix [19]. Another common element found in AA6082.50 is Cu, which contributes to increased strength [39]. Fe is also present, and is mainly found in coarser intermetallic particles [45]. The other alloying elements are also commonly included in these intermetallic particles, and a variety of different compositions exist [19].

2.6.1 Heat treatment parameters

The solution heat treatment temperature for AA6082.25 acknowledged by Raufoss Technology is 540°C [46]. The artificial ageing sequence recognized to give T6 condition for AA6082.25 is correspondingly established as ageing at 190°C for 90 minutes [46].

2.7 Aluminium alloy 7021.50

The aluminium alloy 7021.50 is an alloy within the 7xxx series of aluminium alloys. The 7xxx series are often called Al-Mg-Zn-alloys, as Mg and Zn are the main alloying elements. Alloys in the 7xxx series may have superior strength, but they also tend to suffer from stress corrosion [47]. The 7xxx alloys can be strengthened by heat treatment.

As the chemical composition may vary considerably within the AA7021 alloying window, alloys can be further classified within the AA7021 category. AA7021.50 is an alloy within AA7021, with the alloying window presented in Table 2.3 [38].

Table 2.3: Alloying window for AA7021.50 [38].

Si	Fe	Cu	Mn	Cr	Mg	Zn	Zr
< 0.2	0.3	0.20 - 0.40	< 0.05	< 0.04	1.70 - 1.85	5.5 - 6.2	0.12 - 0.25

The major elements in the strengthening precipitates in the 7xxx are main alloying elements Zn and Mg. These elements precipitate from solid solution upon artificial age hardening, and develops with time until the equilibrium phase $MgZn_2(\eta)$ is reached [39]. The precipitation sequence is summarized as follows [48]:

$$\begin{matrix}\text{GP(I)-zones} \\ \text{GP(II)-zones}\end{matrix} \quad \rightarrow \quad \eta' \quad \rightarrow \quad \eta$$

The addition of Cu to a 7xxx series alloy increases the strength significantly, giving rise to the strongest commercially used aluminium alloys [39]. Cu enhances the strength both by solid solution strengthening and as a part of the main precipitates [39]. Fe is as for the 6xxx series alloys present in coarser intermetallic particles together with other alloying elements [19]. Zr promotes the precipitation of $ZrAl_3$-dispersoids which inhibit recrystallization of the alloy and promotes a very fine subgrain structure where the boundaries are decorated with hardening precipitates [19]. As opposed to Mn- and Cr-dispersoids, the $ZrAl_3$-dispersoids are coherent with the matrix [49], and they are considered the most effective dispersoids used commercially [16, 50].

2.7.1 Heat treatment parameters

The solution heat treatment temperature for AA7021.50 acknowledged by Raufoss Technology is 480°C [46]. The artificial ageing sequence recognized to give T6 condition for AA7021.50 is correspondingly established as more than 24 hours at room temperature, before ageing at 100°C for 5 hours, and subsequently 150°C for 6 hours [46].

2.8 Testing with the Gleeble System

Experiments were conducted at Hydro Sunndalsøra with the Gleeble 3500 Thermal System. Some considerations regarding testing with the Gleeble System are presented in this section, as this equipment is uncommon.

The Gleeble System is very flexible regarding temperature cycle and deformation rates. Samples can be heated very quickly by direct electrical resistance heating, however, as heat is conducted out of the samples through the grips, the temperature will not be uniform throughout the length of the sample. Samples will have the highest temperature in the middle and the temperature will be decreasing towards the grips [51]. As the flow stress of the materials typically is lowest in the warmest area, the deformation will be highly nonuniform. The nonuniform deformation also makes it impossible to achieve a constant true strain rate in Gleeble-testing.

High cooling rates are also obtainable as the samples are fixed by water-cooled grips or clamps. However, as the heat is extracted in both ends of the sample, the temperature profile in the samples will as earlier mentioned be highly nonuniform. Figure 2.9 shows typical temperature profiles in a round standard tensile sample with a temperature of 500°C in the center. The clamp material influences the cooling rates and temperature profiles in the samples. The green lines represent Cu clamps, which was used for the experiments in this report.

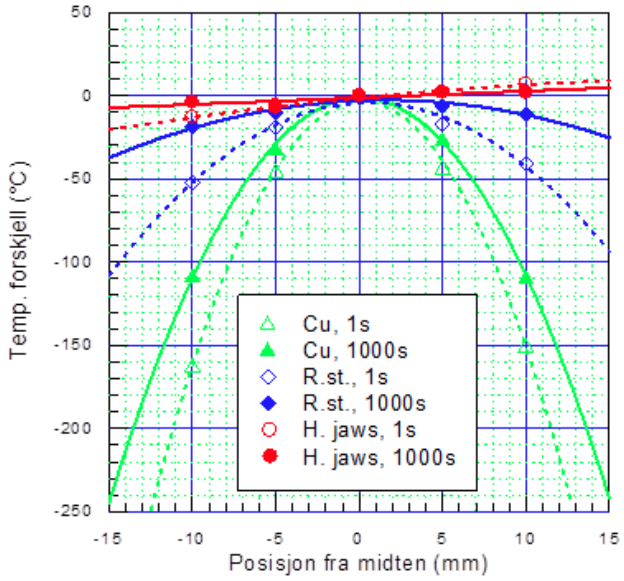

Figure 2.9: Temperature profiles in samples in the Gleeble testing machine [51]. Distance from the center [mm] versus the difference in temperature with respect to the center [°C].

In Gleeble-testing, the temperature is monitored by thermocouples welded on at the center of the sample, thus the temperature cycle applied in a test is only representative for that area.

The holding time at high temperatures affects the subsequent cooling rates. Long holding time at a high temperature increases the temperature of the grips and the surroundings, thus the subsequent cooling rates would be lower than for short holding times. The cooling profiles obtained with Cu-grips after different holding times at 500°C is presented in Figure 2.10.

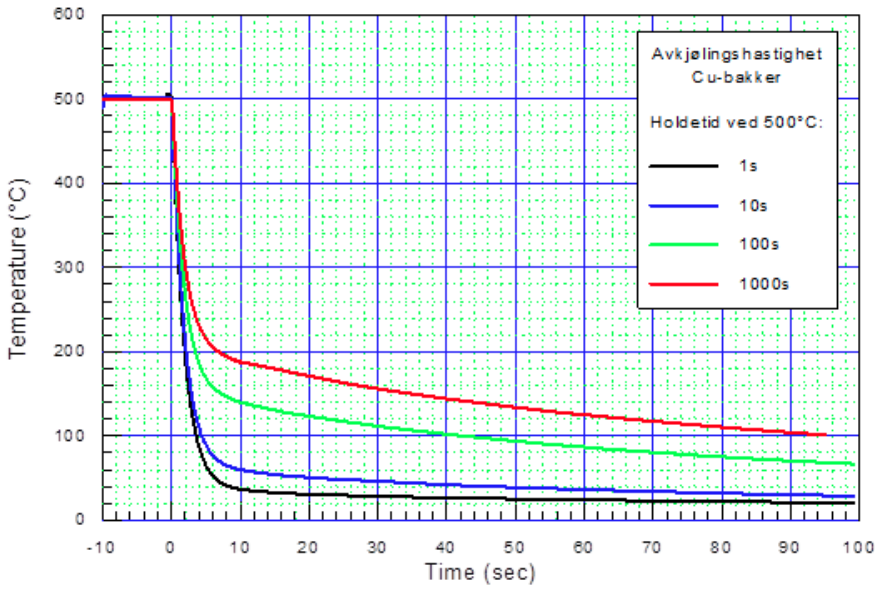

Figure 2.10: Cooling profiles with Cu-grips for different holding times at 500°C [51].

3 Experimental Work

Experiments were conducted in order to evaluate and compare the suitability of the chosen materials for processing by press form hardening (PFH), and to elucidate the capability of this new forming process. The effect of deformation at the high temperatures and strain rates associated with press form hardening on essential properties was of special interest. An overview of the investigated key properties and corresponding experiments are presented in Table 3.1.

Table 3.1: Overview of conducted experiments.

3.1	Characterization of base materials	3.1.1 Light microscopy 3.1.2 SEM and EDS 3.1.3 EBSD
3.2	Formability	3.2.1 Hot tensile testing 3.2.2 Gleeble tensile testing 3.2.3 Fractography
3.3	Microstructure evolution	3.3.1 Heat treatment without deformation 3.3.2 EBSD 3.3.3 Hot tensile deformation 3.3.4 Light microscopy
3.4	Precipitation potential	3.4.1 Heat treatment without deformation 3.4.2 Hot tensile deformation 3.4.3 Gleeble tensile deformation 3.4.4 Hardness measurements 3.4.5 Electrical conductivity measurements

For some experiments, no standard test methods existed that were suitable for execution with the available equipment. Consequently, the test procedures were developed along the experimental work, and several test procedures were attempted in order to obtain useful results.

The investigated materials are repeated in Table 3.2, and their chemical compositions are presented in Table 3.3. Both the rolled sheets and the extruded profiles were produced from extrusion billets, and for each alloy the billets used for production of both material types were processed in the same batch. The further processing parameters are presented in Table 3.4.

Table 3.2: Tested materials.

AA6082.25	**AA7021.50**
Rolled sheet	Rolled sheet
Extruded profile	Extruded profile

Table 3.3: Chemical composition of the delivered materials.

	Si	**Mg**	**Zn**	**Cu**	**Fe**	**Mn**	**Cr**	**Zr**
AA6082.25	0.92	0.64	0.02	0.01	0.17	0.55	0.15	-
AA7021.50	0.08	1.76	5.6	0.29	0.20	0.01	-	0.15

Table 3.4: Processing parameters for the delivered material.

	AA6082.25	**AA7021.50**
Producer	Hydro Karmøy	Benteler Raufoss
Homogenizing	575°C / 2.25h	Unknown
	Rolled material	
Hot rolling to	7 mm	7 mm
Soft annealing	350°C / 2 h + slow cooling	350°C / 2 h + slow cooling
Cold rolling to	4.8 mm	4.8 mm
	Extruded material	
Reduction ratio	1:31	1:31
Billet temperature	510 °C	500 °C
Extrusion speed	10 m/min	10 m/min
Cooling	Air cooling	Air cooling

The terminology used to describe the planes and directions in the rolled samples are illustrated in Figure 3.1. The same terminology is used for samples of the extruded material, however the rolling direction then translates as the extrusion direction.

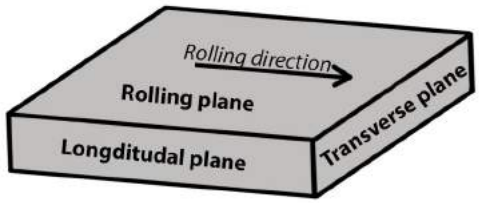

Figure 3.1: Termonology for describing directions and planes in the samples.

3.1 Characterization of the base materials

All four base materials were characterized as delivered in order to determine the initial properties of the material. This allows an evaluation of how properties of the base material affect the suitability for press form hardening, and defines the starting point of the material prior to processing. The material properties that were studied and the associated experimental techniques are summarized in Table 3.5.

Table 3.5: Investigated material properties and associated experimental techniques.

Material property	**Experimental technique**
Grain structure	Light microscopy
Particle structure and chemistry	SEM and EDS
Texture	EBSD

3.1.1 Light microscopy

In order to reveal the grain structure of the samples, the longditudal and transverse planes (see Figure 3.1) were grinded with SiC grinding paper down to 2.5 µm and further polished down to 1 µm with polycrystalline diamond suspension. Subsequently, the samples were anodized with the parameters shown in Table 3.6.

Voltage	20V
Time	120s
Electrolyte	5% HBF_4 - 95% H_2O

Table 3.6: Anodizing parameters for light microscopy.

Pictures of both planes were taken with a Leica MEF4M optical microscope. Polarized light was used to reveal the grain structure.

3.1.2 Energy dispersive spectroscopy and SEM

SEM was used to capture and characterize the particle structures of the materials, and EDS (energy dispersive spectroscopy) was used to asses distinct features of the chemistry of the observed particles and of the matrix. An accurate, quantitative analysis was not intended.

Samples were grinded with SiC grinding paper down to 2.5 µm and further polished with polycrystalline diamond suspension down to 1 µm. Pictures were taken with FE-SEM Zeiss Ultra 55 and EDS spectra were obtained and analyzed with the Quantax Espirit software. The SEM parameters used for the particle characterization are given in Table 3.7. Magnification and scale are given on each picture.

Aperture	300 µm
Voltage	20kV
Working distance	10.1 - 10.8 mm
Probe current	High current

Table 3.7: SEM parameters for characterization of particles.

3.1.3 EBSD

The textures of the base materials were analyzed with EBSD. This was done in order to obtain some indications of the degree of mechanical anisotropy in the base materials. A detailed investigation of the texture and texture evolution was not intended.

Sample preparation was done by grinding with SiC grinding paper down to 2.5 µm and further polishing down to 1 µm with polycrystalline diamond suspension, before electropolishing with Lectropol-5. The electropolishing was conducted with the parameters shown in Table 3.8.

Voltage	20V
Time	20s
Electrolyte	A2
Cooling unit temperature	-30°C

Table 3.8: Electropolishing parameters for EBSD.

EBSD patterns were obtained with the parameters given in Table 3.9, using FE-SEM Zeiss Ultra 55 with the NORDIF EBSD system. The obtained patterns were indexed and analyzed with the EDAX Orientation Imaging Microscopy software in order to obtain pole figures representing the textures.

Accelerating voltage	20 kV
Aperture	300 µm
Probe current	High current
Tilt angle	70°
Work distance	23-26 mm

Table 3.9: Parameters used for EBSD pattern collection.

3.2 Formability

One of the main reasons for developing the press form hardening process is to overcome the challenges regarding formability commonly encountered at room temperature. In order to assess the effect of the relevant forming parameters on the formability of the materials, and thus further assess the capability of the process, the materials' yielding behavior at relevant conditions is investigated. Two factors regarding formability are particularly important;

- The formability of the material, i.e. the achievable strain without fracture or unacceptable strain localization, should be high so that the materials could be formed to complex geometries requiring severe deformations.
- The flow stress of the material at the relevant temperatures should be low, so that the forces or work required by the forming tools would be correspondingly low.

Due to time constraints at the workshop, it was necessary to reduce the number of samples. Therefore, samples were only taken out in the rolling or extrusion direction, and a few test temperatures and strain rates were selected. These constraints also made it necessary to reduce the number of investigated materials. It was considered most important assess the effect of the materials'

- Amount of alloying elements in solid solution
- Initial grain structure (fibrous versus more equiaxed)
- Resistance to recrystallization.

Based on the results from the materials characterization, it was thus concluded that it would be sufficient to compare the materials presented in Table 3.10.

Table 3.10: Materials chosen for formability testing.

AA6082.25	**AA7021.50**
Rolled	Extruded
Extruded	

The test temperatures for the formability testing are presented in Table 3.11. These temperatures were chosen based on the solution heat treatment temperatures applied by Raufoss Technology (540°C for AA6082.25 and 480°C for AA7021.50 [46]). The solution heat treatment temperatures for the respective alloys are thought to be the highest probable temperatures at the onset of deformation, and were thus set as the maximum test temperatures. As the material would be continuously cooled during forming in the press form hardening process, deformation would also be carried out at temperatures below the solution heat treatment temperature, thus tests were also carried out at lower temperatures. Additionally, it would be possible to cool the material before the onset of deformation if this would cause significant advantages further on in the process, however the extent of this pre-cooling would be limited by the precipitation of alloying elements. Based on early trials, it has been estimated that the forming operation will be finished within a relatively narrow temperature range [9]. Consequently, 440°C was set as the lower limit for the formability tests in this work.

Table 3.11: Hot tensile test temperatures.

Alloy	**Temperatures**		
6082.25	540	490	440
7021.50	480	430	380

It is thought that the typical strain rates in the press form hardening process are relatively high, even though precise calculations are not yet available. It was thus desirable to perform the formability tests at high strain rates, however this was restricted by the capacity of the relevant equipment. The applied strain rates are presented for each of the test procedures in the following sections.

As no standard test equipment was available for formability testing at high temperatures and strain rates, test procedures had to be developed along the experimental work.

3.2.1 Hot tensile testing

The equipment mainly availabe for deformation of samples at high temperatures was an INSTRON 5985 universal testing machine rigged with an INSTRON air circulation furnace. Two different test procedures were attempted;

1. Solution heat treatment of the samples *in* the tensile test rig. When solution heat treatment was complete, the furnace door was opened in order to cool the sample to the test temperature, then the deformation was carried out. This approach was attempted in order to simulate the temperature cycle experienced by the material in a real press form hardening process.
2. Solution heat treatment of samples for 5 minutes in a salt bath in advance of the hot tensile testing. Subsequently the samples were mounted in the test rig and heated directly to the test temperature.

For both test procedures a load cell of 5 kN was used. The sample temperature was continuously monitored by pinching a thermocouple in a hole drilled right above the sample curvature. The sample geometry is attached in Appendix A. Note that the extruded profiles had a thickness of 8mm as delivered, thus material was removed on both sides in order to make tensile samples with the same dimensions as for the rolled material (which had a thickness of 4.8mm as delivered).

As materials tend to be sensitive to strain rate at high temperatures, tensile tests were carried out with strain rates of both 0.04 s^{-1} and 0.02 s^{-1} to elucidate this effect. 0.04 s^{-1} was the highest achievable strain rate with the present equipment. At the respective solution heat treatment temperatures, one test was run with a lower strain rate of 0.002 s^{-1}. This was not useful to do at the lower temperatures, as the low strain rate causes the test to last for several minutes. This would allow precipitation of transitional or equilibrium phases (Mg_2Si or Mg_2Zn) which would complicate the results. The complete test matrix presenting all test temperatures, strain rates and number of parallels is attached in Appendix B.

Experience from the author's specialization project [52] suggests that the use of an extensiometer would not be possible at these high temperatures. It was observed that the extensiometer would initiate fracture at the contact points with the samples, even if the extensiometer knives were rounded. Another observation was that the deformation of the sample was constrained within the extensiometer. Consequently, the strain for plotting of stress–strain curves was measured by the machine displacement. These strain measurements are thus not as accurate as if an extensiometer was used.

It was desired to achieve a constant true strain rate during this tensile testing as metals commonly become strain rate sensitive at high temperatures. When the machine displacement is used to measure the strain, it is not possible to make the tensile testing equipment run at a constant true strain rate. However, it is possible to make the equipment increase the crosshead displacement velocity linearly with time. Consequently, a constant true strain rate was approximated linearly, as shown in Figure 3.2a. The correspondingly achieved strain rate is presented in figure 3.2b. The goodness-of-fit of the linear approximations of all applied strain rates are represented by R^2-values in Table 3.12.

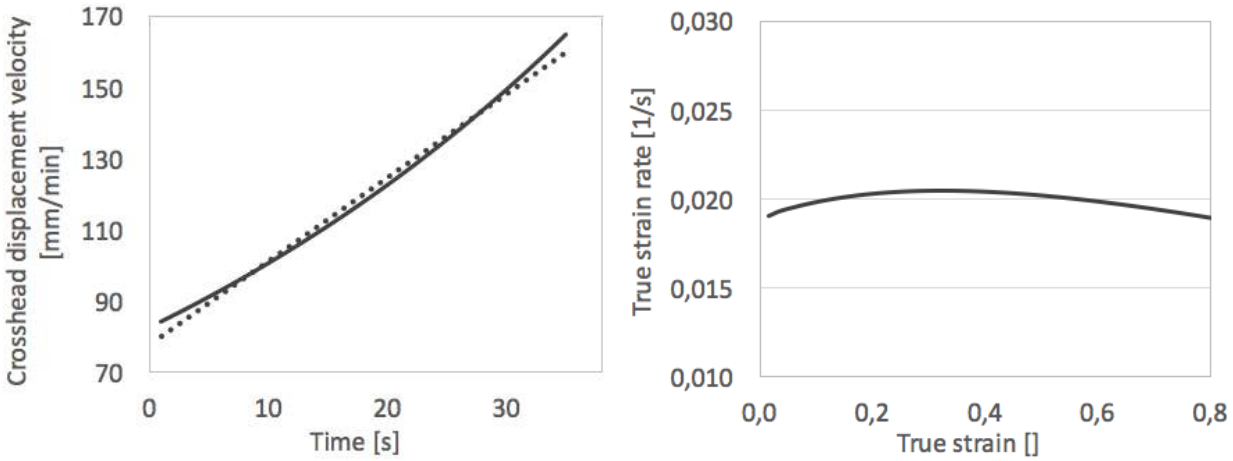

(a) (b)

Figure 3.2: (a): The solid line represents the crosshead displacement velocity required to achieve a constant true strain rate of 0.02 s^{-1}. The broken line represents the corresponding linear approximation. Figure (b) represents the true strain rate achieved with the linear approximation in Figure (a).

Table 3.12: R^2-values for the linear approximations to a constant true strain rate.

Strain rate [s^{-1}]	**R^2-value**
0.04	0.99189
0.02	0.99211
0.002	0.99208

All tests were carried out together with Engineer Vidar Hjelmen at the SINTEF Materials and Chemistry lab at NTNU.

After the tests were completed, the following parameters were obtained by direct measurements on the samples:

- Maximum true strain at the onset of local necking ($\varepsilon_{\text{diff}}$)
- % reduction of area at fracture (%RA)

The maximum strain in the samples before local necking ($\varepsilon_{\text{diff}}$) was measured as a substitute for the uniform elongation, as it was recognized that diffuse necking occurred practically at the onset of plastic deformation. Diffuse necking is commonly acceptable in sheet forming [35], thus the main objective during forming is often to avoid *local* necking. The onset of local necking was estimated visually, and recognized as the point where the thickness of the sample rapidly decreased. At this point, the with and thickness of the sample was measured. The maximum strain at the onset of local necking was calulated from the cross sectional area at this point by Equation 3.1, where $\varepsilon_{\text{diff}}$ and A_{diff} are respectively the true strain and the cross sectional area at the point of maximum strain in the diffuse neck. A_0 is the initial cross sectional area.

$$\varepsilon_{\text{diff}} = -\frac{A_{\text{diff}}}{A_0} \tag{3.1}$$

The dimensions of the fracture areas (A_{f}) were measured with a Carl Zeiss Jena Technival 2 light microscope, equipped with a Fehlmann CH–5703 XY-board and a Mitutoyo KL counter. As the shape of the contracted fracture areas is affected by edge effects and thus have the typical shape

displayed in Figure 3.3, some estimations were made when measuring these dimensions. The thickness of the contracted area was measured at the points A and B, and the average thickness was subsequently estimated. The length of the fracture area was measured as marked by arrow C (starting and ending approximately halfway between the top and bottom of the V-shaped edge). The fracture area representing the true strain at fracture (A_f) was assumed to be a rectangle with length C and thickness $\frac{A+B}{2}$.

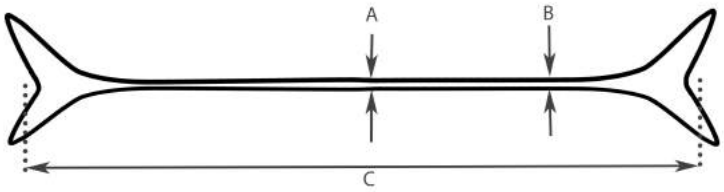

Figure 3.3: The observed typical shape of the fracture areas.

The % reduction in area at fracture was then calculated by Equation 3.2.

$$\%RA = \frac{A_f - A_0}{A_0} \cdot 100 \tag{3.2}$$

Some additional samples of the 6082 rolled material were deformed at 560°C as there were a few samples left over after completion of the other tests.

3.2.2 Gleeble tensile testing

Some supplementary tests of the AA6082.25 rolled material were run with the Gleeble 3500 Thermal System together with Senior Research Scientist Terje Iveland and Senior Laboratory Engineer Ole Andersen at Hydro Aluminium Sunndalsøra. The test matrix is attached in Appendix B. This was done as the Gleeble equipment can provide higher strain rates than the equipment used for the hot tensile testing (described in Section 3.2.1).

The samples were heated to the solution heat treatment temperature with the Gleeble System by direct electrical resistance heating [53]. The samples were kept at the solution heat treatment temperature for 5 minutes. Subsequently the samples were cooled rapidly to the test temperature by the water cooled grips or clamps. Thermocouples were welded on at the center

of the samples to control the temperature. The sample geometry is attached in Appendix A.

As a constant true strain rate cannot be obtained during deformation with the Gleeble System (see Section 2.8), the deformation was carried out with a constant crosshead displacement velocity giving an average strain rate of 2 s^{-1}, averaged over the entire deformation. The deformation zone was estimated to be approximately 10 mm in length. The strain was recorded based on the machine displacement, and stress–strain curves were plotted. The % reduction in area at fracture was measured in the same way as for the hot tensile tests described in Section 3.2.1.

3.2.3 Fractography

Pictures of the fracture surfaces obtained from the experiments described in sections 3.2.1 and 3.2.2 were taken with FE-SEM Zeiss Ultra 55 in order to assess the fracture mechanisms at the relevant temperatures and strain rates. This was performed for one sample deformed at each temperature and strain rate. The samples were prepared by rinsing with ethanol.

3.3 Microstructure evolution

The microstructure of a material is altered by both temperature and deformation, and may significantly affect the material properties. As the press form hardening process involves both high temperatures and deformation, knowledge of how deformation at the spesific relevant conditions affects the microstructure is required. Experiments were conducted in order to assess the following:

- The recrystallization behavior of the materials without deformation. This is done in order to reveal the grain structure of the materials at the onset of deformation (subsequent to solution heat treatment). The results will also elucidate the materials' tendency to recrystallize at temperatures relevant to the forming operation.
- The effect of deformation at high temperature on the grain structure. This will further simulate the microstructure development throughout the combined heating and forming cycle.

The test temperatures were chosen based on the same evaluations as for the hot tensile testing in Section 3.2.1. For the heat treatment without deformation, some slightly higher temperatures were tested to get a more comprehensive view of the recrystallization behavior of the materials.

3.3.1 Heat treatment without deformation

Samples were solutionized at the temperatures presented in Table 3.13 for 5 minutes. The heat treatment was conducted in a salt bath for conveniency.

Table 3.13: Investigated heat treatment temperatures in °C.

AA6082	AA7021
560	500
540	480
520	460
500	440
480	420
460	400

3.3.2 EBSD

As the 6082 rolled material experienced recrystallization during solution heat treatmen, the recrystallized texture was investigated with EBSD. This was done for an undeformed sample heat treated at the solution heat treatment temperature (540°C). EBSD was carried out as described in Section 3.1.3.

3.3.3 Hot tensile deformation

The effect of deformation at high temperatures on the microstructure was investigated by tensile testing at high temperatures, with the same equipment, samples and procedure as presented for the hot tensile testing in Section 3.2.1. Note however that the extruded materials had a thickness of 8mm as delivered, thus 1.6mm of material was removed on both sides in order to make tensile samples with the same dimensions as for the rolled material (sample thickness of 4.8mm). The same materials were tested, they are repeated in Table 3.14.

Table 3.14: Materials chosen for deformation at high temperature.

AA6082.25	**AA7021.50**
Rolled	Extruded
Extruded	

The tests were carried out together with Engineer Vidar Hjelmen at the SINTEF Materials and Chemistry lab at NTNU.

The samples of rolled AA6082.25 were tested with approach 1 described in Section 3.2.1 (solution heat treatment and cooling to test temperature while mounted in the tensile testing rig), while the other two materials were tested with approach 2 (solution heat treatment in a salt bath in advance, then heating directly to test temperature). The test temperatures are repeated in Table 3.15.

Table 3.15: Hot tensile testing temperatures in °C.

AA6082.25	**AA7021.50**
540	480
490	430
440	380

All samples were deformed to 60% elongation, except the 6082 samples deformed at 440°C which could not be elongated more than 50% without initiation of a local neck. The tests were conducted at an approximated constant true strain rate of 0.02 s^{-1} (see Section 3.2.1 for details regarding this approximation). At the highest temperature, one sample was tested with a lower strain rate of 0.002 s^{-1}. This only done at the solution heat treatment temperature as the low strain rate would cause the test to take several minutes. This could give significant precipitation of alloying elements which could complicate the results.

3.3.4 Light microscopy

The grain structure of both deformed and undeformed samples (sections 3.3.1 and 3.3.3) were investigated by light microscopy as described in Section 3.1.1. Samples were taken out from the center of the deformed tensile samples, and the longditudal plane was investigated as this plane has the most readable grain structure.

3.4 Precipitation potential

As earlier mentioned, the expected high cooling rates [9] in the press form hardening process is thought to be beneficial for precipitation of strengthening phases during the subsequent artificial age hardening. However, the effect of the deformation at high temperatures on the subsequent precipitation behavior is unknown. In order to get an indication of how deformation at high temperature affects this precipitation, tests were run with two different approaches:

1. Deformation at high temperature in the hot tensile test rig described in Section 3.2.1.
2. Deformation at high temperature in the Gleeble rig described in Section 2.8.

T6 condition for the present materials was first identified with the undeformed materials. Then the samples deformed at high temperature were artificially age hardened to T6 condition based on these results. The test temperatures were the same as for the formability testing described in Section 3.2, they are repeated in Table 3.16.

Table 3.16: Deformation temperatures in °C.

Alloy	**Temperatures**		
6082.25	540	490	440
7021.50	480	430	380

Samples were also exposed to the temperature cycles characteristic of each test without applying any deformation. This was done in order to be able to separate the effects of the temperature cycle from the effects of deformation on the subsequent precipitation potential.

3.4.1 Heat treatment without deformation

Peak hardness was identified in the previously selected materials repeated in Table 3.17, with basis in the existing artificial ageing curves [46].

Table 3.17: Materials chosen for identification of T6 condition.

AA6082.25	**AA7021.50**
Rolled	Extruded
Extruded	

The samples were heat treated by the standard heat treatment procedures [46] until the last step of the artificial ageing, the heat treatment and test parameters are presented in Table 3.18. At the last step, samples were artificially aged for various durations.

Table 3.18: Test parameters for identification of T6 condition.

Alloy	**Solutionizing temperature [°C]**	**Storage time**	**Ageing step 1**	**Ageing test temperature [°C]**
AA6082.25	540	20 min	-	190
AA7021.50	480	24 - 48 h	100°C, 5 h	150

Solution heat treatment was done in a salt bath for 5 minutes, storage was done at room temperature, and artificial ageing was done in oil baths. Quenching between each step was done in water.

The 6082 samples were kept at room temperature for 20 minutes before artificial age hardening as this is estimated as the shortest achievable transfer time in the press form hardening process. The 7021 samples were stored at room temperature for 24 hours before artificial ageing as the standard ageing treatment states that this alloy should spend 24-48 hours at room temperature after solution heat treatment [46].

3.4.2 Hot tensile deformation

Some extra samples were deformed during the experiments regarding microstructure development (described in Section 3.3.3). The deformation was conducted with the same procedure, however these samples were artificially aged to the peak hardness subsequent to deformation. Artificial ageing was done according to the ageing curves obtained from the experiments described in the previous section (Section 3.4.1).

3.4.3 Gleeble tensile deformation

Samples were solution heat treated for 5 minutes while mounted in the Gleeble Thermal System described in Section 2.8, and subsequently cooled rapidly to the test temperature by the water cooled grips. Deformation was carried out, and the samples were further cooled to room temperature by the Gleeble System before artificial ageing. The artificial ageing was done according to the ageing curves resulting from the experiments described in Section 3.4.1. The sample geometry is attached in Appendix A.

The deformation was carried out at the average strain rates of 2 s^{-1} and 0.2 s^{-1}, averaged over the entire deformation. The zone where the main part of the deformation occurred was roughly estimated to be approximately 10 mm in length, and the samples were elongated 6 mm. Two parallell samples were run for each set of test parameters.

As previously mentioned, there are significant temperature gradients present during testing with the Gleeble System, which gives heterogeneous deformation of the samples. The Gleeble System controls the temperature by thermocouples that are welded to the middle of the samples, thus it is only this region that experiences the applied temperature cycle. Further measurements thus were conducted in the middle of the sample.

As the deformation of the samples is nonuniform in Gleeble testing, the sample dimensions in the center of the samples were measured with a caliper after deformation. The strains were calculated based on the deformed area according to Equation 3.3 [21], where A is the measured

area in the deformed region, A_0 is the original cross sectional area and ε is the true strain.

$$\varepsilon = \ln(\frac{A_0}{A}) \tag{3.3}$$

3.4.4 Hardness measurements

Vickers hardness (HV5) after artificial age hardening was measured with Vickers Hardness Tester DVK-1S from Matsuzawa. A load of 5 kg was applied with a loading time of 15 seconds. The loading speed was 100 µm/s. The hardness was measured in the rolling plane (see Figure 3.1), without any preceeding grinding or polishing of the sample. For the deformed samples, the hardness was measured in the middle of the deformed area. 5 indents were made at each sample.

3.4.5 Measurements of electrical conductivity

The electrical conductivity of the samples deformed with the Gleeble System was measured with a Foerster Sigmatest 2.069. The measurements were done in the rolling plane of the deformed samples, and in the middle of the deformed area. The electrical conductivity of the samples treated with the representative temperature cycles without applying any deformation was measured correspondingly.

4 Results

4.1 Characterization of the base materials

The selected potential base materials were characterized as delivered in order to determine the initial properties of the material, thus allowing an evaluation of how these properties changes throughout the PFH process. The following properties were examined:

- Grain structure
- Particle structure and chemistry
- Texture

4.1.1 Grain structure

The grain structures of the four base materials are presented in Figure 4.1. It can be seen that both the extruded materials have a grain structure consisting of long and narrow grains along the extrusion direction. The 6082 rolled material consists of grains elongated in the rolling direction, however the grains are shorter and wider than what is observed in the extruded materials. The grains in the 7021 rolled material are also long and narrow and aligned along the rolling direction, however, the large amount of particles, seen as small black spots where the anodized layer is incomplete, makes the grain structure appear slightly unclear.

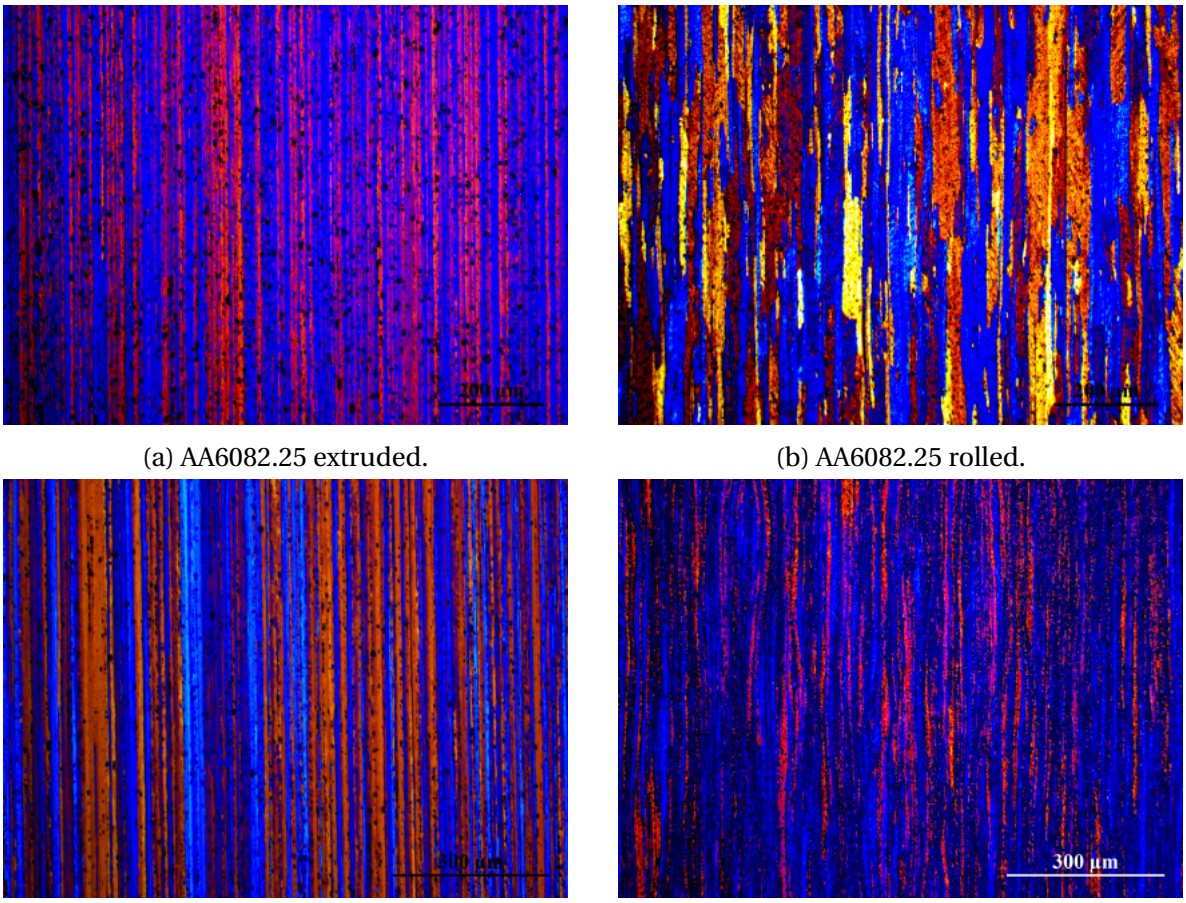

(a) AA6082.25 extruded.

(b) AA6082.25 rolled.

(c) AA7021.50 extruded.

(d) AA7021.50 rolled.

Figure 4.1: Initial grain structure of the base materials at 10x magnification. The scale on picture (d) is representative for all pictures.

4.1.2 Particle structure and chemistry

The particle structures of the base materials are presented in figures 4.2 and 4.3. The particles are seen as white spots. In both the extruded materials, distinct lines of particles aligned parallel to the extrusion direction is observed. The particle structure seems more random in the rolled 6082 material, however bands of higher and lower particle density can be observed. The particles in the rolled 6082 material is smaller than in the 6082 extruded material. The rolled 7021 material contains significantly more particles than the other materials, thus it is difficult to recognize an obvious structure. The particles in this material are a mixture of small and larger sized particles. Differences between the alloys can be seen as the 6082 extruded material contains more and larger particles than the 7021 extruded material.

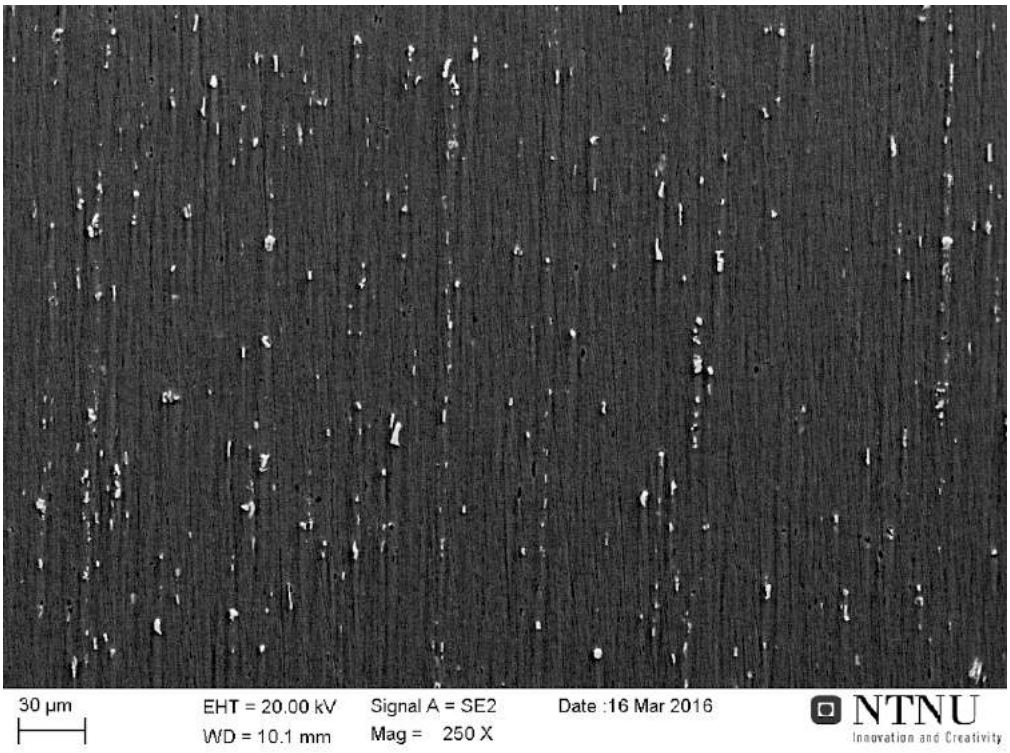

(a) AA6082.25 extruded.

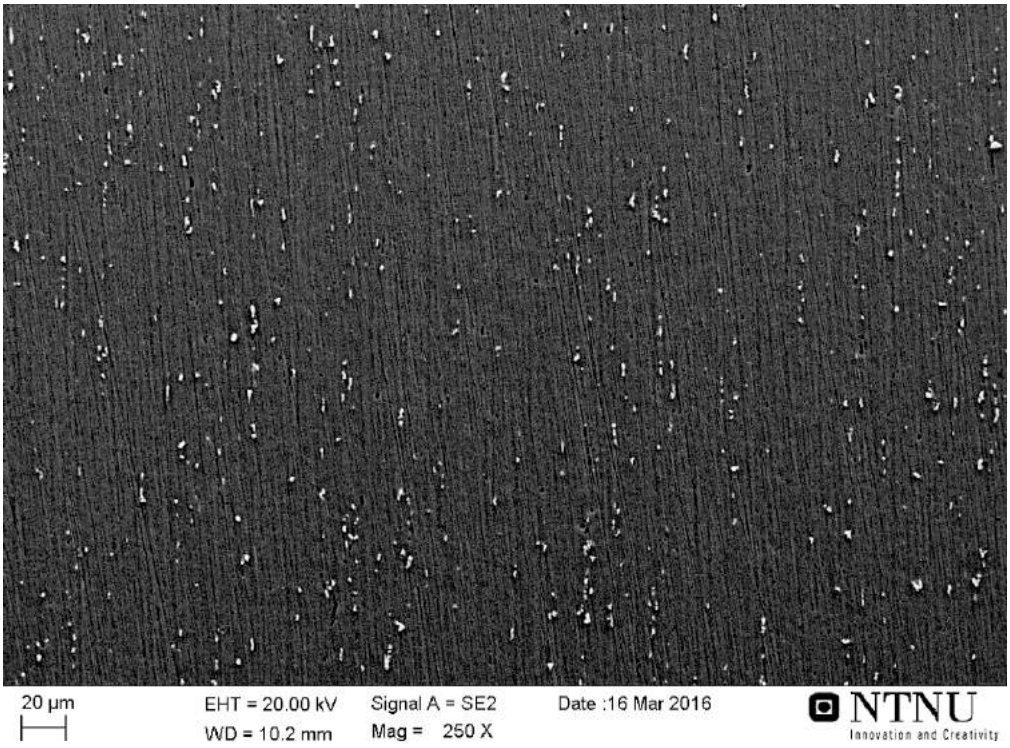

(b) AA6082.25 rolled.

Figure 4.2: Particle structures of the AA6082.25 base materials

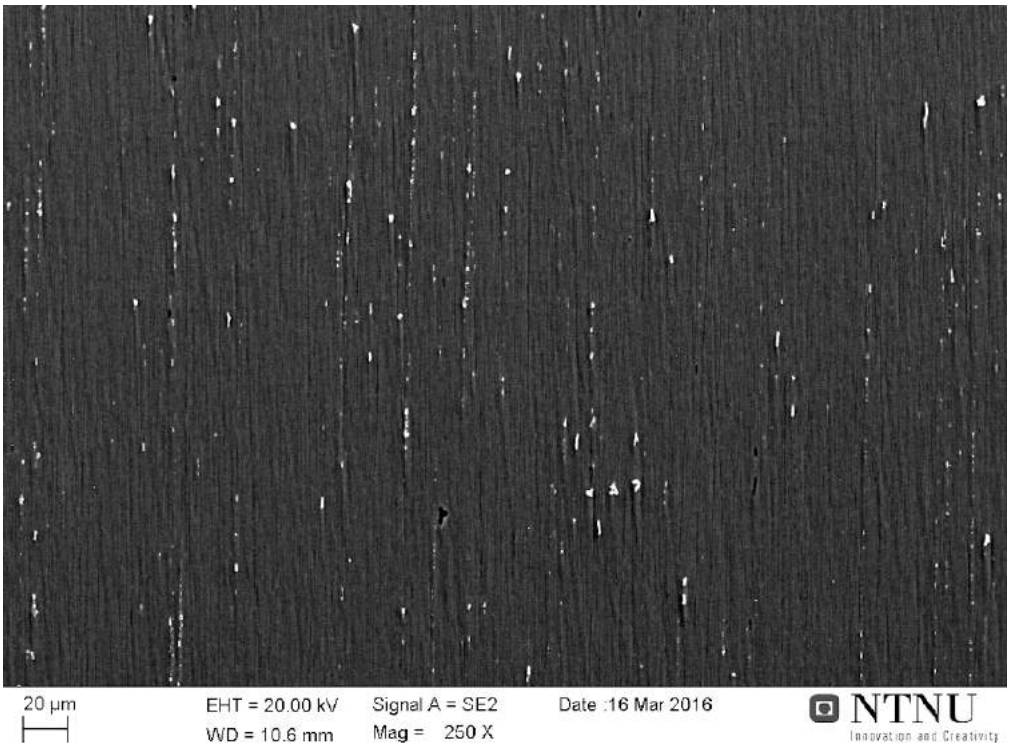

(a) AA7021.50 extruded.

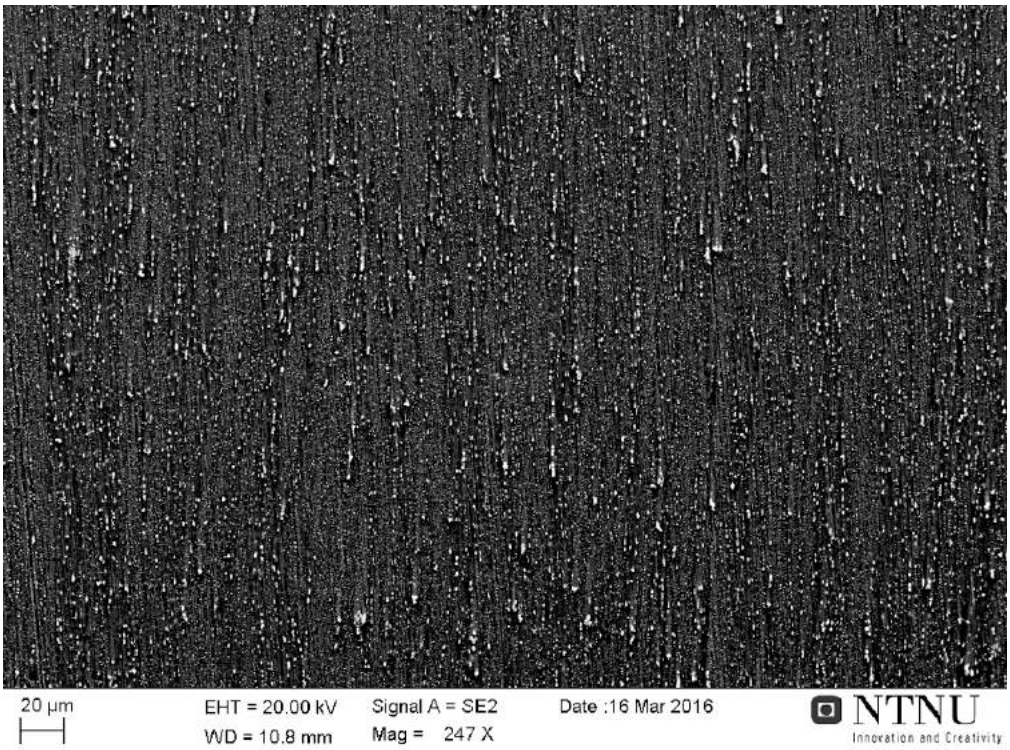

(b) AA7021.50 rolled.

Figure 4.3: Particle structures of the AA7021.50 base materials

EDS was used to asses distinct features of the chemistry of the particles and the matrix. An accurate, quantitative analysis was not intended. The average chemical composition of the analyzed particles and the matrix are presented in tables 4.1 and 4.2. The chemical composition of the particles are presented as the ratio of the concentration of the different chemical constituents to the concentration of Fe (Zn for some particles in the 7021 rolled material). This way of presenting the results was chosen as the emission depth of the electron beam may be larger than the depth of some particles, thus the emission volumes contain different fractions of particle. This greatly affects the measured absolute concentrations of the alloying elements. The concentration ratios will also be affected by the amount of matrix in the emission volume, however the effect will be less as the matrix mostly consist of Al. SEM pictures of the analyzed particles and the corresponding complete results are attached in Appendix C.

Keeping in mind that these EDS results are not highly accurate with respect to quantity, the results for the 6082 materials (Table 4.1) showed no distinct different features between the rolled and the extruded material. The same elements are present in both alloys.

Table 4.1: Chemical composition of particles [ ] and matrix [wt%] in the AA6082.25 materials.

(a) Extruded material.

Particles		**Matrix**	
Si/Fe	0.65	**Si**	0.69
Mn/Fe	0.77	**Mn**	0.26
Mg/Fe	0.16	**Mg**	1.42
Cr/Fe	0.11	**Cr**	0.02
Cu/Fe	0.01	**Cu**	0.01
Zn/Fe	0.00	**Zn**	0.00
		Fe	0.00

(b) Rolled material.

Particles		**Matrix**	
Si/Fe	1.22	**Si**	0.58
Mn/Fe	1.63	**Mn**	0.41
Mg/Fe	0.31	**Mg**	1.16
Cr/Fe	0.28	**Cr**	0.07
Cu/Fe	0.01	**Cu**	0.05
Zn/Fe	0.00	**Zn**	0.01
		Fe	0.08

The EDS results for the AA7021.50 materials (Table 4.2) show that two distinct particle types are observed in the rolled material, one that mainly contains Fe and another that mainly contains Zn. Only the Fe based particles are observed in the 7021 extruded material. No other distinct differences were observed, except for a higher concentration of Zn in the matrix of the extruded material than in the matrix of the rolled material. Both materials contain the same elements.

Table 4.2: Chemical composition of particles [ ] and matrix [wt%] in the AA7021.50 material.

(a) Extruded material.

Particles		**Matrix**	
Si/Fe	0.09	**Si**	0.21
Mn/Fe	0.00	**Mn**	0.01
Mg/Fe	0.17	**Mg**	2.57
Cu/Fe	0.11	**Cu**	0.28
Zn/Fe	0.31	**Zn**	5.89
Zr/Fe	0.05	**Zr**	0.49
		Fe	0.03

(b) Rolled material.

Particle 1		**Particle 2**		**Matrix**	
Si/Fe	0.05	**Si/Zn**	0.03	**Si**	0.20
Mn/Fe	0.11	**Mn/Zn**	0.00	**Mn**	0.02
Mg/Fe	0.14	**Mg/Zn**	0.29	**Mg**	1.92
Cu/Fe	0.04	**Cu/Zn**	0.06	**Cu**	0.15
Zn/Fe	0.03	**Fe/Zn**	0.06	**Zn**	3.74
Zr/Fe	0.00	**Zr/Zn**	0.04	**Zr**	0.47
				Fe	0.13

By comparing tables 4.1 and 4.2, it can be seen that the concentration of alloying elements is higher in the AA7021.50 material than in the AA6082.25 material. All materials contain Fe-based particles.

4.1.3 Texture

The textures of the base materials were analyzed in order to obtain some indications of the degree of mechanical anisotropy in the base material. A detailed investigation of the effects of texture and texture evolution was not intended. Figure 4.4 presents the polefigures obtained from the EBSD scans of the base materials, and the corresponding maximum intensities are presented in Table 4.3. The sizes and grain structures of the scanned areas are attached in Appendix E.

In both extruded materials and the rolled 7021 material, the $\{111\}\langle\bar{1}\bar{1}2\rangle$ texture component is the most pronounced. It seems, however, as there is some rotation of orientations around the

$\langle \bar{1}\bar{1}2 \rangle$ direction in the extruded materials as the high intensity points are drawn out around the ideal orientation. This is not observed to the same degree in the rolled material where the areas of high intensity are more gathered. Slight traces of the cube orientation $\{010\}\langle 100 \rangle$ can be seen in the 6082 and 7021 extruded materials. The chaotic pole figure of the 6082 rolled material have a maximum intensity of 3.6 times random, thus it practically indicates a random texture. The rolled materials have weaker textures than the extruded materials, however the maximum intensites of 10 and 10.9 times random is not particularly high, thus the textures are weak.

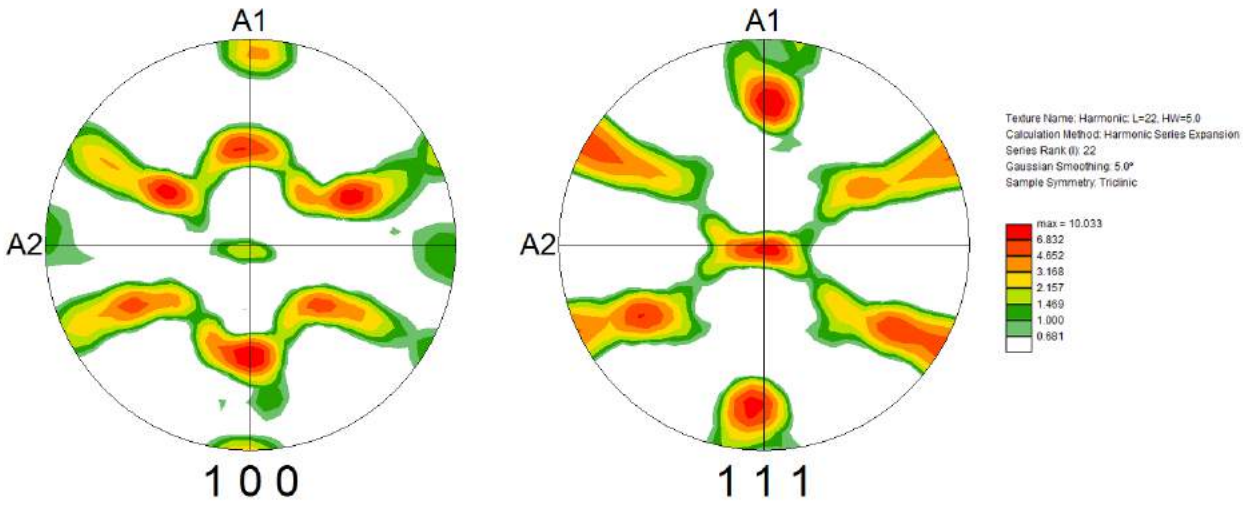

(a) AA6082.25 extruded.

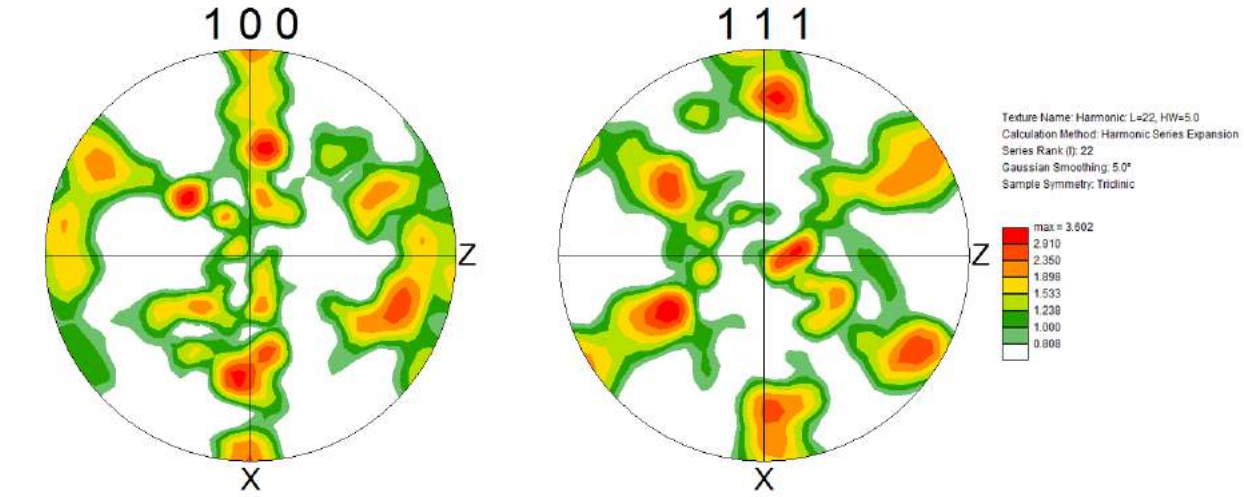

(b) AA6082.25 rolled.

Figure 4.4: Pole figures representing the textures of the 6082 base materials.

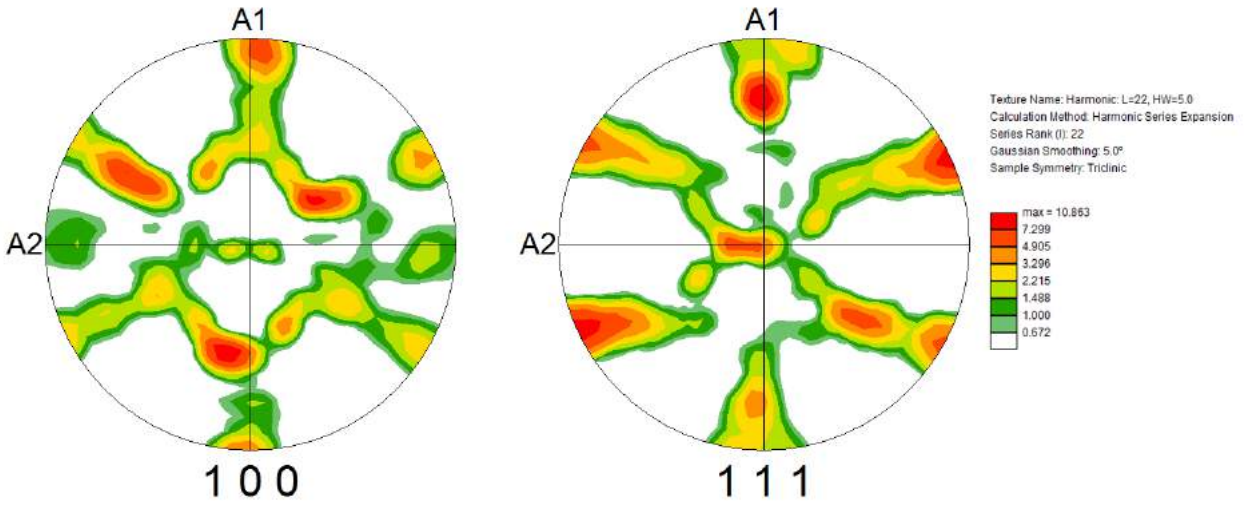

(c) AA7021.50 extruded.

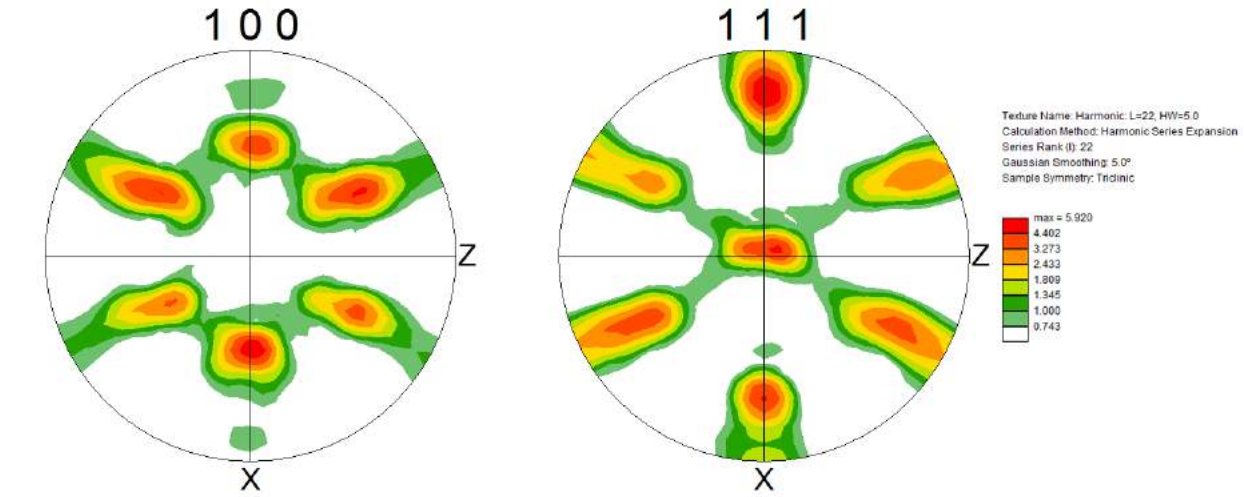

(d) AA7021.50 rolled.

Figure 4.4: Pole figures representing the textures of the 7021 base materials.

Table 4.3: Maximum intensity observed in the pole figures.

	Extruded		**Rolled**	
Alloy	**AA6082.25**	**AA7021.50**	**AA6082.25**	**AA7021.50**
Max. intensity	10.0	10.9	3.6	6.0

4.2 Formability

Tests were carried out in order to assess the flow behavior of the materials at different temperatures and strain rates relevant to processing by press form hardening process.

4.2.1 Hot tensile testing

Two approaches were attempted for the hot tensile testing:

1. Solution heat treatment in the tensile rig
2. Separate solution heat treatment prior to mounting in the test rig

For the samples that were solution heat treated in the tensile rig, the main results were that it is not possible to produce a satisfactory temperature cycle with this approach. The test procedure with separate solution heat treatment was preferred. This conclusion is further elaborated in the discussion. The results presented in the following are thus the results from the tests ran with solution heat treatment prior to mounting in the test rig.

The obtained true stress–strain curves had the typical shape displayed in Figure 4.5. The complete set of true stress–strain curves for all materials and strain rates are attached in Appendix D. Note that a steady state flow stress where the true stress remains close to constant up to large strains is established quickly after the onset of plastic deformation. However, some curves have a very slight maximum around the middle of the steady-state region. The corresponding engineering curves are presented in Figure 4.6. All materials experienced a maximum in engineering stress right at the onset of plastic deformation at all temperatures and strain rates. After this maximum, the engineering stress declined at a constant rate up to large elongations.

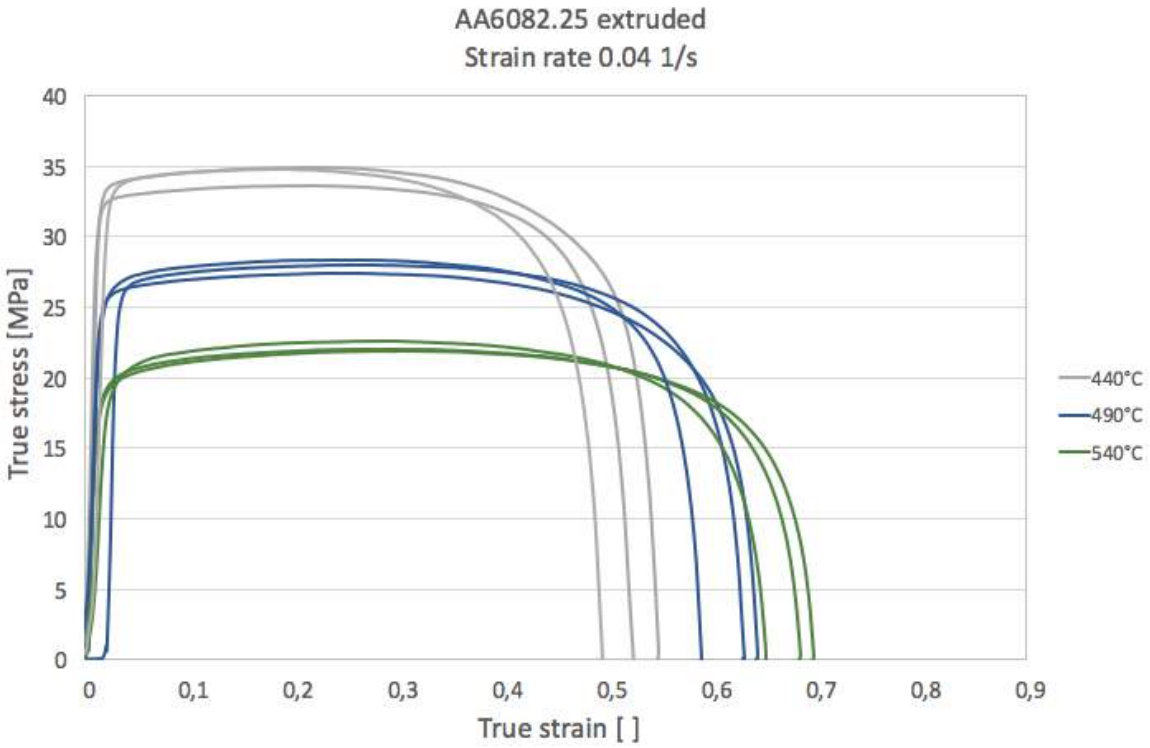

Figure 4.5: True stress–strain curves representing the typical shape of all obtained curves.

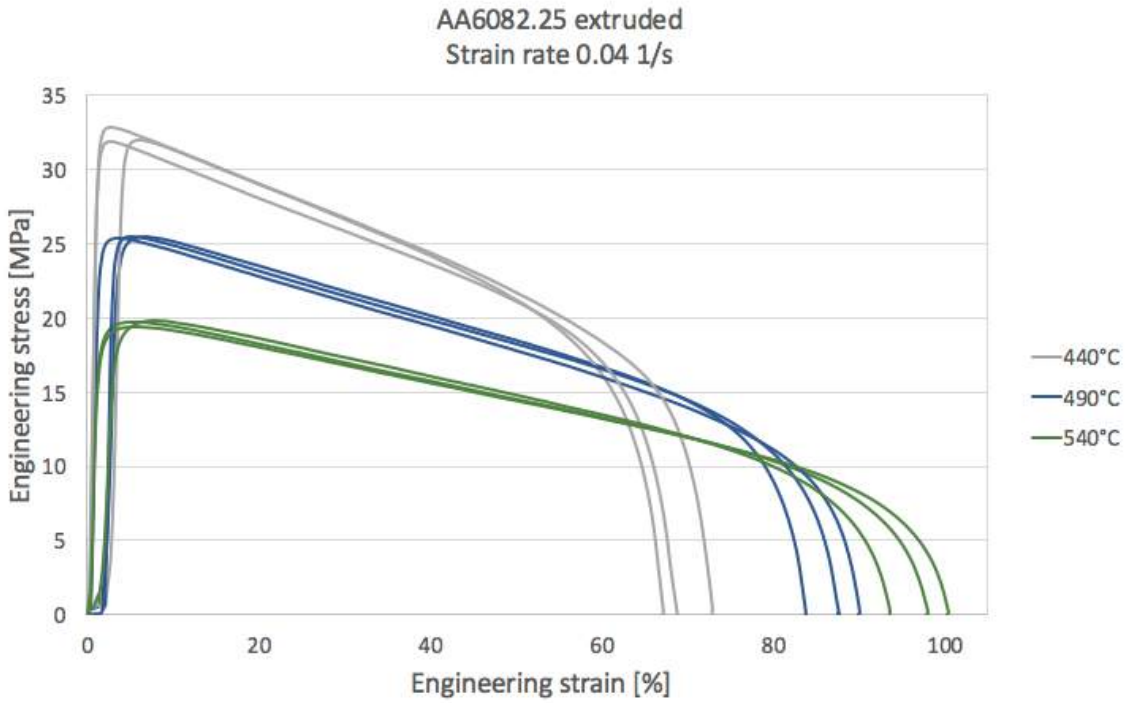

Figure 4.6: Engineering stress–strain curves representing the typical shape of all obtained engineering curves.

The variation in maximum true flow stress with temperature and strain rate is presented in Figure 4.7. The separately marked points represent the one sample of each material tested at the low strain rate of 0.002 s^{-1} (for the two 6082 materials, these two points coincide).

It can be seen that the maximum true flow stress decreases with increasing temperature for all the investigated materials. For the 7021 extruded material, the flow stress decreases steeply as the temperature approaches the solution heat treatment temperature. The corresponding decline in maximum true flow stress is more gradual for the two 6082 materials. The behavior of the 7021 material is however not investigated above the respective solution heat treatment temperature of 480°C.

The flow stress of the 7021 material is strictly higher than for the 6082 material, however at 480°C, the difference is not more than 6 MPa. For all materials, the maximum true flow stress increases with increasing strain rate. This effect is more pronounced in the 7021 material than in the 6082 materials. The rolled 6082 material has consistently lower flow stress than the 6082 extruded material, however their maximum flow stresses vary similarly with temperature and strain rate.

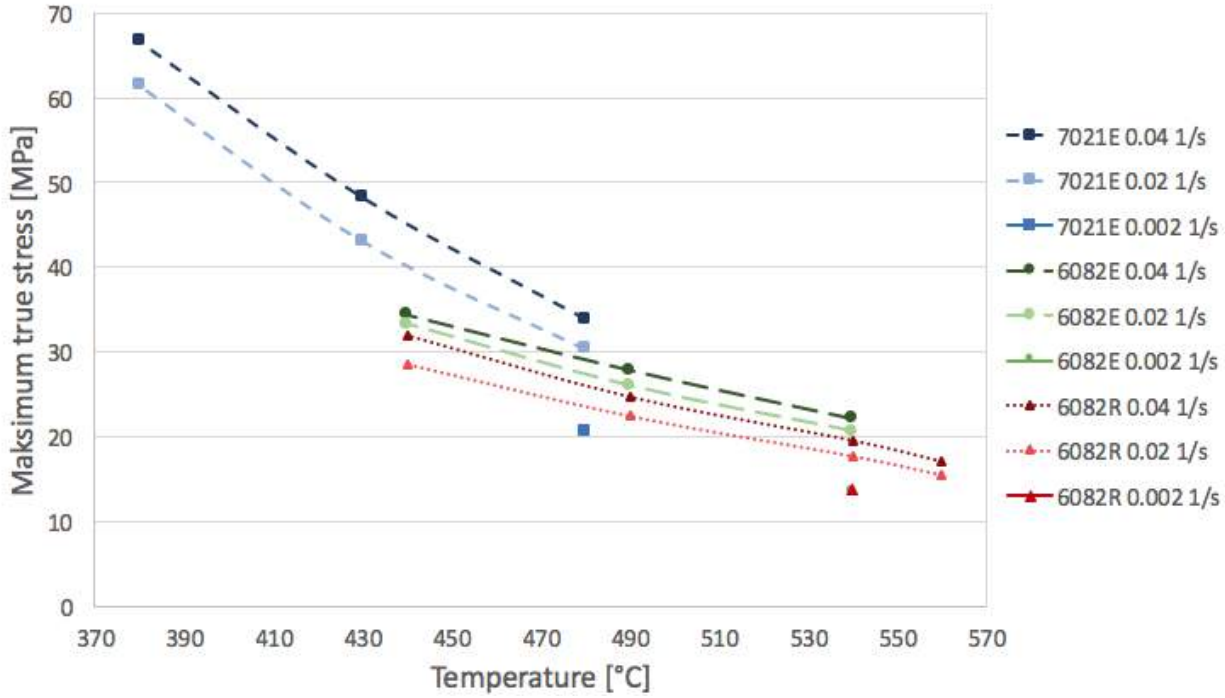

Figure 4.7: Variation in maximum flow stress with temperature and strain rate.

The variations in % reduction of area with temperature for the different materials deformed at strain rates 0.02 s^{-1} and 0.04 s^{-1} are presented in Figure 4.8. Keeping in mind that the precision in the fracture area measurements is limited both due to the irregular shape of the fracture surfaces and due to the remarkably narrow fracture areas, the % area reduction vary very little with both temperature, strain rate and material. Close to 100% area reduction was observed in these samples, thus all materials sustained great strains before fracturing at these strain rates. For the samples deformed at 0.002 s^{-1}, corresponding results were not observed. The % reduction of area for these samples are presented in Table 4.4. At this low strain rate, the 7021 extruded material still demonstrated close to 100% area reduction, while the reduction of area at fracture was significantly lower for both the 6082 materials.

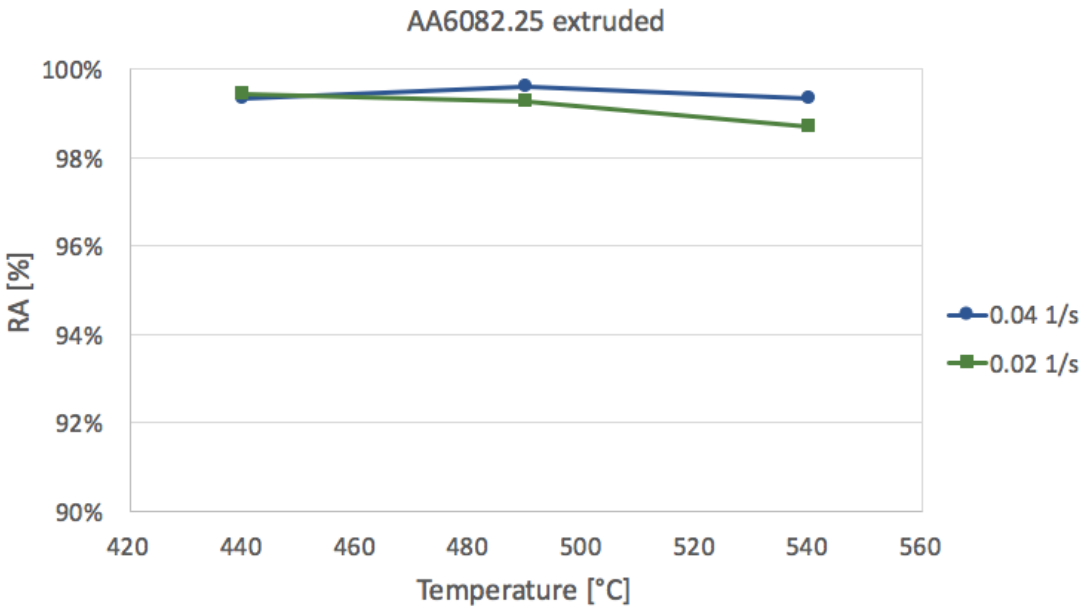

(a)

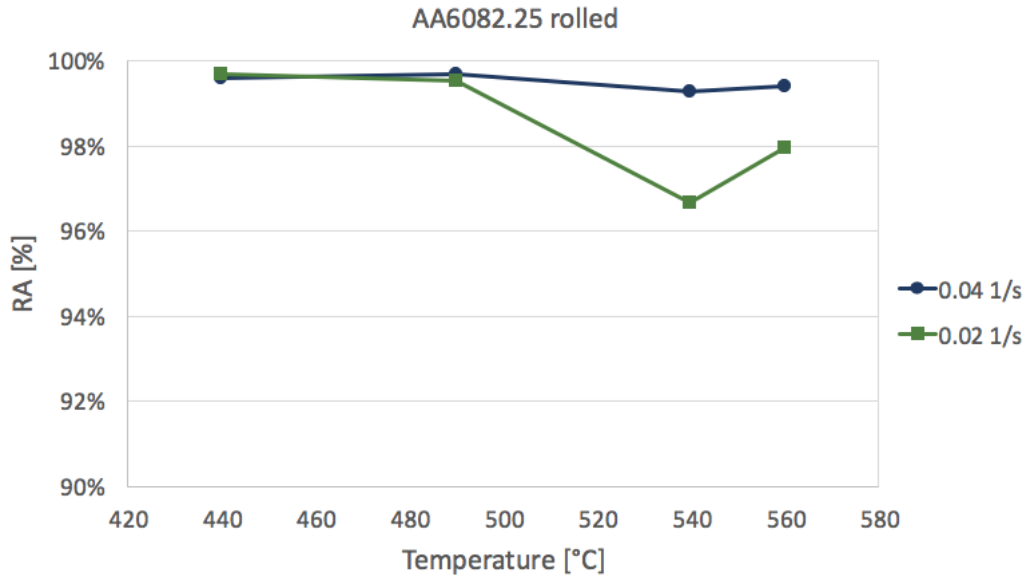

(b)

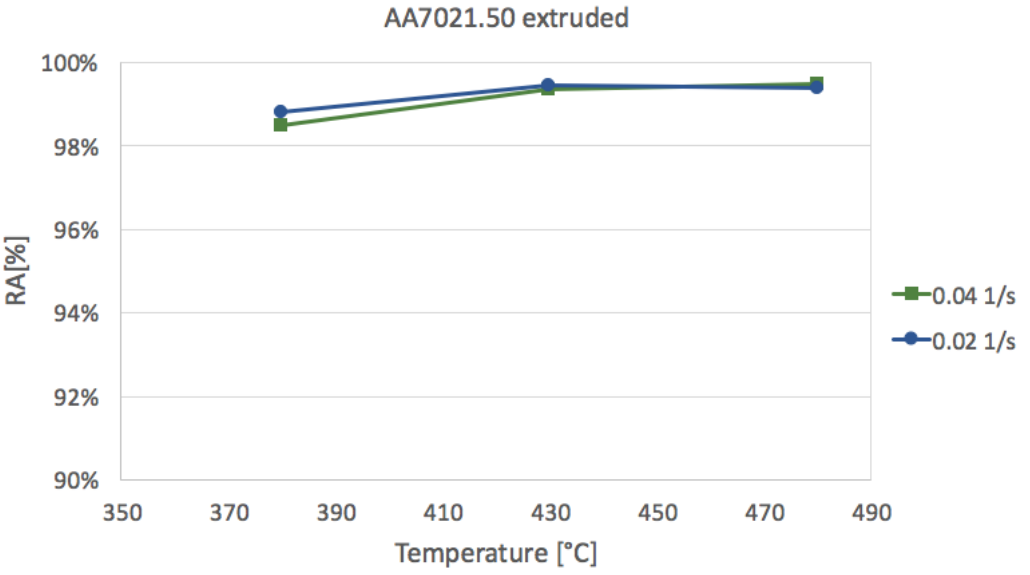

(c)

Figure 4.8: %RA as a function of temperature and strain rate.

Table 4.4: %RA for the samples deformed at 0.002 s^{-1}.

Material	**AA6082.25 extruded**	**AA6082.25 rolled**	**AA7021.50 extruded**
%RA	75.4	73.2	99.3

The measured maximum true strain in the diffuse necks is presented in figures 4.9-4.11. For both the extruded materials, this strain increases with increasing temperature, and the achievable strain is consistently higher for the 7021 extruded material than for the 6082 extruded material. For the 6082 rolled material, the maximum strain in the diffuse neck is relatively constant with temperature, except for deformation at 490°C at the strain rate 0.04 s^{-1} where this strain is slightly enhanced. For the 6082 extruded material, the achievable strain is not significantly affected by strain rate. For the 7021 extruded material, the lower strain rate gives a slightly but consistently higher strain in the diffuse neck. Note that there will be inaccuracies in these measurements as the onset of local necking is estimated visually.

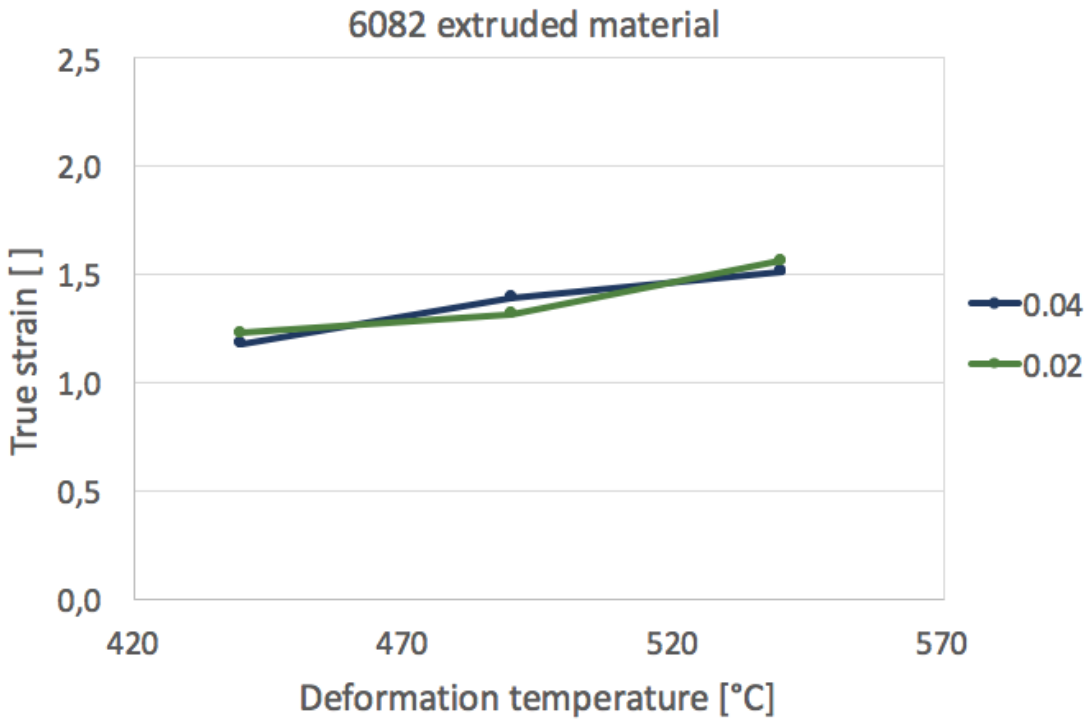

Figure 4.9: True strain in the diffuse neck for the AA6082.25 extruded material.

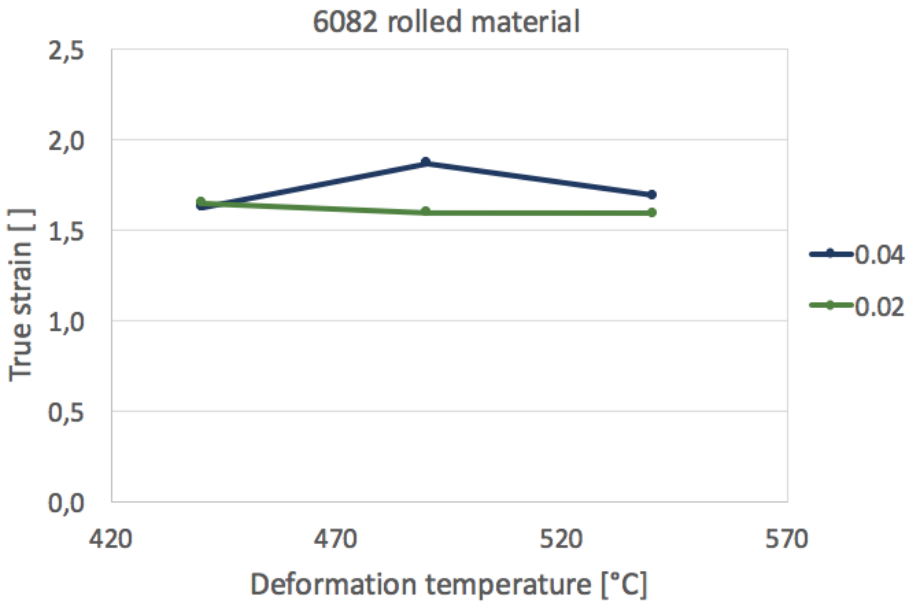

Figure 4.10: True strain in the diffuse neck for the AA6082.25 rolled material.

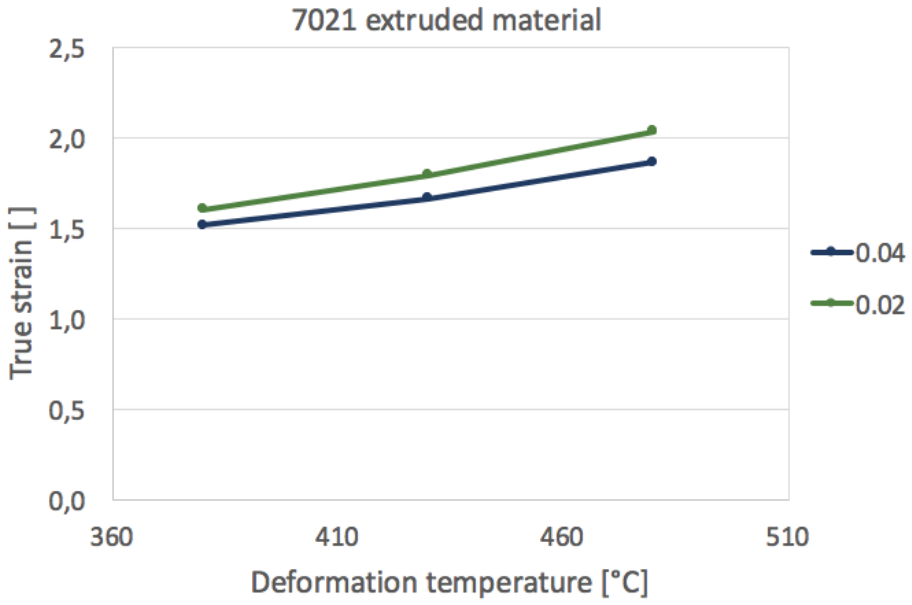

Figure 4.11: True strain in the diffuse neck for the AA7021.50 extruded material.

Corresponding trends can be inferred from the true stress–strain curves attached in Appendix D. It can be observed that the the true strain at fracture increases with increasing temperature for all materials even though there is a certain scatter of the strain at fracture between the parallel samples. The exception is the rolled 6082 material deformed at 560°C, where the

average fracture strain does not seem larger than for the samples deformed at 540°C. The increase in fracture strain with temperature is however least for the 6082 rolled material, and most severe for the 7021 material.

4.2.2 Gleeble testing

Samples of the rolled AA6082.25 material were deformed with the Gleeble Thermal System in order to obtain an indication of the formability properties at higher strain rates. The engineering stress–strain curves obtained with a strain rate of 2 s^{-1} is presented in Figure 4.12. The flow stress of the material increases with decreasing temperature. Note also that the engineering stress increases after the onset of plastic deformation.

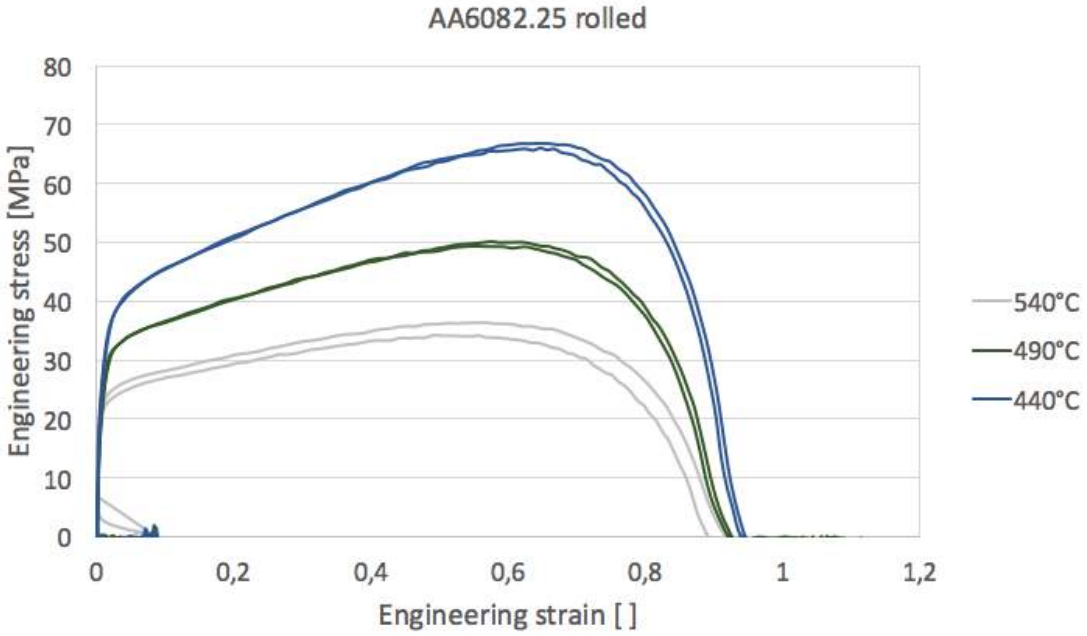

Figure 4.12: Engineering stress–strain curves for samples deformed with the Gleeble System.

The measured area reductions at fracture for the Gleeble tests are presented in Figure 4.13. All samples had very large area reductions. Keeping in mind that the precision in the fracture area measurements is limited both due to the irregular shape of the fracture surfaces and due to the remarkably narrow fracture areas, the % area reduction at fracture vary very little with temperature.

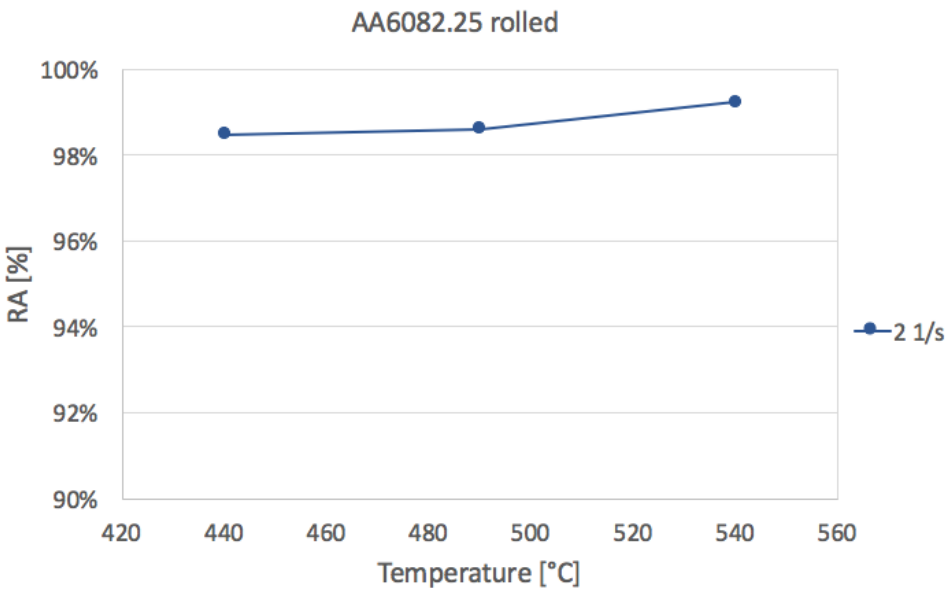

Figure 4.13: %RA as a function of deformation temperature and strain rate for samples deformed with the Gleeble system.

4.2.3 Fractography

Fractography of the fractured surfaces was performed in order to assess the fracture mechanisms at the relevant temperatures and strain rates. Some selected pictures of the fracture surfaces from the tests carried out at strain rates 0.02 and 0.04 s^{-1} are presented in figures 4.14 - 4.16. The overview pictures (a) represents the typical observed shapes of the fracture areas. Similar shapes were observed for all samples. Representative pictures of the middle of the fracture surfaces with enhanced magnification (b) reveals dimples. Regions where the fracture surfaces were smooth without dimples were observed in some corners and edges. The thickness of the fracture areas was observed to vary slightly, however, no clear pattern was recognized.

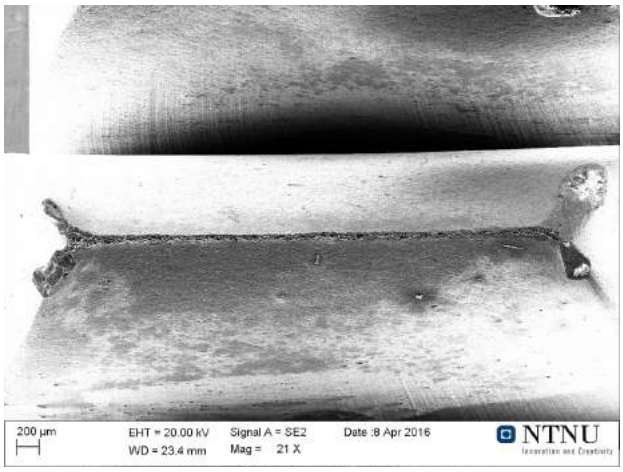

(a)

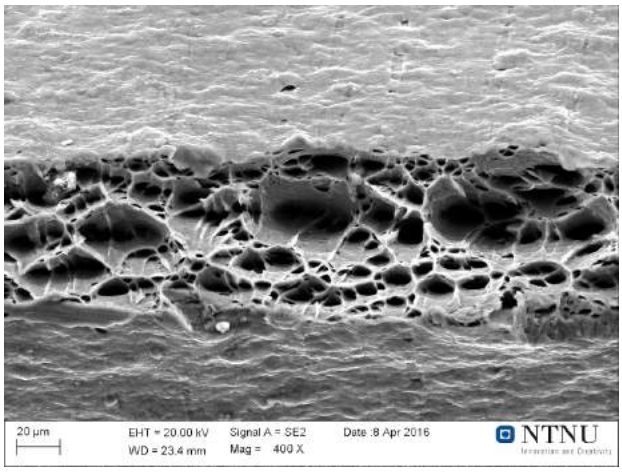

(b)

Figure 4.14: Representative fractography of the AA6082.25 extruded material.

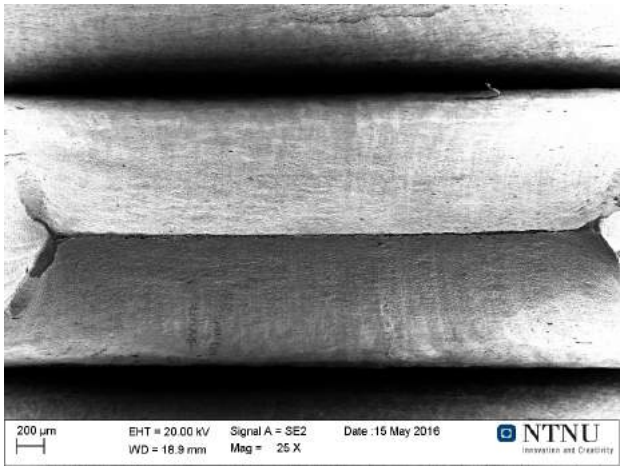

(a)

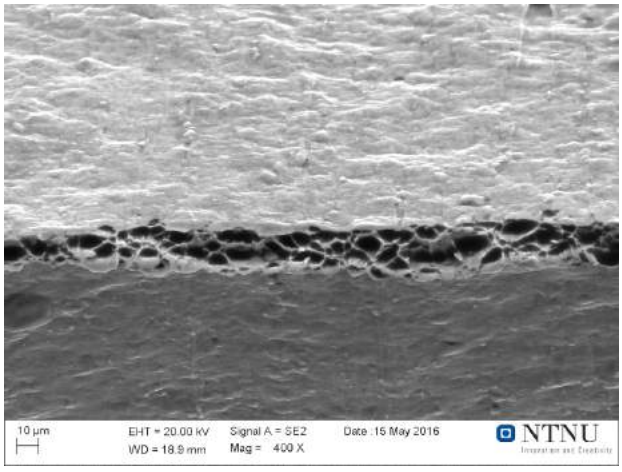

(b)

Figure 4.15: Representative fractography of the AA6082.25 rolled material.

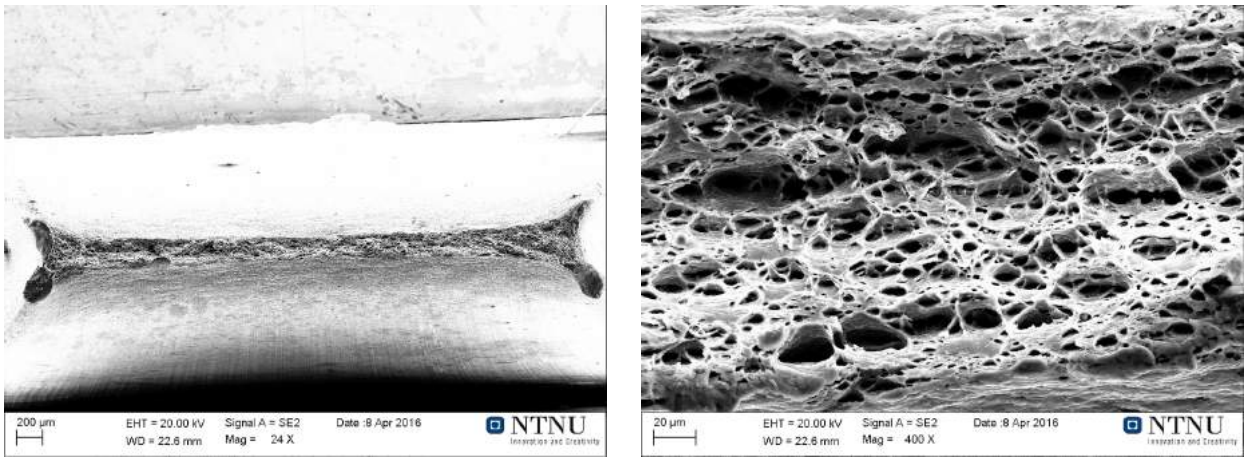

(a) (b)

Figure 4.16: Representative fractography of the AA7021.50 extruded

Pictures of the fracture surfaces of the single samples deformed at the extra low strain rate (0.002 s^{-1}) is presented in figures 4.17-4.19. The pictures with low magnifications (a) have a ductile appearance for all samples. The fracture surface of the 7021 material also appear ductile at higher magnification. For both the 6082 materials, some distinctive features can be seen at the higher magnifications. For the 6082 rolled material (Figure 4.17), the framed area could mark a previous grain boundary, and the arrow marks an apparent grain node. For the 6082 extruded material (Figure 4.18), the surface is covered in tiny rounded bumps. The arrows indicate a more diffuse boundary, possibly a subgrain boundary.

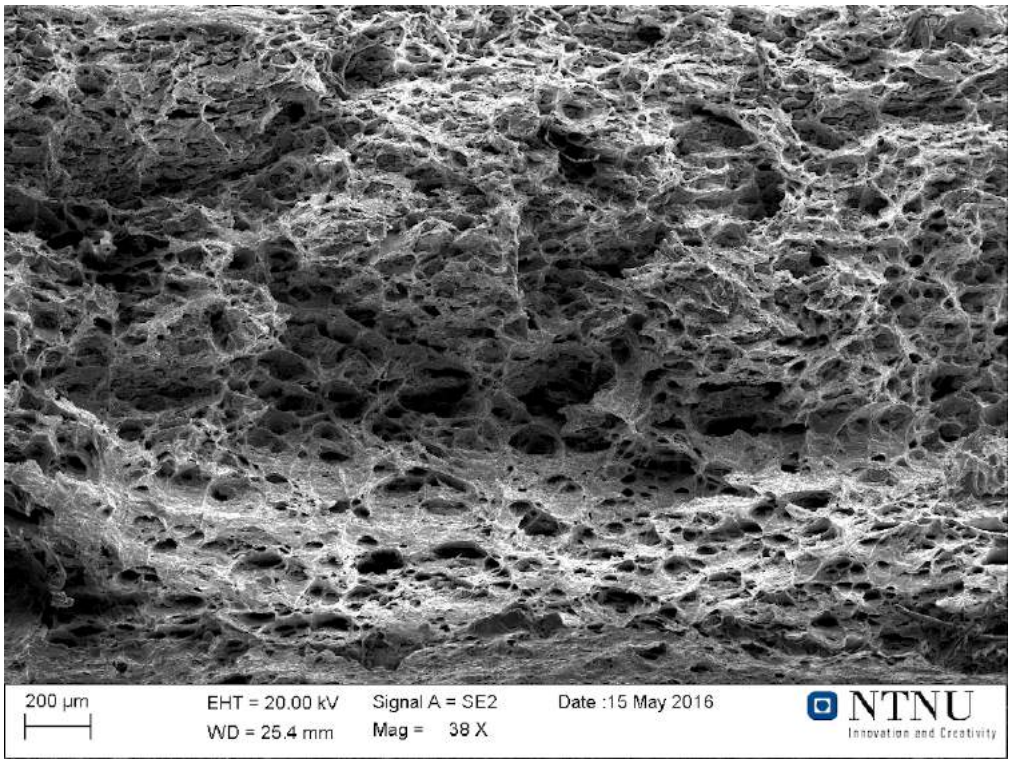

(a)

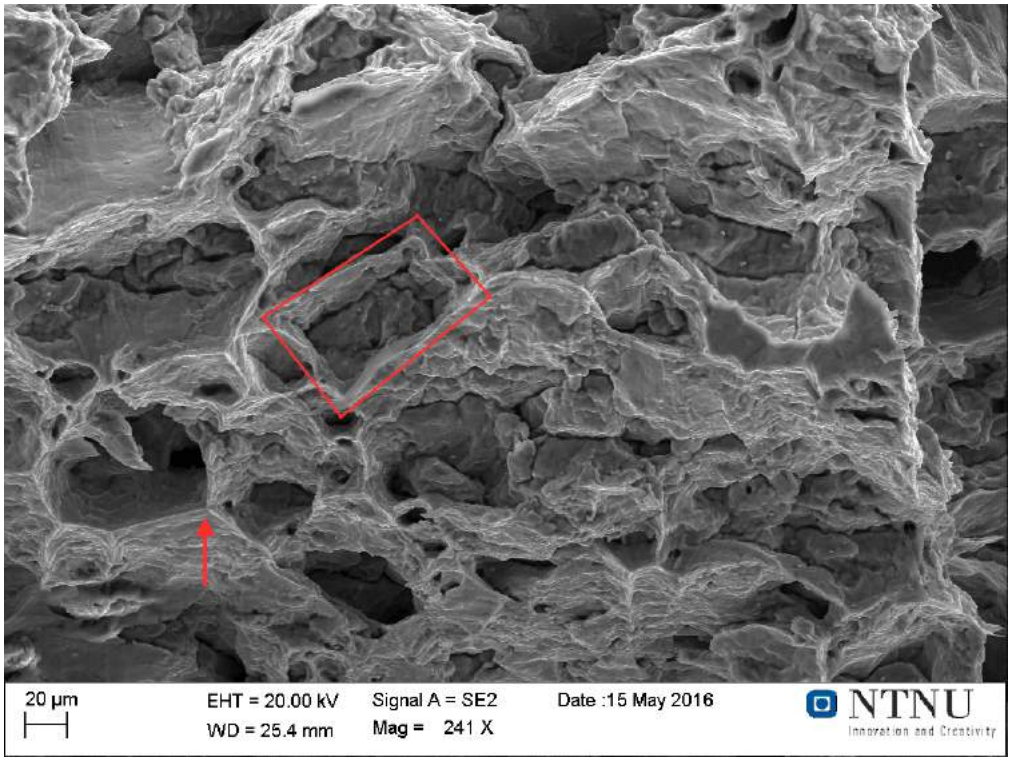

(b)

Figure 4.17: 6082 rolled, deformed at 540°C.

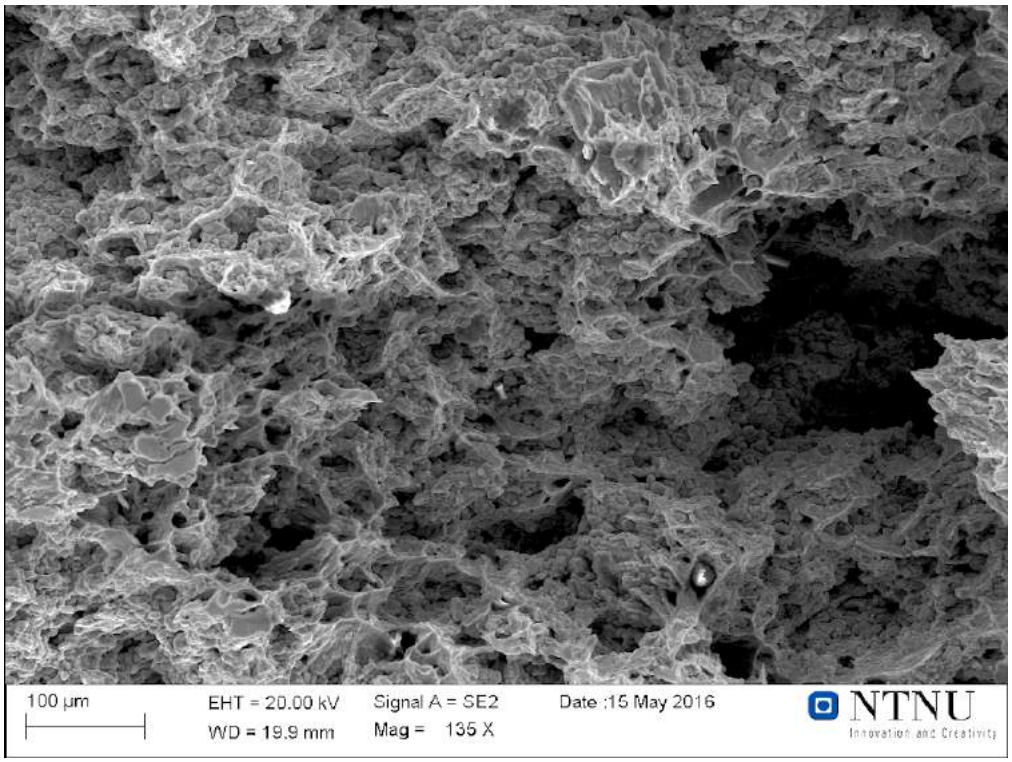

(a)

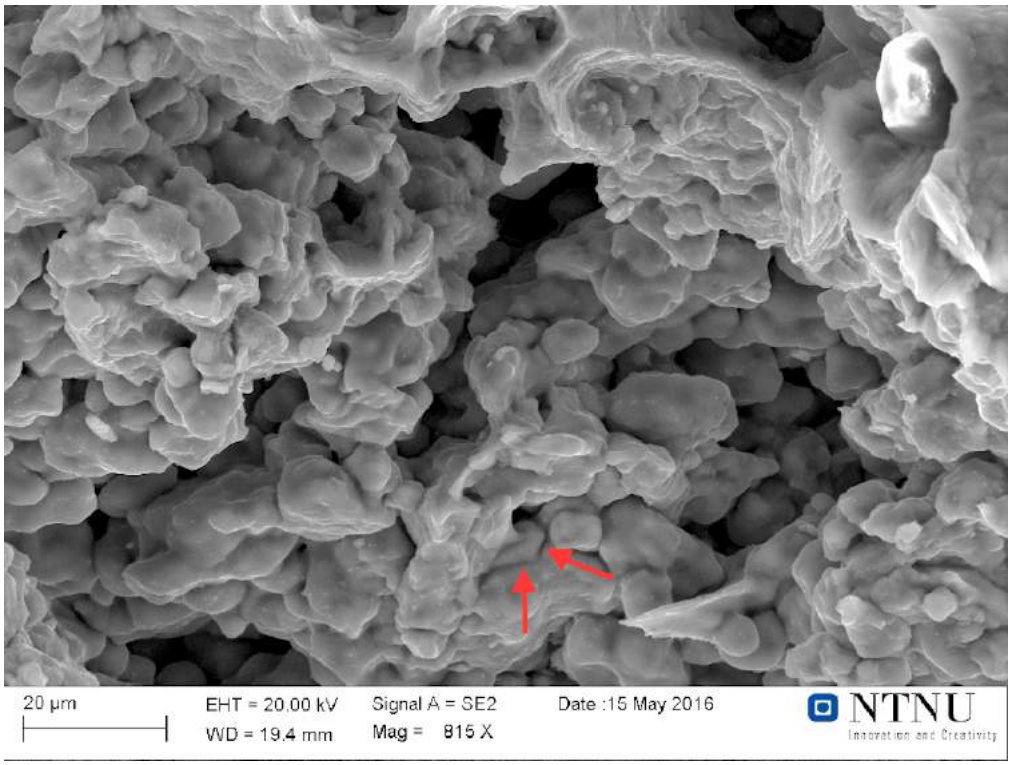

(b)

Figure 4.18: 6082 extruded, deformed at 540°C.

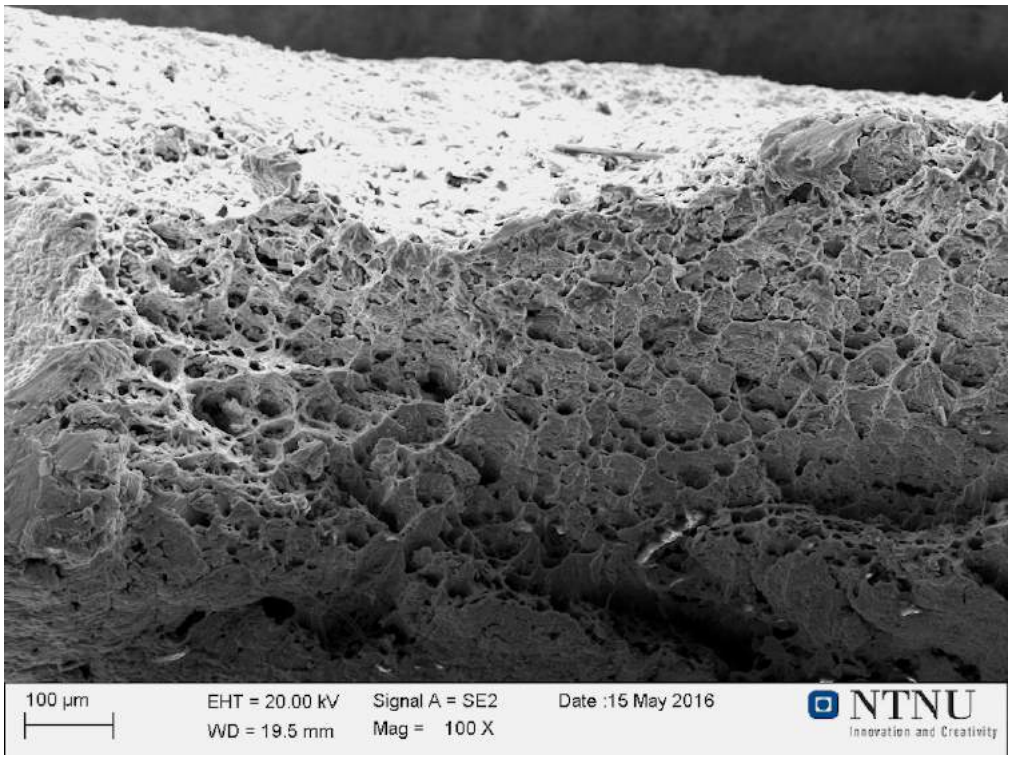

(a)

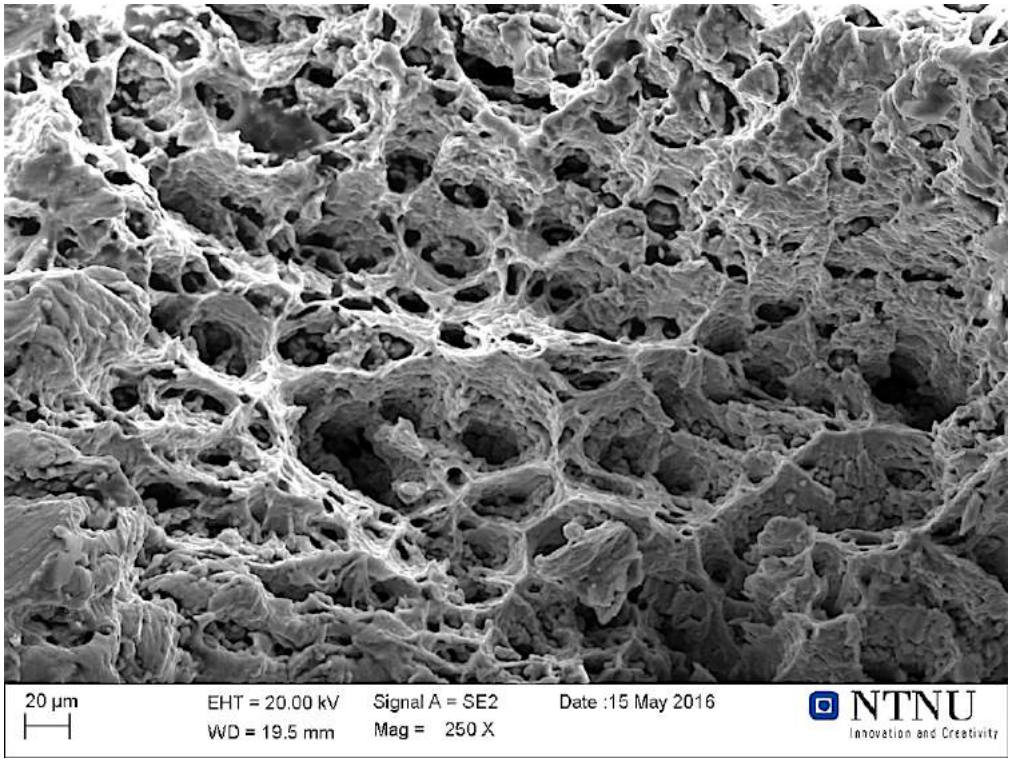

(b)

Figure 4.19: 7021 extruded, deformed at 480°C.

4.3 Microstructure evolution

Experiments were conducted in order to elucidate how deformation at conditions relevant for press form hardening affects the microstructure of the investigated materials.

4.3.1 Heat treatment without deformation

Samples were heat treated without deformation in order to reveal the grain structure of the materials prior to deformation but after solution heat treatment.

Figure 4.20 displays the grain structure of the 6082 rolled sample heat treated at 540°C. No recrystallization is observed as the fibrous grain structure observed in the base material is preserved. The same observations were made for all samples heat treated below 540°C. The grain structure of the sample heat treated at 560°C is presented in Figure 4.21. It can be seen that a surface layer of approximately 400 µm is recrystallized, while the fibrous grain structure observed in the base material is preserved elsewhere in the sample.

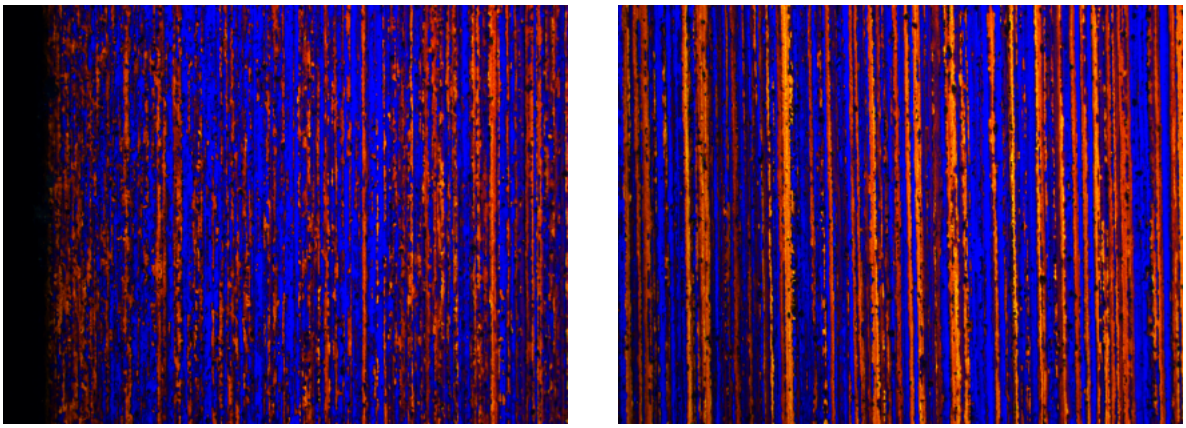

(a) Edge of sample. (b) Middle of sample.

Figure 4.20: Extruded AA6082.25, heat treated at 540°C

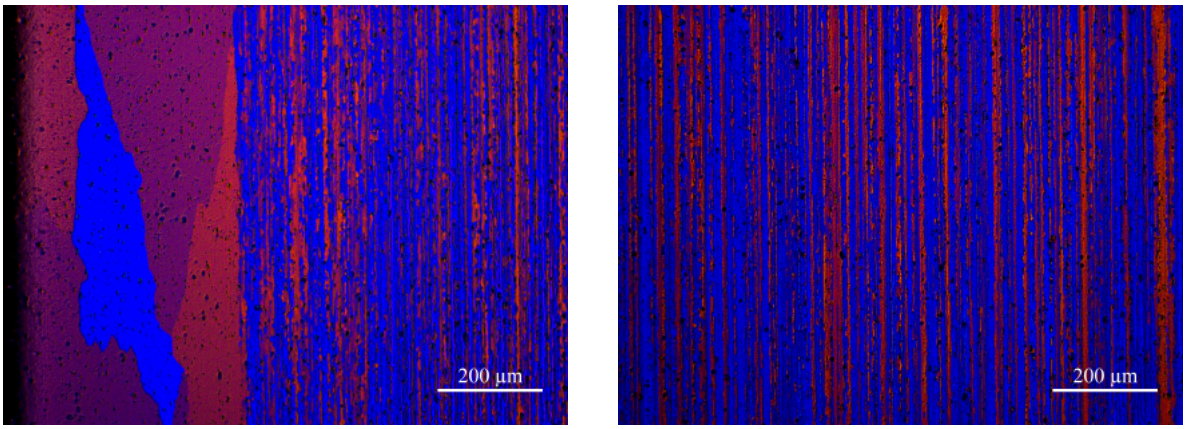

(a) Edge of sample. (b) Middle of sample.

Figure 4.21: Extruded AA6082.25, heat treated at 560°C

Figure 4.22 displays the grain structure of the 6082 rolled sample heat treated at 560°C. It can be seen that the grains have recrystallized both in the middle and at the edge of the samples as the grains are closer to equiaxed and have rounded boundaries. However, some traces of the preceding deformation structure can be recognized as the grains still are slightly elongated in the rolling direction. Recrystallization was observed in all samples heat treated at temperatures down to 460°C. The grain structures were similar in all samples. No significant or abnormal grain growth was observed in any samples.

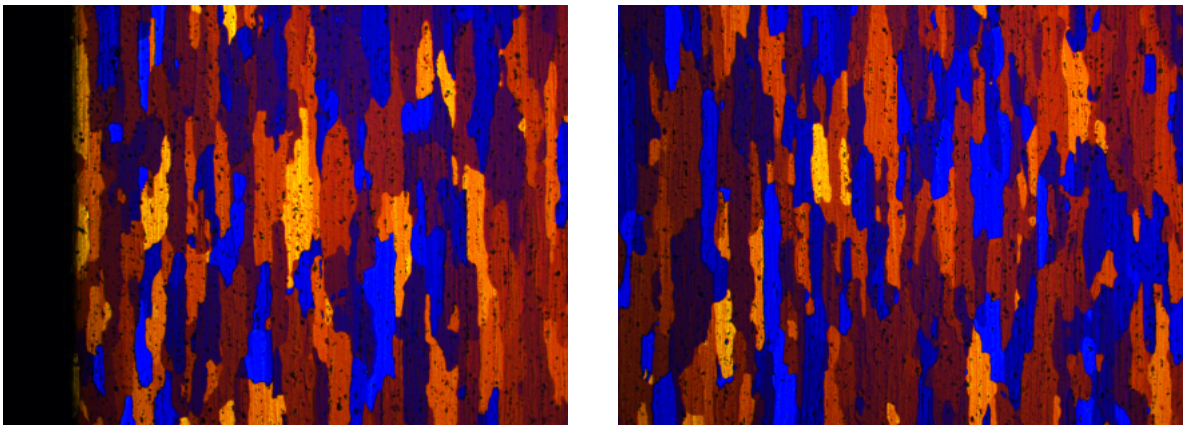

(a) Edge of sample. (b) Middle of sample.

Figure 4.22: Rolled AA6082.25, heat treated at 560°C

Figure 4.23 presents the grain structure of the 7021 extruded sample heat treated at 500°C. No recrystallization can be seen in the surface layer or in the bulk of the sample, as the deformed grain structure observed in the base material is preserved. The grain structure was similar for all samples heat treated at temperatures down to 400°C.

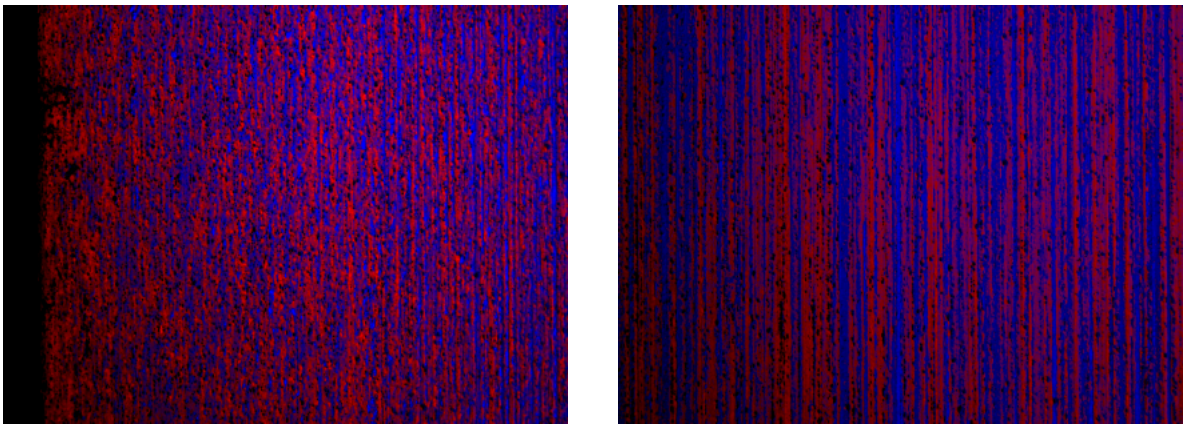

(a) Edge of sample. (b) Middle of sample.

Figure 4.23: Extruded AA7021.50, heat treated at 500°C

Figure 4.24 shows the grain structure of the 7021 rolled sample heat treated at 500°C. No recrystallization can be seen, as the grain structure is still fibrous as in the base material. The grain structure was similar for all samples heat treated at temperatures down to 400°C. Note that the small black dots seen in the anodized base material are no longer present.

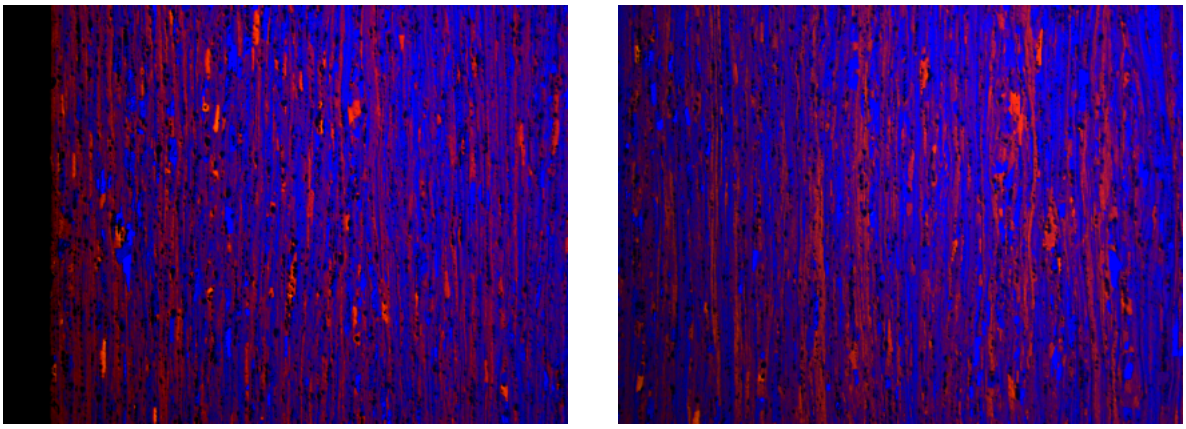

(a) Edge of sample. (b) Middle of sample.

Figure 4.24: Rolled AA7021.50, heat treated at 500°C.

4.3.2 Recrystallized texture

As the AA6082.25 rolled material recrystallized at the relevant temperatures, the texture after solution heat treatment was investigated. The texture of the recrystallized material is presented in Figure 4.25. The texture is practically random as the maximum intensity represented by the darkest red color is 2.5 times random.

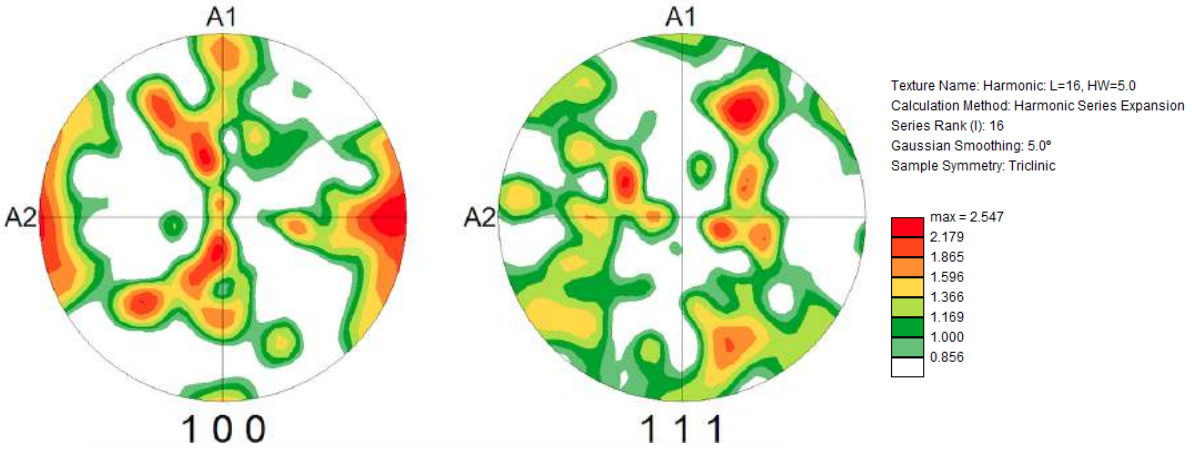

Figure 4.25: Texture of the recrystallized AA6082.25 rolled material.

4.3.3 Hot tensile deformation

The grain structure of samples deformed at conditions relevant to press form hardening was investigated and compared with the grain structure of the materials after solution heat treatment. The 7021 rolled material was not investigated. The results are presented in figures 4.26 - 4.28.

For both the 6082 and 7021 extruded materials, the grains were exceedingly long and narrow at the onset of deformation, thus a further advancement of this deformation structure would be difficult to observe. No substantial effects were observed, however, the grain boundaries seem somewhat more rugged in the deformed samples. The grain structure also seems slightly more broken up, as several small "grain-pieces" can be seen. These effects are most pronounced in the samples deformed at the lowest strain rate (0.002 s^{-1}) and highest temperature (540°C). No recrystallization was observed, however it is emphasized that the surface layer associated with extrusion was removed during machining of these samples.

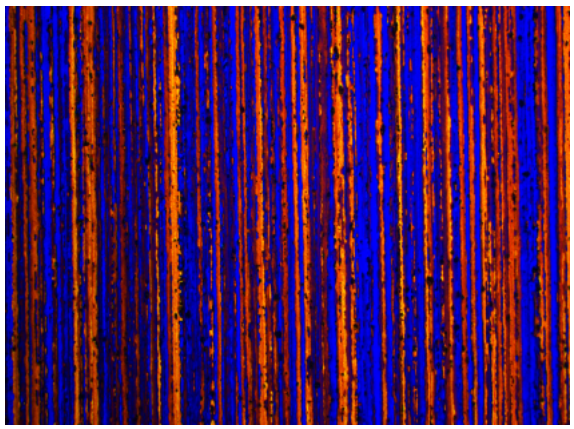

(a) Solution heat treated at 540°C.

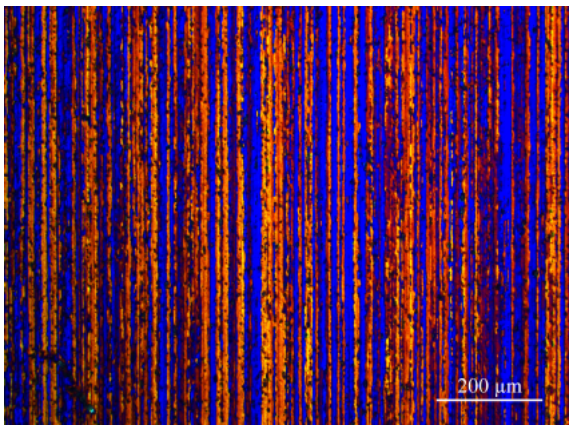

(b) Deformed at 440°C.

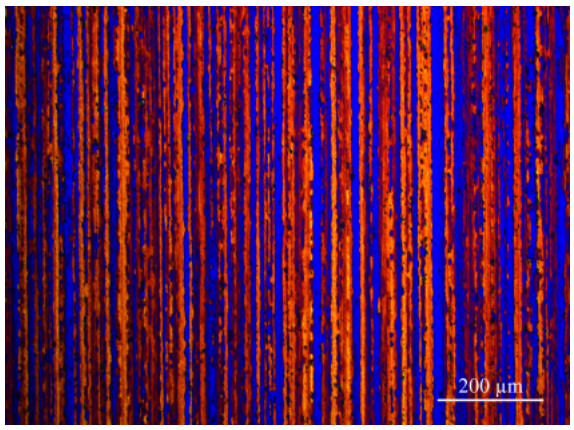

(c) Deformed at 540°C.

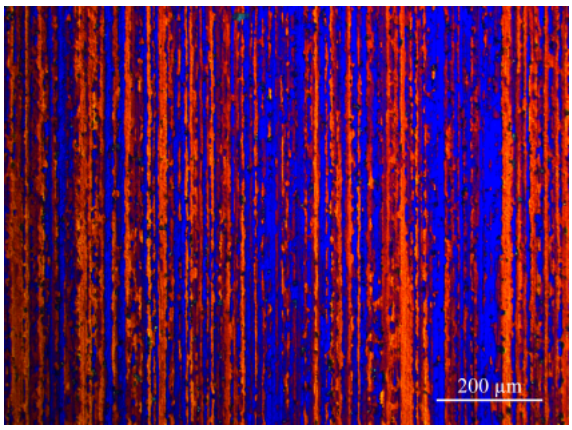

(d) Deformed at 540°C with low strain rate.

Figure 4.26: Grain structures of the extruded AA6082.25 material.

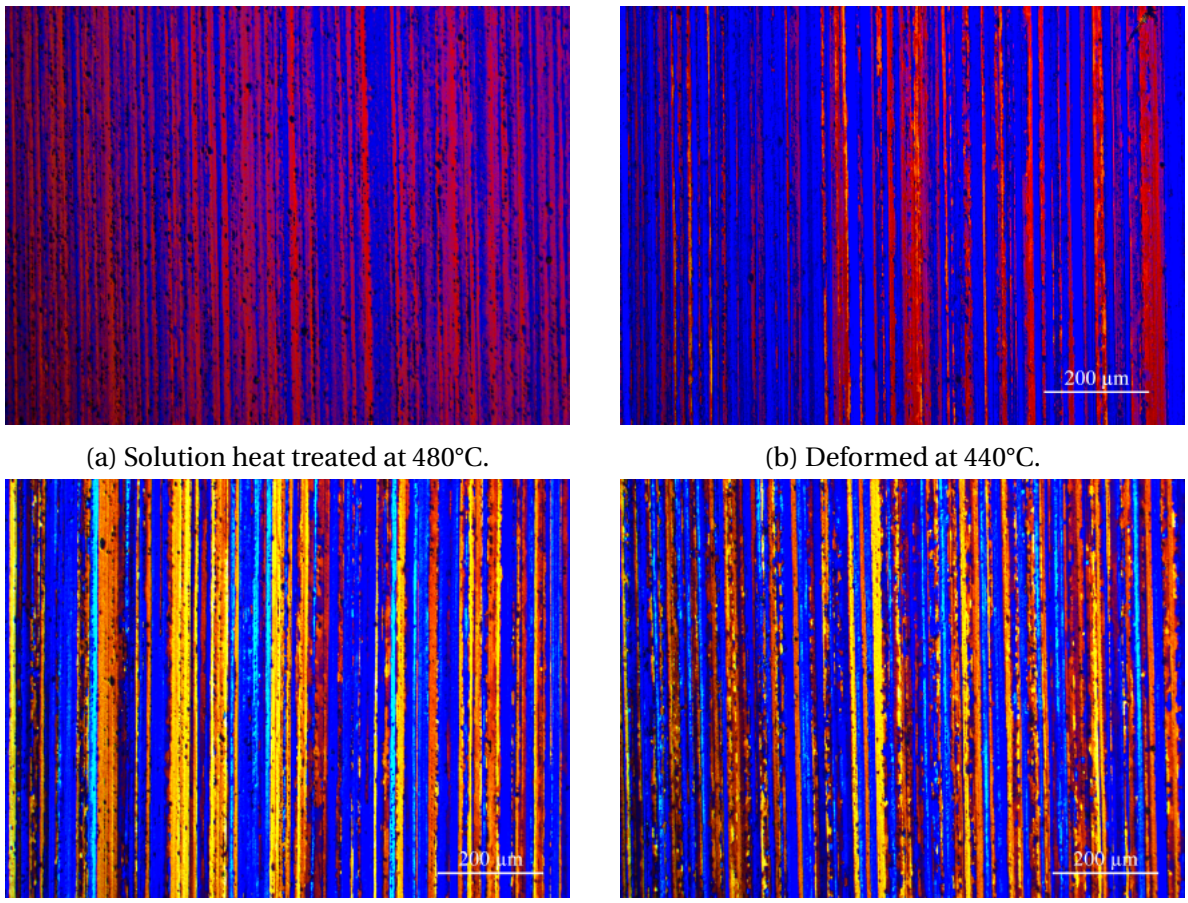

(a) Solution heat treated at 480°C.

(b) Deformed at 440°C.

(c) Deformed at 480°C.

(d) Deformed at 480°C with low strain rate.

Figure 4.27: Grain structures of the extruded AA7021.50 material.

For the 6082 rolled material, a distinct effect of deformation could be observed on the grain structure. The recrystallized grain structure present after solution heat treatment is visibly stretched out along the tensile axis after deformation. The grains also seem larger after deformation. No conclusive differences between deformation at high or low temperature and high or low strain rates is observed.

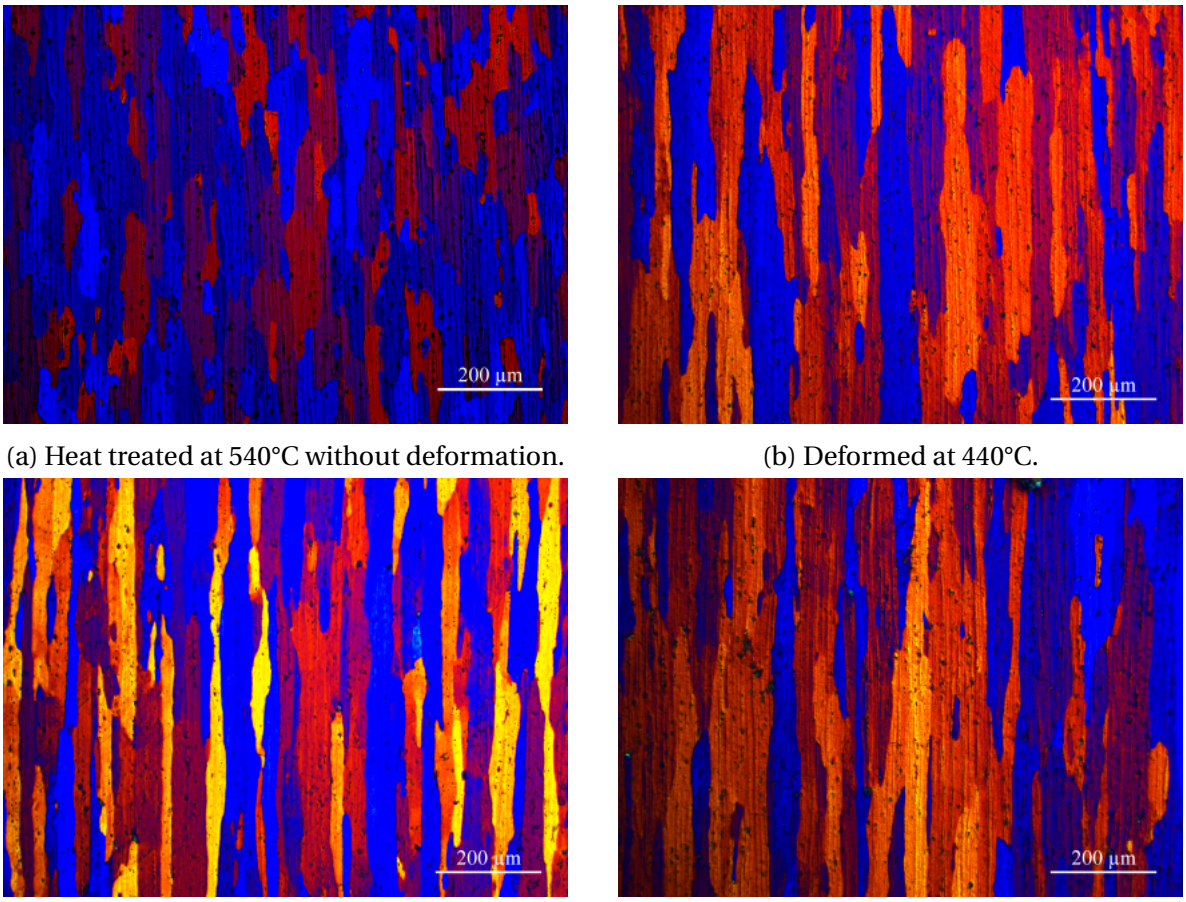

(a) Heat treated at 540°C without deformation.

(b) Deformed at 440°C.

(c) Deformed at 540°C.

(d) Deformed at 540°C with low strain rate.

Figure 4.28: Grain structures of the rolled AA6082.25 material.

4.4 Precipitation potential

Experiments were conducted in order to get an indication of the effect of deformation at high temperatures on the subsequent precipitation behavior.

4.4.1 Peak hardness

Peak hardness was identified for both 6082 materials, and for the rolled 7021 material. The obtained artificial ageing curves are presented in Figure 4.29. For both the AA6082.25 materials, peak hardness was reached after ageing for 2 hours at 190°C. For the AA7021.50 material, peak hardness was obtained after ageing for 5 hours at 100°C and subsequently for 6 hours at 150°C. The corresponding peak hardness values are presented in Table 4.5.

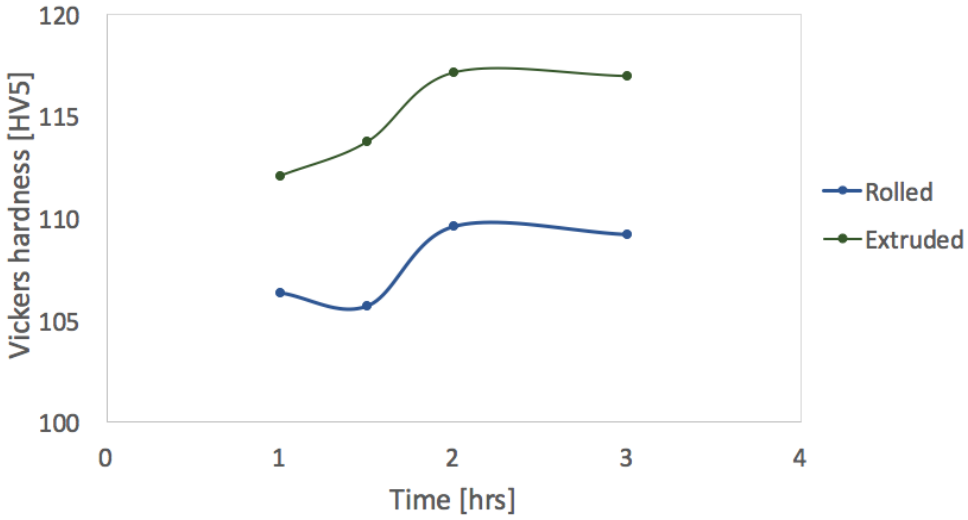

(a) AA6082.25 materials aged at 190°C.

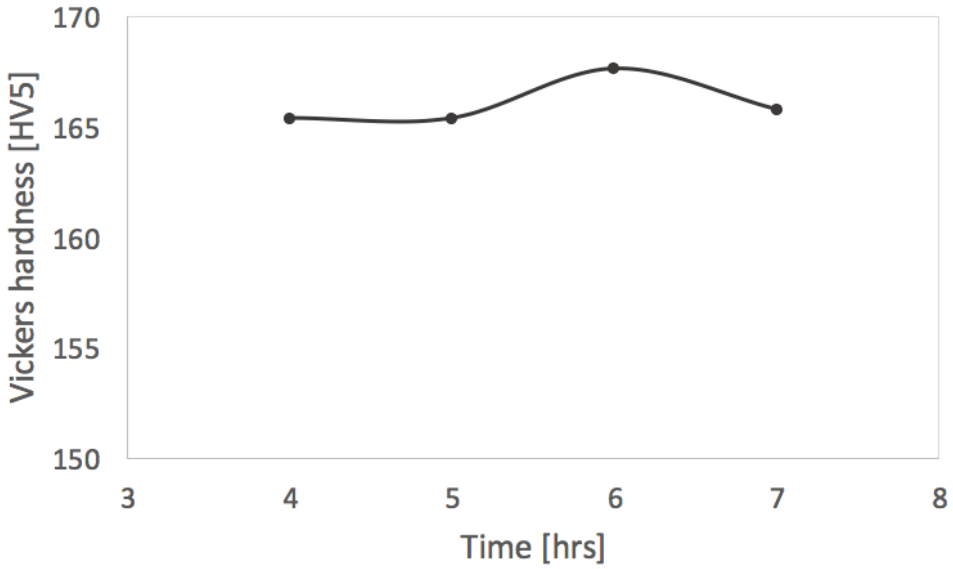

(b) AA7021.50 materials, aged at 100°C for 5 hours and further aged at 150°C.

Figure 4.29: Obtained artificial ageing curves.

Table 4.5: Peak hardness values from artificial ageing curves.

Material	**AA6082.25 extruded**	**AA6082.25 rolled**	**AA7021.50 extruded**
Peak hardness [HV5]	117.1	109.6	167.7

4.4.2 Hot tensile deformation

Samples were deformed in the hot tensile test rig and subsequently age hardened. The approach with solution heat treatment in the tensile rig (called approach 1) was observed to keep the samples below the solution heat treatment temperature for several minutes (see Section 4.2). As significant precipitation is likely to occur prior the artificial age hardening, the results regarding the precipitation potential for these samples were thus discarded.

Similar conclusions were drawn for the samples that were solution heat treated in a salt bath prior to testing (approach 2) as heating to test temperature was slow and removing the hot samples from the test rig after deformation was difficult. Consequently, the samples spent much time at high temperatures below the solution heat treatment temperature prior to quenching and subsequent age hardening. Results regarding fine differences in precipitation potential would not be observable, thus the results from the samples deformed with this approach was also discarded.

4.4.3 Gleeble tensile deformation

Samples were deformed in the Gleeble Thermal System and subsequently age hardened. The obtained temperature cycles are presented in Figure 4.30. It can be seen that the samples deformed at the lower temperatures spend more time between the solution heat treatment temperature and 200°during the subsequent cooling than the samples deformed at 540°C.

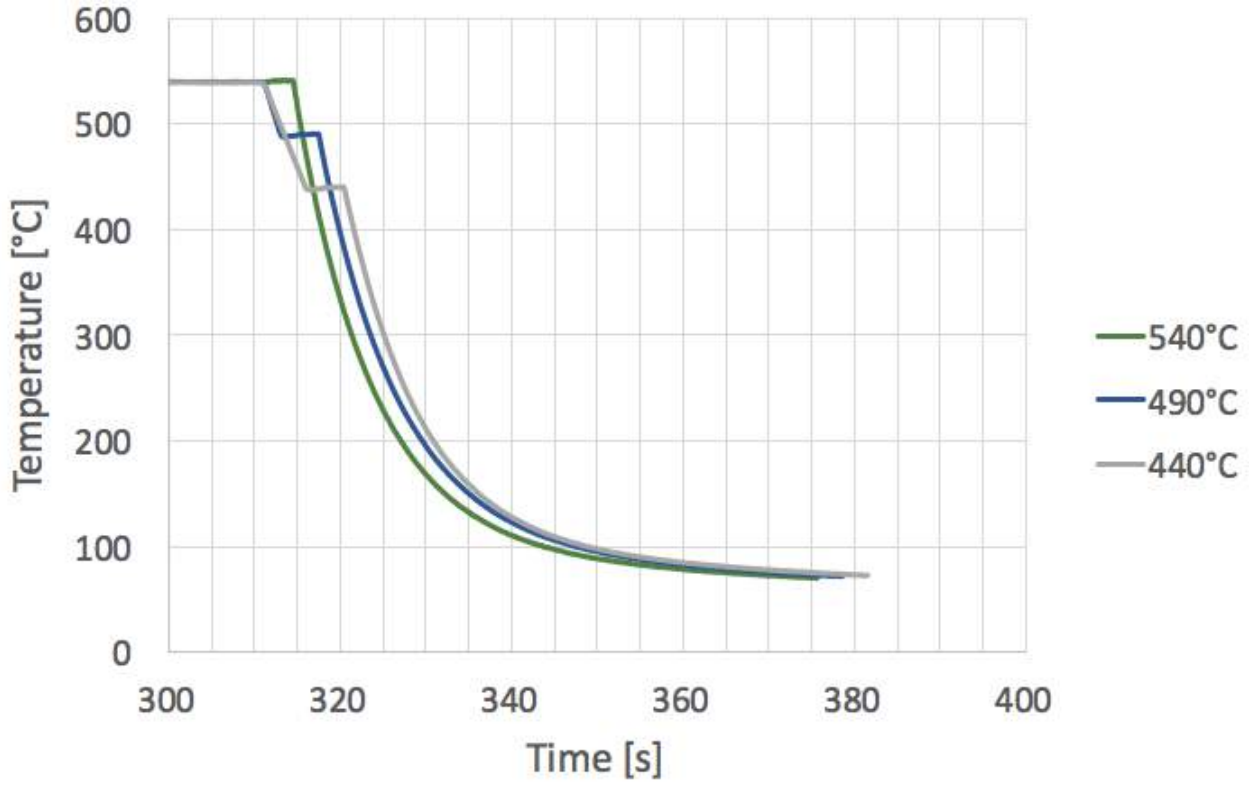

Figure 4.30: Temperature cycles for the different test temperatures.

The hardness of the samples treated with these temperature cycles (Figure 4.30) without applying any deformation is presented in Figure 4.31. The variation in hardness with test temperature is within the standard deviations. The hardness of the samples deformed at different temperatures and strain rates is presented in Figure 4.32. All samples have lower hardness than the peak hardness of 109.6 HV5 obtained with ideal heat treatment described in Section 4.4.1. As the standard deviation of these measurements is rather large, no definite trend can be inferred. However, there are slight indications of increasing hardness after artificial age hardening with increasing deformation temperature.

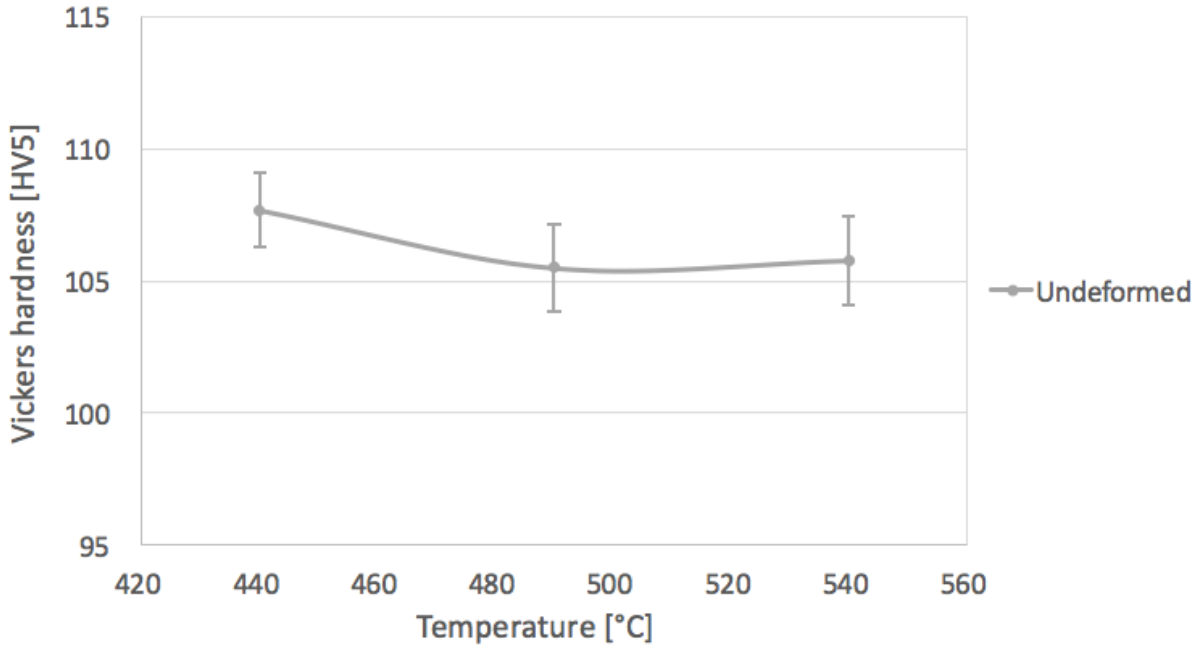

Figure 4.31: Hardness of the undeformed samples treated with the same temperature cycles as the deformed samples. Plotted with standard deviation.

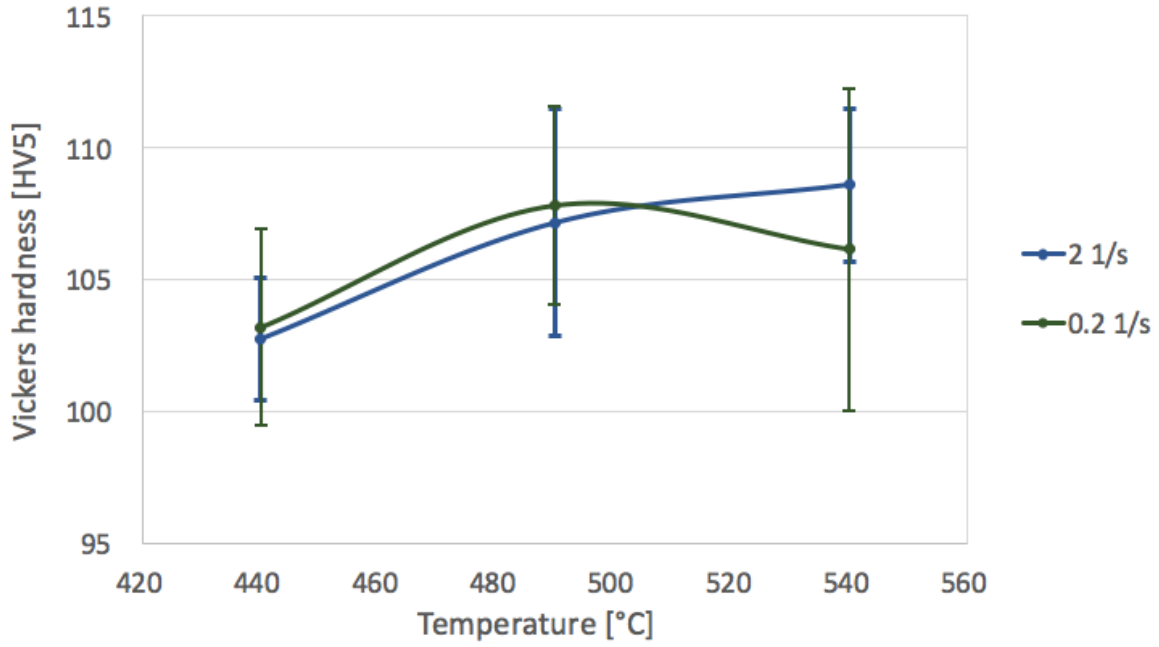

Figure 4.32: Hardness of samples deformed at different temperatures and strain rates. Plotted with standard deviation.

The electrical conductivity of the corresponding samples is presented in figure 4.33. The electrical conductivity is lower in the undeformed samples. It can be seen that the electrical conductivity is stable or increases with increasing deformation temperature.

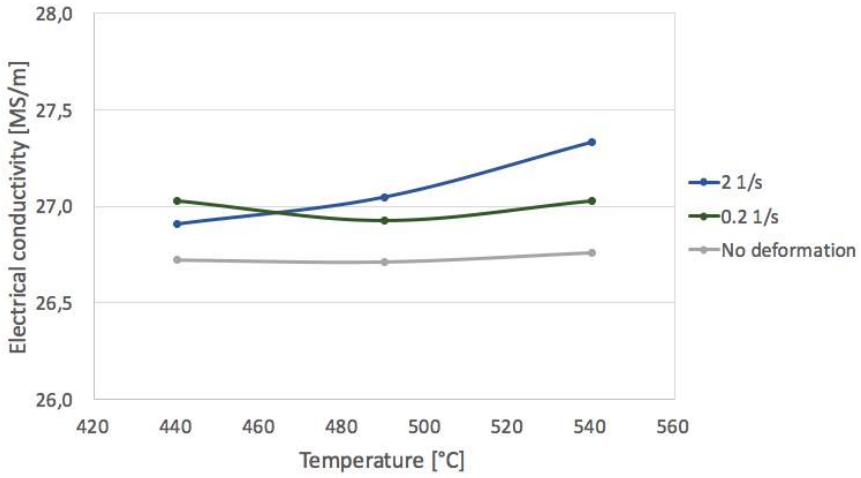

Figure 4.33: Electrical conductivity of samples deformed at different temperatures and strain rates.

The strain in the center of the deformed samples is presented in Figure 4.34. Note that the strain in the center of the samples is lower in the samples deformed at the higher temperatures.

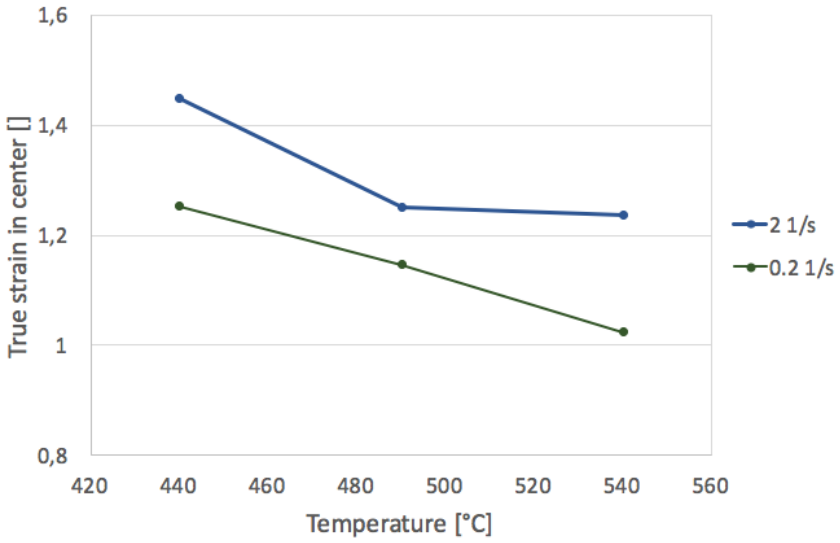

Figure 4.34: Strain in the center of samples deformed at different temperatures and strain rates.

5 Discussion

In this section, the results presented in Section 4 will be discussed and explained with basis in the theory presented in Section 2. The observed material phenomena will be discussed first, followed by a discussion of the implications of the observed effects for the suitability of the material for processing by press form hardening. As there is not much work done regarding the material response during the specific conditions relevant for press form hardening, the results will mainly be discussed based on general theory concerning the relevant mechanisms.

5.1 The base material

A characterization of the base materials was conducted. The observed grain structures of the base materials are as expected from the processing conditions, as it can be seen that the previous casting structures are more drawn out in the extruded materials than in the rolled materials. This can also be inferred from the particle structures, where the particles in the extruded materials are drawn out in distinct lines during extrusion. The same alignment of particles is not observed in the rolled materials, however, bands of higher and lower particle densities exist. This is probably bacause the primary particles often precipitate on the grain boundaries and between dendrites during casting [54]. Subsequent rolling eliminates the primary grain structure, while the original particle structure persists, though smeared out in the rolling direction.

The rolled 7021 material contains significantly more particles than the other materials. The EDS analysis revealed two particle types; one with a high Fe content and one with a high Zn content. The amount of particles was severely reduced after solution heat treatment. It is thus probable that the low processing temperature and slow cooling after hot rolling has caused Zn-rich transition or equilibrium phases to precipitate in the rolled 7021 material, in addition to the already existing Fe based primary particles. As corresponding processing conditions were used for the rolled 6082 material, transition or equilibrium phases should also be present in this material. However, as Mg_2Si typically dissolves in water, it is likely that these particles

escaped during sample preparation. The Mg_2Si phase would thus not be observed by EDS, it would rather be observed by pores in the surface. These pores can be seen by looking closely at the pictures of the particle structure (Figure 4.2), or in the high magnification secondary electron pictures obtained during EDS-scanning (attached in Appendix C). The amount of transition or equilibrium phases is larger in the 7021 material as this material is more heavily alloyed than the 6082 material.

Neither of the materials have particularly strong textures, especially the rolled materials have weak to no texture. The two extruded materials have very similar textures, thus it seems as the deformation and reduction ratio affects the resulting textures more than the alloying content and elements. The weak textures of the materials may serve as an indication that anisotropy not will cause considerable issues during forming, particularly as anisotropic properties were observed to diminish at high temperatures in the author's specialization project [52]. However, the anisotropy was not investigated directly in this study.

5.2 Formability

Tests were carried out in order to assess the flow behavior of the base materials of current interest at different temperatures and strain rates relevant to press form hardening. Results regarding the formability test procedure, deformation mechanism, steady-state flow stress, strain rate sensitivity, strainability and fracture at the relevant forming conditions is discussed in this section.

5.2.1 Hot tensile test procedure

Several test procedures were attempted for the hot tensile testing, as described in Section 3.2.1. For the samples that were solution heat treated while mounted in the tensile rig, the main results were that it is not possible to produce a satisfactory temperature cycle with this approach. Cooling from the solution heat treatment temperature was most successfully done by opening the furnace door while monitoring the sample temperature. However, the air in the air circulation furnace could be cooled quickly, but the furnace chamber itself could not be cooled as rapid, thus once the test temperature was attained and the furnace door was closed,

the temperature quickly rose again. In order to provide a fairly stable temperature during straining, the temperature first had to be lowered 10 - 30°C below the target temperature. Subsequently the temperature rose again and became somewhat stable at the test temperature. As a result of this, the samples spent up to 3-4 minutes below the solution heat treatment temperature prior to deformation. It was thus not possible to achieve a temperature cycle that satisfactory simulated the temperature conditions in a press form hardening process with the available equipment. In addition, it was difficult to achieve a reproducible temperature cycle with this test procedure, and the experiments were very time consuming.

The test procedure where samples were solution heat treated in a salt bath and water quenched in advance of mounting in the tensile rig was neither fully ideal. Heating of the quite large samples in the air circulation furnace was not rapid, thus the state of the material would not be completely as quenched at the onset of deformation with this test procedure either. The results will thus be affected by precipitation of various transition phases prior to deformation (precedors of β or η depending on alloy). It was nevertheless easier to produce the same temperature cycle for each sample with this method, thus the results obtained with this test procedure have better reproducibility. These experiments were also significantly more efficient with respect to the time required per sample. No significant effects of precipitation prior to deformation were inferred from the results.

It was thus concluded that separate solution heat treatment prior to tensile testing was the preferable test procedure, thus the results following discussion is based on the results from these tests.

5.2.2 Deformation mechanism

For the samples hot tensile tested at strain rates 0.02 s^{-1} and 0.04 s^{-1}, the horizontal plateaus observed in the true stress–strain curves (exemplified in Figure 4.5) indicate that the dominant deformation mechanism is dislocation creep where dynamic recovery occurs [14, 27, 28]. The generation and annihilation of dislocations reach an equilibrium quickly after the onset of plastic deformation, thus any further strain hardening is continuously eliminated [14, 28]. The

steady-state plateaus appear very slightly curved with a maximum point around the middle of the horizontal region. This effect may possibly be assigned to the linear approximation to a constant true strain rate that gives a slightly higher than average true strain rate around the middle of the deformation, and a slightly lower than average true strain rate at the beginning and end of the deformation (see Figure 3.2b). However, the steady-state plateau in the 6082 rolled material appears more curved that what could be justified by the deviations from the ideal constant true strain rate. An explanation for the cause of this was not obtained in this work. Note that this is not an indication of work hardening, as the engineering stress–strain curves strictly decrease from the onset of plastic flow.

The fractography of the fracture surfaces indicated that some grain boundary sliding may occur during deformation of both the 6082 materials at the lowest strain rate of 0.002 s^{-1}. This is further discussed in Section 5.2.5. Notable grain boundary sliding may however occur without any significant contributions to the overall strain [14].

The engineering stress–strain curves for the samples deformed with the Gleeble system at the high strain rate of 2 s^{-1} was presented in Figure 4.12. It is desired to compare the stress–strain behavior of these samples with the true stress–strain curves obtained by hot tensile testing at the lower strain rates, however this is difficult as the deformation in the Gleeble System is inhomogeneous [51] (see Section 2.8). It is thus not possible to calculate the true stress level in the material because these calculations assume a uniform decrease in cross-sectional area over the whole sample length, which is in conflict with the situation during this type of testing. Therefore, the engineering stress is presented, where the true stress in the material is progressively underestimated as the decrease in cross sectional area is not accounted for.

Another challenge in comparing these results is that the hot tensile testing is performed with constant true strain rate (approximately). In Gleeble deformation, the nonuniform deformation makes it impossible to achieve a constant true strain rate, thus the test is carried out with a constant crosshead displacement velocity estimated to give an average strain rate of 2 s^{-1} over the complete deformation. In reality, the true strain rate (averaged over the sample

length) will thus decrease throughout the test. For a strain rate sensitive material, this means that the presented engineering stress will be progressively lower than what it would be if the test was carried out at constant true strain rate.

Both these discussed factors predict a progressive underestimation of the stress level in the samples compared to the true stress–strain curves obtained with the hot tensile testing at constant true strain rate. Still, the engineering stress strain curves obtained with the Gleeble system displays a lasting increase in the load-bearing capacity of all samples after the onset of plastic deformation, while the true stress strain curves from the hot tensile testing displays a constant true flow stress quickly after the onset of deformation. This indicates that work hardening occurs at the high strain rate of 2 s^{-1}. It is expected from theory that increasing the strain rate at some point could lead to strain hardening, as increasing the strain rate increases the generation of dislocations, and at at a certain strain rate, the annihilation of dislocations cannot keep up the dynamic equilibrium that is characteristic for steady-state dislocation creep [14, 27, 28]. As diffusion mechanisms cannot sufficiently provide the dislocation mobility required for steady-state dislocation creep at this high strain rate, it is also possible that the deformation mechanism slightly shifts towards high temperature dislocation glide.

It can also be observed that the work hardening seems to increase with decreasing deformation temperature in the samples deformed with the Gleeble System. This could be explained as the dislocations become less mobile with decreasing temperature [27], thus annihilation of dislocations and then elimination of work hardening becomes slower at the lower temperatures. It is however difficult to quantify this effect. As seen from Figure 4.34, the strain in the center of a sample elongated 6mm with the Gleeble System increases with decreasing temperature. This means that the material volume that deforms during this deformation is smaller at the lowest deformation temperatures. This phenomenon may cause a larger underestimation of the flow stress at the lower test temperatures, as the cross sectional area in the deforming region will be smaller than during deformation at the higher temperatures. However, a smaller deforming volume will also cause an increased true strain rate in this material volume. Consequently, the true strain rate experienced by the material has in reality

been higher during deformation at the lowest temperatures, and this would cause an overestimation of the flow stress with increasing temperature. It is difficult to predict the magnitude of these effects, thus the variation in strain hardening rate with temperature cannot be quantified based on these results.

5.2.3 Steady-state flow stress and strain rate sensitivity

Figure 4.7 showed that the flow stress of all materials decreased with increasing temperature. Theory states that the shear modulus of metals decreases with increasing temperature [14], thus the friction stress in the slip systems is lowered at high temperatures. In addition, thermal fluctuations increase the dislocations' ability to surpass short range barriers [14], and as dislocation creep is thought to be the dominating deformation mechanism at these temperatures and strain rates, dislocations also overcome barriers like coherent precipitates, solute atoms and other dislocations by thermally assisted mechanisms involving diffusion [14]. Diffusion rates increase with increasing temperature [17], thus this mechanism becomes more effective with increasing temperature. The decrease in observed flow stress with increasing temperature concurs well with theory, and with the results obtained by Fan et al. [55] who investigated the flow stress of an Al-Mg-Si alloy up to 500°C.

From Figure 4.7 it can also be seen that the the true flow stress of the 7021 material is strictly higher than for the 6082 material. However, the flow stress of the 7021 material decreases more steeply with increasing temperature than it does for the two 6082 materials. The flow stress of the 6082 extruded material experiences the same variation with temperature as the 6082 rolled material. It is emphasized that even though it may seem like the maximum flow stress varies linearly with temperature, the investigated temperature range is quite narrow, thus the apparent linear relationship may not continue much further. Note also that the investigated temperature ranges for the respective alloys do not overlap with more than 40°C, thus it is possible that the difference in behavior is smaller than what it would seem like if the apparent linear areas were extrapolated.

The 7021 and 6082 extruded materials have similar grain and particle structures after solution heat treatment, thus the observed differences in flow stress behavior are likely to be caused by differences in the amount and type of alloying elements in solid solution. This is also supported as both 6082 alloys have different grain and particle structures but the same alloying contents, and the steady-state flow stress of these materials vary similarly with temperatures. The alloy compositions suggest that the 7021 material will have a significantly higher concentration of alloying elements in solid solution than both of the 6082 materials. This was also inferred from the EDS results obtained during the characterization of the base material (Section 4.1.2). The higher amount of alloying elements in solid solution of the 7021 alloy translates into more obstacles to dislocation motion which in turn increases the flow stress [14]. This explains the higher flow stress of the 7021 material. The higher amount of obstacles to dislocation movement in the 7021 material material also explains the steeper decrease in maximum flow stress with increasing temperature. As the temperature increases, thermal fluctuations and diffusion diminish the restraining effect of these obstacles [14]. Because more obstacles are overcome with increasing temperature for the 7021 material than for the 6082 material, the flow stress correspondingly decreases more steeply.

This higher amount of alloying elements in solid solution in the 7021 alloy also affects the strain rate sensitivity of the material. Figure 4.7 shows that the maximum true flow stress increases with increasing strain rate for all materials, thus all materials are strain rate sensitive. However, the increase in flow stress with strain rate is larger for the 7021 material than for the 6082 materials. As the strain rate increases, more movement of dislocations is required in order to accomodate the deformation. This is more difficult in the 7021 material which contains more obstacles to dislocation movement, thus the flow stress increases more with increasing strain rate.

No variation in strain rate sensitivity with temperature was seen in the narrow temperature range investigated. The strain rate sensitivity does however seem to increase with increasing strain rate. This can be inferred from Figure 4.7. At the respective solution heat treatment temperatures of the materials, the middle point represent deformation at a strain rate of

0.02 s^{-1}, which is half of the strain rate of the upper point (0.04 s^{-1}) and ten times the strain rate of the singular, low points (0.002 s^{-1}). The difference in maximum flow stress between these points are however not proportionate to the difference in strain rate. The strain rate sensitivity thus seems to be the highest at high strain rates.

From Figure 4.7, it can also be seen that there is a stable difference in flow stress between the 6082 extruded material and the 6082 rolled material. As both materials are homogenized in the same batch and they have the same chemistry, the dispersoid structures of the materials should be fairly equal. Theory also predicts that the equilibrium sub grain size of a given alloy during steady-state hot deformation is mainly dependent on the temperature and strain rate [28], thus the sub-grain size should be similar in both materials. From the results regarding the grain structure of the materials after solution heat treatment (Section 4.3.1), it can be seen that the grains of the rolled 6082 material are larger than the grains of the extruded 6082 material after solution heat treatment. The main differences between the materials at the onset of deformation are thus the size of the Fe-based primary particles and the grain structure. The primary intermetallic particles generally have a small effect on the flow stress [54]. Grain boundaries are known to contribute to strength [17], consequently, the most likely cause of the higher flow stress in the 6082 extruded material is the finer grain structure. As earlier mentioned, the flow stress of both 6082 materials *vary* similarly with temperature, and no major differences in strain rate sensitivity are observed, thus it seems as the grain structure does not significantly affect the strain rate sensitivity or the variation in flow stress with temperature.

5.2.4 Workability

The forming limits in terms of achievable strain without fracture is as mentioned dependent on the stress state associated with the relevant forming operation. As the formability tests in the present study is carried out in uniaxial tension, the absolute values obtained here cannot be directly used as forming limits. However, the variations in formability with temperature for a forming operation with a certain stress state are similar to the variations in the formability in uniaxial tension [28], thus the results may still be useful.

As discussed in the theory section, the criterion for diffuse necking is that diffuse necking occurs when $dF = 0$ [32]. From the shape of the engineering stress–strain curves illustrated in Figure 4.6, it can thus be concluded that diffuse necking occurs shortly after the onset of plastic deformation for deformation at strain rates 0.04, 0.02 and 0.002 s^{-1}. This concurs with observations during testing, and is also expected from theory as the work hardening of the material is minimal at these high temperatures [32]. The true stress–strain curves are commonly considered invalid after the onset of necking, however the stress state within such a diffuse neck will be approximately uniaxial tension [36], thus the presented curves may still be useful beyond this point.

It can be seen from the complete set of flow curves attached in Appendix D that the total average strain at fracture varies with temperature, strain rate and material. Note that the apparent true strains at fracture as seen in the stress–strain curves represents the total elongation of the sample averaged over the sample length.

Assessment of the variations of the strain at fracture was attempted by measurement of the area contraction at fracture (%RA). The results were presented in Figure 4.8 and Figure 4.13 for strain rates 0.02 s^{-1}, 0.04 s^{-1} and 2 s^{-1}. As there are significant inaccuracies in these measurements, both due to the irregular shapes and remarkably limited sizes of the fracture surfaces, no considerable variation in reduction of area could be inferred. As the size of all fracture surfaces approached zero, thus all samples sustained extensive strain, it may also seem as the precise strain at which fracture occurs may be more coincidental than dependent on temperature or strain rate. This is also supported by the scatter in strain at fracture observed in the otherwise reproducible flow curves (Appendix D). Nevertheless, the remarkably high values of area contraction at fracture indicates very high strainability for all materials.

The maximum achievable strain in the diffuse necks was presented in figures 4.9-4.11. The onset of local necking was estimated visually and recognized by a sharp change in thickness of the sample [35], thus the accuracy of these measurements is somewhat limited. The measured

maximum strain in the diffuse necks are expected to be larger than the fracture strains observed in the true stress–strain curves, as the strain in reality is highest in the middle of the sample and lower towards the edges of the diffuse neck. However, both these strain measures vary in the same manner with temperature, strain rate and material. By comparison of the maximum measured strain in the diffuse necks and the strain at fracture in the stress–strain curves, it is deduced that the obtainable strain increases with increasing temperature for all materials. This concurs well with theory [32], and the results obtained by Fan et al. [55] who investigated the strainability of an Al-Mg-Si alloy up to 500°C. The exception is for the 6082 rolled material, where the fracture strain appears fairly stable rather than increasing at the highest temperatures.

The achievable strain before onset of local necking is consistently higher for the 7021 extruded material than for the 6082 extruded material with similar grain structure. This could amongst other be due to the higher strain rate sensitivity of the 7021 material, as theory predicts that the obtainable strain in the diffuse neck increases with increasing strain rate sensitivity [35]. In addition, imperfections and inhomogeneities in the material lower the strain at onset of local necking [36], thus another factor likely to increase the strainability of the 7021 material compared to the 6082 materials is the lower content of iron-based intermetallic phases. Strain heterogenities around particles are thought to increase with increasing particle size, and the tendency to nucleate voids would increase correspondingly. Heterogenities related to particles would thus increase with increasing particle size. The intermetallic particles in the 7021 material is smaller than in the 6082 extruded material, and this may also contribute to delay the onset of local necking. A difference in particle size could also explain the higher strains obtained in the diffuse necks of the rolled 6082 material than in the extruded 6082 material. Both materials have the same alloying content and thus similar volume fraction of intermetallic particles, but the intermetallic particles is larger in the extruded material than in the rolled material.

The maximum strain at fracture increases significantly less with temperature for the 6082 rolled material than for the 6082 extruded material. The fracture strain is however higher for

the rolled material at all temperatures. It is possible that the workability increases with increasing temperature for the extruded material because the enhanced dislocation mobility also results in a more effective accommodation of strain around particles, and thus prevents the formation of heterogeneities such as voids [32]. The stable workability of the 6082 rolled material might thus be explained as the primary particles in this material is smaller, thus higher strains are reached. At these high strains, it is possible that the obtainable strain is limited by another mechanism. As the most pronounced difference between these two materials (excluding the intermetallic particles) is the difference in grain size, this could be a strain limiting mechanism related to grain structure. One suggestion is that some grain boundary sliding promoted in the 6082 rolled material (further discussed in Section 5.2.5) possibly may create heterogeneities that can trigger local necking.

For the 7021 extruded material, it can be seen that the workability of the material is slightly but consistently lower at the higher strain rate. This could possibly be explained as the nucleation of inhomogenities at intermetallic particles may be enhanced at higher strain rates if the recovery processes are not rapid enough to effectively eliminate dislocation build up. The same effect is not seen in the 6082 materials, where no conclusive effect of strain rate on the strainability can be seen. It is likely that if such an effect exists, it would become pronounced at lower strain rates for the 7021 material than for the 6082 material, because the 7021 alloys contain more alloying elements in solid solution, and solute atoms decrease the dynamic recovery rate [54].

In summary, a high amount of alloying elements in solid solution probably results in a high strain rate sensitivity, which should be beneficial for the obtainable strain before onset of local necking. However, a higher amount of alloying elements would also result in an enhanced dislocation density, which could lower the workability, possibly in interaction with primary particles and high strain rates. Further work should be conducted in order to determine these potential effects. At a given volume fraction of intermetallic particles, smaller particles seems to give the highest workability.

The matematical criterion for local necking is repeated in Equation 5.1 [35].

$$\frac{d\sigma}{d\varepsilon} = \frac{\sigma}{2} \tag{5.1}$$

This criterion suggests that local necking of the samples deformed by hot tensile testing would experience local necking before reaching the steady-state region (where $\frac{d\sigma}{d\varepsilon} \approx 0$) is reached. This does not concur with visual observations made during the tests, or with the fact that all samples could be elongated at least 50% (corresponding to a true strain of 0.41) without local necking in the experiments regarding microstructure development. A criterion for local necking that fits the observations better would be that necking occurs when the $\frac{ds}{de}$ drops from the constant value obtained during steady-state, where s is the engineering stress and e is the engineering strain. This statement is however solely based on real-time visual observation of the sample and the measured stress, and is thus highly speculative.

For the samples deformed with the Gleeble system at the high strain rate of 2 s^{-1}, the deformation is as earlier mentioned nonuniform at all strains due to the temperature gradient in the samples. Consequently the onset of local necking could not be obtained from these tests. The only obtainable measure of strainability at this high strain rate is thus the % reduction of area at fracture, which as discussed indicated high strainability at the relevant conditions.

5.2.5 Fracture

For the strain rates of 0.02 s^{-1}, 0.04 s^{-1} and 2 s^{-1}, the dominating fracture mechanism seems to be transgranular creep fracture as the fracture surfaces are dimpled and look typically ductile. However, as the cross sectional area contraction at fracture is close to 100%, the fractures may also be characterized as rupture fractures where either nucleation of internal cavities and/or growth of nucleated cavities is suppressed so that the onset of fracture is delayed[14, 32]. Rapid dynamic recovery, which is observed at these conditions, may be responsible for both these effects, and is typically associated with rupture [14, 32].

One sample of each material was deformed with the low strain rate of 0.002 s^{-1} at 540°C. At this low strain rate, a shift in fracture mechanism was observed in both 6082 materials, and no local necking was observed. The fractography revealed a macroscopically ductile fracture surface, but some distinct observations were made at higher magnifications. In the fracture surface of the 6082 rolled material, some seemingly brittle facets and apparent grain nodes were observed. It is thus possible that an increasing amount of grain boundary sliding occurs at this low strain rate, and that the observed facets and grain nodes thus originates from cracks nucleated on the grain boundaries. This sample experienced a uniquely low fracture strain (see Appendix D, Figure D.7). Investigations of the fracture surface of the 6082 extruded material at higher magnifications revealed a structure consisting of small, more rounded bumps. It is thought that a lack of grain boundaries normal to the deformation direction could suppresses substantial intergranular crack growth. This thought is supported by the significantly larger strain at fracture for this sample than for the sample of rolled 6082. If crack formation at the grain boundaries is suppressed, crack growth at the subgrain boundaries may possibly be triggered. These boundaries are less defined than the main grain boundaries, thus this could explain the somewhat unusual appearance of the fracture surface. The size of the observed bumps also corresponds better with a typical subgrain size than with the grain size. In summary, it is possible that the fracture mechanism partly shifts towards transgranular creep fracture at the lowest strain rate for the 6082 material. Theory predicts that grain boundary sliding, and thus transgranular creep fracture is promoted at lower strain rates and high temperatures [14, 32].

Similar signs of sliding at grain boundaries or sub boundaries are not observed in the 7021 extruded material, even though the flow stress inside the grains is larger in this material. A possible explanation for this could be the $ZrAl_3$-dispersoids which are present in the 7021 material and not in the 6082 material. These dispersoids are coherent with the matrix [50], and they are typically present with a higher number density than the Mn- and Cr-based dispersoids in the 6082 material [56], thus they could be more effective in restraining sliding on sub boundaries.

5.3 Grain structure evolution

As the grain structure of a material may have significant effects on the mechanical properties, experiments were conducted in order to assess the effect of deformation at the relevant conditions on the grain structure of the selected materials.

During heating without deformation, no recrystallization was observed between 400°C and 500°C in either the AA7021.50 rolled or extruded materials. This is expected as the 7xxx alloy system typically contains a high density of $ZrAl_3$-dispersoids, which is the most effective commercial dispersoid for prevention of recrystallization [50]. The 6082 material with Mn- and Cr-based dispersoids is not as resistant to recrystallization [56], however, the bulk of the AA6082.25 extruded material did not recrystallize at any temperatures between 460°C and 560°C. Recrystallization was however observed in the surface layer at 560°C. Because the driving force for recrystallization is the enhanced dislocation density induced in the material during deformation [29], this is probably due to the larger deformations typically induced in the surface layer during extrusion [6]. The AA6082.25 rolled material did recrystallize at all investigated temperatures. This can be explained as the rolled material is subjected to cold deformation, which may provide sufficient dislocation density to induce recrystallization. The deformation structure of the material was however still visible after heat treatment as the recrystallized grains were not fully equiaxed. This is probably because the dispersoids limit the mobility of the grain boundaries [27], even though recrystallization could not be prevented.

The recrystallized texture of the 6082 rolled material was practically random. This also supports the assumption that anisotropy not will induce significant issues during forming.

No dynamic recrystallization was observed in any of the materials during hot deformation (Figures 4.26 - 4.28). This observation is supported by the shape of the corresponding flow curves, as theory states that dynamic recrystallization of the microstructure during deformation would cause a sudden decline in true flow stress [28], which was not observed for any materials. This concurs well with theory, which states that dynamic recrystallization is

uncommon in aluminium [28], as the dynamic recovery rates typically are rapid [27] thus the dislocation density required to drive recrystallization is never is obtained. It should however be taken into consideration that the surface layer of the extruded profiles was machined off in order to make tensile samples with the same thickness as the rolled material. Consequently, no results were obtained regarding recrystallization in the surface layer which as earlier mentioned is more severely deformed than the bulk of the material. For the 6082 extruded material, where recrystallization of the surface layer was observed at 560°C, it is not unlikely that the additional generation of dislocations induced in the beginning of the deformation may induce recrystallization in the surface layer also at 540°C. This would be unfavorable, as larger grains in the surface are known to give poor surface appearance [57].

Some grain growth of the previously recrystallized grains was observed after deformation of the 6082 rolled material, especially at the lowest strain rate (0.002 s^{-1}). However, the observed grain growth is not extensive enough to have a major effect on the mechanical properties of the material. These grains also seem to further elongate in the deformation direction during hot tensile deformation. This concurs well with theory, which states that grains develop in the same manner during hot deformation as during cold deformation [28].

Similar grain growth was not observed in the extruded materials, probably because they had not recrystallized at the onset of deformation. For the 7021 extruded material, no conclusive effect of deformation with a strain rate of 0.02 s^{-1} could be seen on the grain structure. However, after deformation at the lowest strain rate of 0.002 s^{-1}, the previously smoother grains appear more uneven with rough grain boundaries. Some grains also seem broken up and distributed in pieces along the deformation axis. The same kind of rough grain boundaries and broken up structure is observed for all the samples of the 6082 extruded material, even though these features are far most pronounced in the material deformed at the lowest strain rate (0.002 s^{-1}). The apparent rough boundaries and some of the small, separate grain pieces could be indications of slightly initiating recrystallization.

No abnormal grain growth was observed in any samples or materials, thus it is unlikely that abnormal grain growth will impose significant challenges during processing of the selected materials by press form hardening.

5.4 Precipitation potential

A deformed material is commonly observed to have a lower incerase in hardness during artificial age hardening than an undeformed material [56]. Experiments were thus conducted in order to assess the effect of high temperature deformation on the hardening response during subsequent age hardening.

As seen from the artificial age hardening curves of the undeformed samples presented in Figure 4.29, it can be seen that the hardness of the 6082 extruded material is consistently higher than the hardness of the 6082 rolled material, though the hardness of both materials develops similarly with time. This difference in hardness could possibly be explained by a denser sub grain or dislocation cell structure arising in the extruded material after extrusion [56]. This structure could be partially preserved through solution heat treatment, and give a slightly higher hardness in the material.

For the samples that were deformed with the Gleeble system prior to artificial age hardening, the samples deformed at the lowest temperatures experienced a less favorable quenching than the samples deformed at the solution heat treatment temperature (see Figure 4.30). However, no significant differences between the samples that went through the these temperature cycles without any deformation was observed (figures 4.31 and 4.33).

Several factors influence the hardness of the samples after deformation and artificial age hardening. Theory predicts that higher strain rates and lower temperatures during hot deformation would promote a smaller dynamic subgrain size in the material [28], which in itself would strengthen the material corresponding to grain boundary strengthening. As the strain in the center of the samples was largest for the samples deformed at the lowest temperatures (seen from Figure 4.34), it is also likely that the actual strain rate in the deformed

material volume was higher for these samples. This would make the sub structure even more dense, which thus would give an even higher hardness in the samples deformed at the lowest temperatures. It is also possible that the material deformed at the highest temperatures have a lower overall dislocation density, as the dynamic recovery rates increase with increasing temperature. A lower dislocation density would give a lower hardness in the material.

However, the dislocation structure of the material also influences the precipitate structure subsequent to artificial age hardening. Precipitation of strengthening particles is promoted on dislocations [58], thus the precipitate structure may become somewhat inhomogeneous if there is a very distinct dislocation structure present. This would be unfavorable for the strength of the material. Furthermore, precipitates may nucleate heterogeneously at dislocations, and this would cause the material to reach peak hardness faster expected from artificial ageing curves that are made based on an undeformed material. The heterogeneously nucleated precipitates are however typically coarser and less favorable for strengthening than the precipitates that nucleates homogeneously in the matrix [59].

The standard deviation of the hardness measurements subsequent to hot deformation and artificial age hardening (presented in Figure 4.32) are large compared to the apparent effects, thus it is difficult to conclude on which of the possible effects of deformation at high temperature that are the most pronounced in these experiments. Similar considerations applies to the electrical conductivity measurements (Figure 4.33). A homogeneous and finely divided dislocation and particle structure would lower the electrical conductivity of the material compared to a heterogeneous structure or coarser structure. A lower overall dislocation density would increase the electrical conductivity.

The most important result from the experiments regarding the precipitation following hot deformation is that the hardness of the 6082 rolled material after artificial age hardening is not detrimentally lowered by quite extensive deformation at temperatures in the range of 440°C to 540°C and strain rates in the range of 0.2 s^{-1} to 2 s^{-1}.

5.5 Implications for the suitability for PFH

5.5.1 Formability

The flow stress of all the tested materials is very low at the relevant forming temperatures. This is favorable for forming as the forces acting on the forming tools and the corresponding energy consumption would be low. Even though the 7021 alloy generally have higher strength than the 6082 alloy at room temperature [60], the flow stress of these alloys becomes close to equal for at the highest temperatures.

The workability of all materials was high at the relevant forming temperatures. This is favorable for forming as it becomes possible to form geometries that require more severe strains. Diffuse necking was observed to occur rapidly for all materials at all relevant forming temperatures. Diffuse necking is normally not limiting in a sheet forming process, as the relatively uniform thinning of the material does not introduce any major structural weaknesses in the finished part. It is however important to consider diffuse necking, as it may act as a global instability because the diffuse neck may become unable to transmit the force required to obtain certain forming geometries [36].

The onset of diffuse necking in a tensile strip is a global instability dependent on geometry [36], thus the onset of local necking is a better measure for assessment of the workability as a material property. Local necking can be analyzed without involving the overall deformation process [36]. All materials could withstand large strains at the relevant forming temperatures, and the formability was highest *at* the respective solution heat treatment temperatures.

The 7021 extruded material had the highest workability of the investigated materials. The 6082 extruded material had the lowest workability, though the true strain at onset of necking was above 1.2 at all relevant forming temperatures.

The results also indicated that a low strain rate (0.002 s^{-1}) could be detrimental to the workability of both the 6082 materials, especially to the 6082 rolled material, as cracks could

develop at grain boundaries. This does not challenge the capability of the press form hardening process, as this process typically is associated with rapid forming at high strain rates. It is however useful to be aware of this, in case regions of low strain rate should emerge in the design of a specific component. Similar challenges was not observed in the 7021 material at the investigated conditions.

No major effects of strain rate was observed for the intermediate strain rates 0.02 s^{-1} and 0.04 s^{-1}. At the highest strain rate of 2 s^{-1}, work hardening was observed in the 6082 rolled material. The effect of work hardening on the strainability of the material was not directly assessed, however some further evaluation can be made. Mielnik [35] predicts a synergistic effect of combined strain hardening and strain rate hardening, giving significantly higher obtainable strain than the sum of what these two effects can provide alone. As a notable strain rate sensitivity is observed at these temperatures, this indicates that deformation with high strain rate, giving strain hardening, could be beneficial regarding the workability of the material. However, results from hot deformation of the 7021 material suggests that high strain rates also could lower the strain at onset of local necking, possibly due to combining effects of high dislocation density and primary particles present in the material. Consequently, more thorough investigations regarding the effect of strain rate in these materials are required.

Both the flow stress and workability of all materials was most favorable at the respective solution heat treatment temperature. There is thus no reason to cool the material from the solution heat treatment temperatures prior to forming. These properties became less advantageous at lower temperatures, though they were excellent at all relevant forming temperatures.

As there typically are great challenges related to forming of alloys in the 7xxx series due to their high strength, it seems like it would be particularly favorable to develop the press form hardening process for the 7021 material and similar alloys. The 7021 alloy both had superior strainability and remarkably low flow stress at the relevant conditions, which are properties that are highly advantageous for forming.

5.5.2 Properties of the finished part

Because a smaller grain size generally is favorable in the finished parts, materials that do not recrystallize during solution heat treatment or forming would be most suitable for press form hardening. It might also be favorable to avoid dynamic recrystallization, as the dynamically recovered structure is regarded as considerably stronger [28]. Neither of the assessed extruded materials recrystallized prior to or during hot deformation, thus a fine grain structure was obtained after deformation of these materials. The rolled 6082 material recrystallized during solution heat treatment, but not during the subsequent deformation. This indicates that extruded materials may be most suitable for forming by press form hardening when the grain structure of the finished part is considered. Extrusion of the base materials also have the additional advantage that the cross section of the profiles prior to forming can be varied, which provides higher flexibility in component design. However, recrystallization in the surface layers was not investigated in this work. Further work is required to assess this, as recrystallization in the surface layer could be detrimental to the properties of the component.

The 7021 alloy in general showed the highest resistance to recrystallization and thus seems further suitable for forming by press form hardening.

The effect of deformation at high temperatures on the subsequent artificial age hardening was investigated for the 6082 rolled material. No significant adverse effect on the hardness was observed, which is beneficial for the mechanical properties after forming. Further work is however required in order to determine the related mechanisms for all potential base materials.

6 Conclusion

Aluminium alloys 6082.25 and 7021.50 were evaluated and compared as potential base materials for processing by press form hardening. Both extruded profiles and rolled sheets were assessed, however the rolled 7021 material was neglected early in the project due to time constraints. The conclusions of the work are summarized as follows:

- The flow stress and workability of all investigated materials is highly favorable for forming at all forming temperatures relevant to press form hardening. These properties are *most* favorable at the solution heat treatment temperatures of the respective alloys.
- When the grain structure of the finished part is considered, the use of a material that does not recrystallize during solution heat treatment seems advantageous. The extruded materials in this work did not recrystallize in bulk neither during solution heat treatment nor hot deformation, however recrystallization in the surface layer was not assessed. No disfavour of the fibrous grain structure associated with extruded materials was observed regarding formability at the relevant temperatures.
- The AA7021.50 extruded material seems especially suitable for press form hardening due to a particularly high workability and low flow stress at the relevant forming conditions. The superior resistance to recrystallization in this material may further favor it as a suitable base material for press form hardening.
- The size and distribution of Fe based primary phases appear to influence the workability of the base materials. This should be investigated more closely.
- There are indications that both too high or too low strain rates may have negative effects on the workability of the materials in the relevant temperature range. The effect of strain rate on the workability of the materials should thus be further assessed.
- No detrimental effect of the hot deformation on the artificial ageing response was observed in the AA6082.25 rolled material. This should however be further and more thoroughly assessed for all potential base materials.

7 Recommendations for Further Work

Further work is required in order to assess each of the discussed topics in detail. Further work should include:

- Assessment of the effect of stress state on the workability at relevant conditions. In the present study the workability was only assessed in uniaxial tension.
- Further formability testing with a temperature cycle that simulates the conditions in press form hardening; that is simultaneous forming and cooling.
- Closer investigations of the correlation between workability and the amount, size and distribution of Fe based primary particles at the relevant conditions.
- Further assessment of the effect of strain rate on the workability of the materials at these high temperatures. The connections between workability at high strain rates and alloying content and primary particle structure should be determined.
- Further investigations of recrystallization in the surface layer of extruded profiles during hot deformation.
- Thorough evaluations of the effect of hot deformation on the precipitation of hardening precipitates during the subsequent artificial age hardening of all potential base materials.

A Geometry of Tensile Samples

Geometry of tensile samples for hot tensile testing

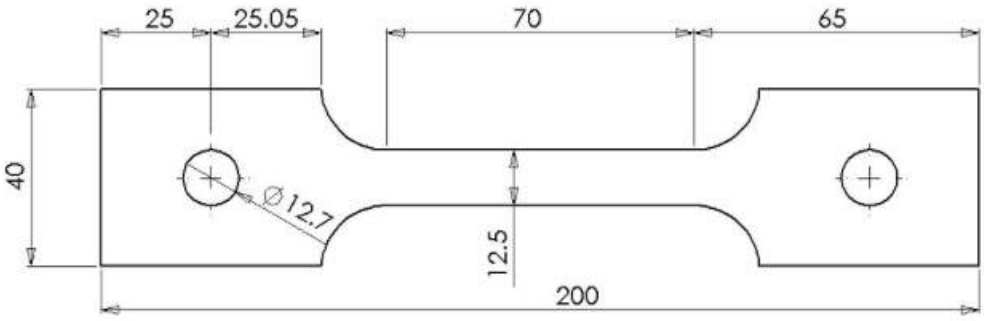

Figure A.1: Sample geometry for hot tensile testing. The thickness of all samples was 4.8mm.

Geometry of samples for Gleeble tensile testing

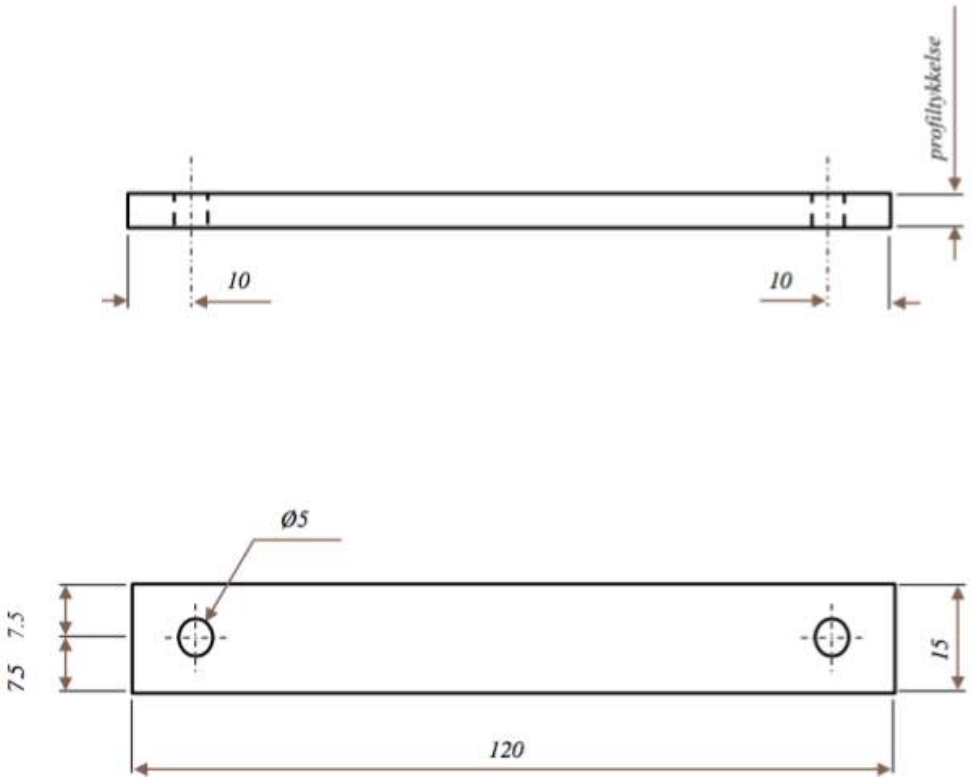

Figure A.2: Sample geometry for Gleeble tensile testing. The profile thickness was 4.8mm

B Test Matrixes for Formability Tests

B.1 Test matrix for the hot tensile testing

Table B.1: Complete test matrix for the AA6082.25 material.

AA6082.25		
Temperature [°C]	**Strain rate [1/s]**	**Parallels [ ]**
560	0.04	2
540	0.04	3
490	0.04	3
440	0.04	3
560	0.02	2
540	0.02	3
490	0.02	3
440	0.02	3
540	0.002	1

Table B.2: Complete test matrix for the AA7021.50 material.

AA7021.50		
Temperature [°C]	**Strain rate [1/s]**	**Parallels [ ]**
480	0.04	3
430	0.04	3
380	0.04	3
480	0.02	3
430	0.02	3
380	0.02	3
480	0.002	1

B.2 Test matrix for the Gleeble testing

Table B.3: Complete test matrix for the Gleeble testing of the AA6082.25 material.

AA6082.25		
Temperature [°C]	**Strain rate [1/s]**	**Parallels [ ]**
540	2	2
490	2	2
440	2	2

C EDS Results

Figures C.1 and C.2 displays the scanned particles and areas in the AA6082.25 extruded sample. Table C.1 presents the corresponding results in normalized wt%.

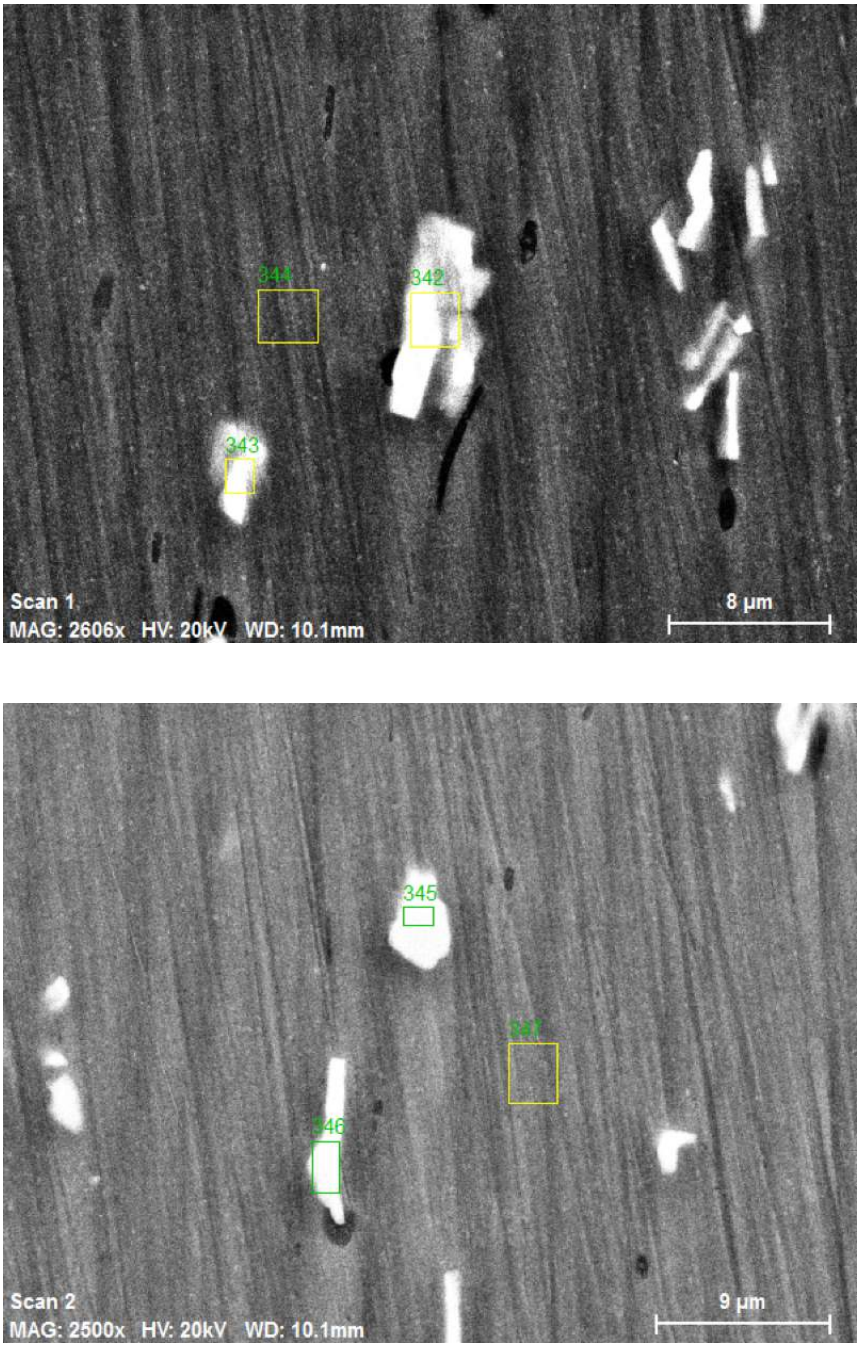

Figure C.1: Scanned areas of the AA6082.25 extruded sample.

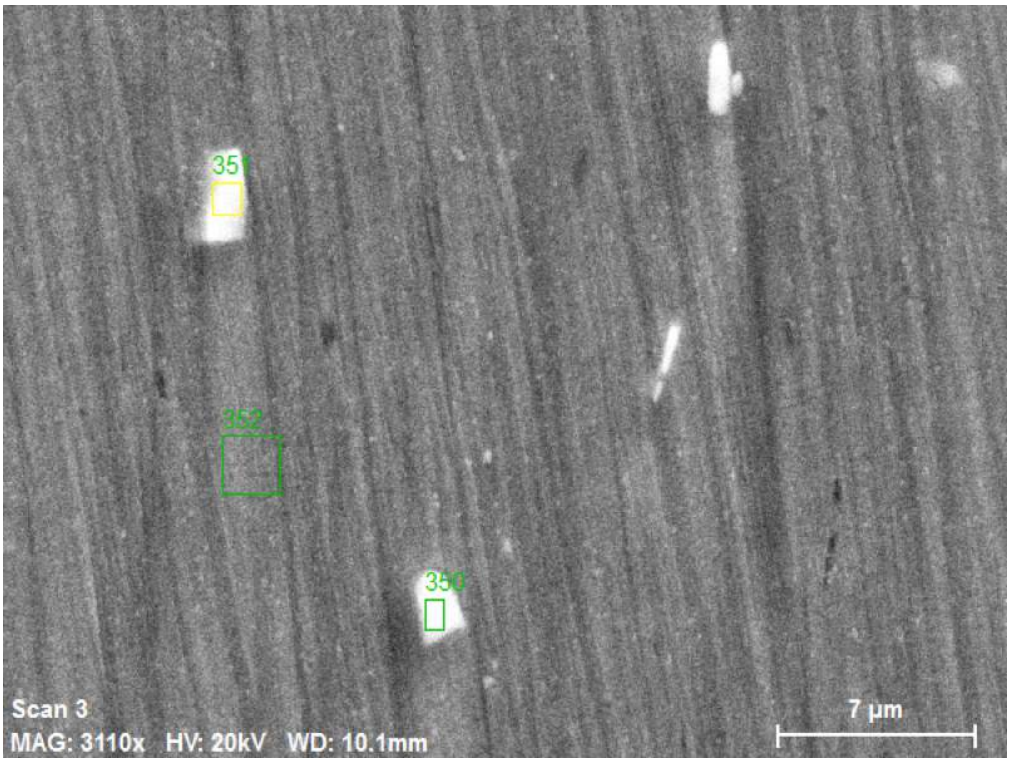

Figure C.2: Scanned areas of the AA6082.25 extruded sample.

Table C.1: Normalized EDS results for each scanned area of the AA6082.25 extruded sample in wt%.

	342	**343**	**344**	**345**	**346**	**347**	**350**	**351**	**352**
Al	69.99	73.99	97.68	69.46	79.68	97.44	83.76	81.77	97.67
Si	6.51	5.13	0.66	6.97	5.14	0.75	4.34	5.00	0.67
Fe	11.40	10.23	0.01	11.60	6.99	0.00	5.76	6.59	0.00
Mn	9.16	7.97	0.31	9.38	5.71	0.18	4.30	4.34	0.29
Mg	1.37	1.09	1.30	0.99	1.63	1.61	1.22	1.51	1.34
Cr	1.31	1.36	0.02	1.32	0.76	0.01	0.54	0.79	0.03
Cu	0.22	0.21	0.02	0.24	0.09	0.00	0.07	0.00	0.00
Zn	0.05	0.03	0.00	0.03	0.00	0.01	0.00	0.00	0.00

Figure C.3 displays the scanned particles and areas in the AA6082.25 rolled sample. Table C.2 presents the corresponding results in normalized wt%.

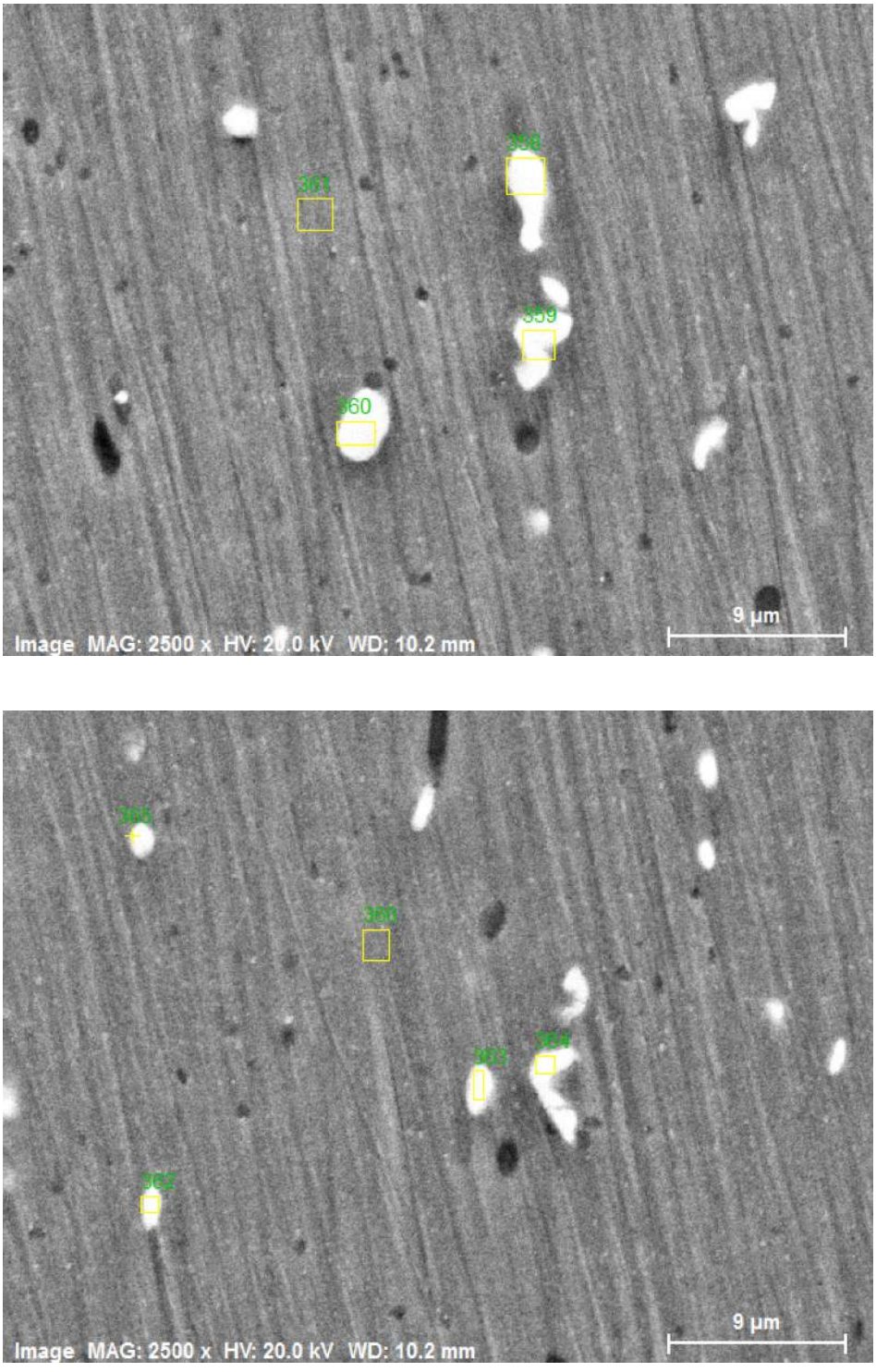

Figure C.3: Scanned areas of the 6082 rolled sample.

Table C.2: Normalized EDS results for each scanned area of the AA6082.25 rolled sample in wt%.

	358	359	360	361	362	363	364	365	366
Al	77.50	73.58	73.79	97.79	85.81	82.38	76.89	86.78	97.51
Si	6.04	5.88	6.63	0.69	4.43	5.08	5.42	4.07	0.47
Fe	5.48	9.15	4.79	0.00	3.26	2.98	7.13	2.52	0.16
Mn	7.77	8.81	10.67	0.25	4.57	7.12	8.17	4.64	0.56
Mg	1.53	0.97	1.58	1.13	1.28	1.18	1.14	1.27	1.18
Cr	1.59	1.36	2.45	0.01	0.62	1.22	1.13	0.70	0.12
Cu	0.09	0.23	0.09	0.00	0.02	0.04	0.12	0.02	0.10
Zn	0.00	0.02	0.00	0.01	0.00	0.00	0.00	0.00	0.00

Figures C.4 and C.5 displays the scanned particles and areas in the AA7021.50 extruded sample. Table C.3 presents the corresponding results in normalized wt%.

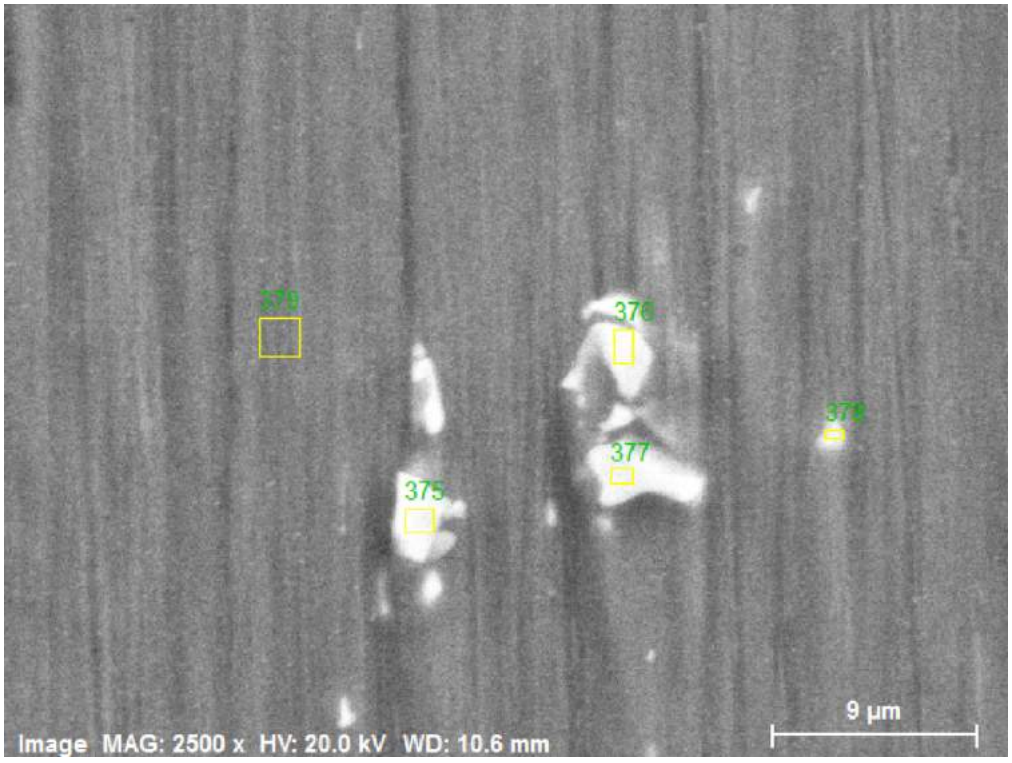

Figure C.4: Scanned areas of the AA7021.50 extruded sample.

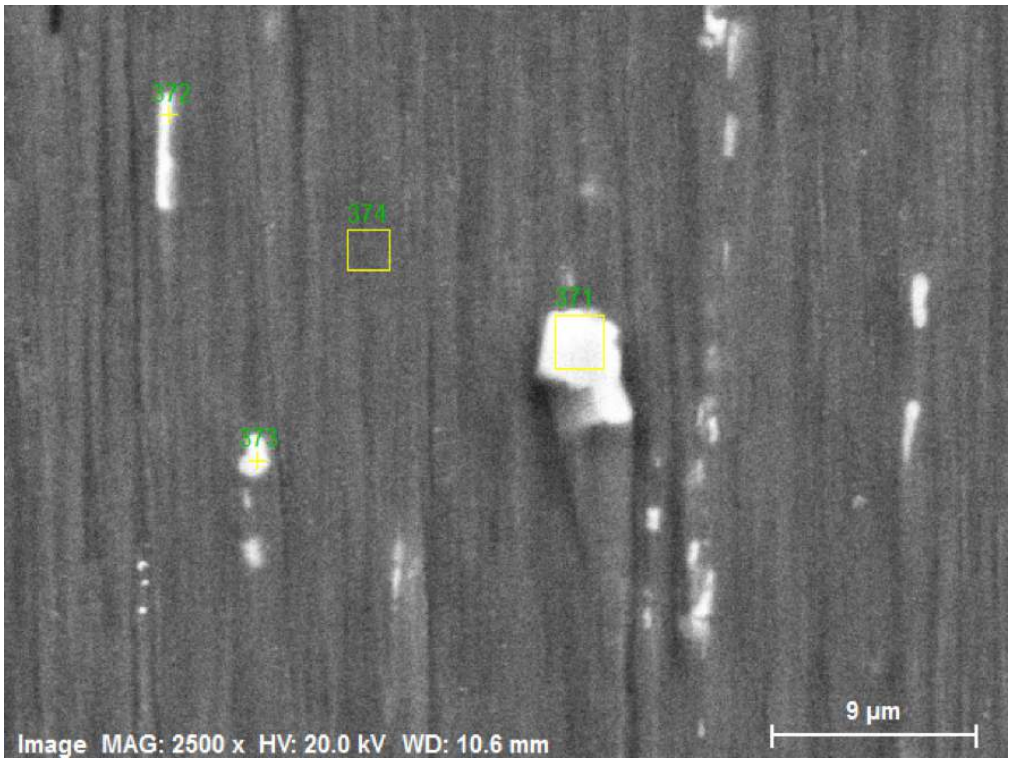

Figure C.5: Scanned areas of the AA7021.50 extruded sample.

Table C.3: Normalized EDS results for each scanned area of the AA7021.50 extruded sample in wt%.

	371	**372**	**373**	**374**	**376**	**377**	**378**	**379**
Al	66.56	8.83	78.05	90.44	73.92	67.97	85.29	90.64
Fe	24.26	12.05	12.80	0.03	16.86	23.17	5.47	0.02
Si	2.46	1.29	0.58	0.19	2.15	2.24	0.45	0.23
Mg	1.28	2.16	2.24	2.58	1.67	1.32	2.47	2.55
Zn	2.39	3.85	3.78	5.97	3.19	2.65	4.62	5.81
Cu	2.35	1.22	1.86	0.30	1.50	2.08	0.89	0.25
Zr	0.56	0.54	0.68	0.47	0.66	0.45	0.77	0.50
Mn	0.14	0.07	0.01	0.01	0.04	0.12	0.03	0.00

Figure C.6 displays the scanned particles and areas in the AA7021.50 rolled sample. Table C.4 presents the corresponding results in normalized wt%.

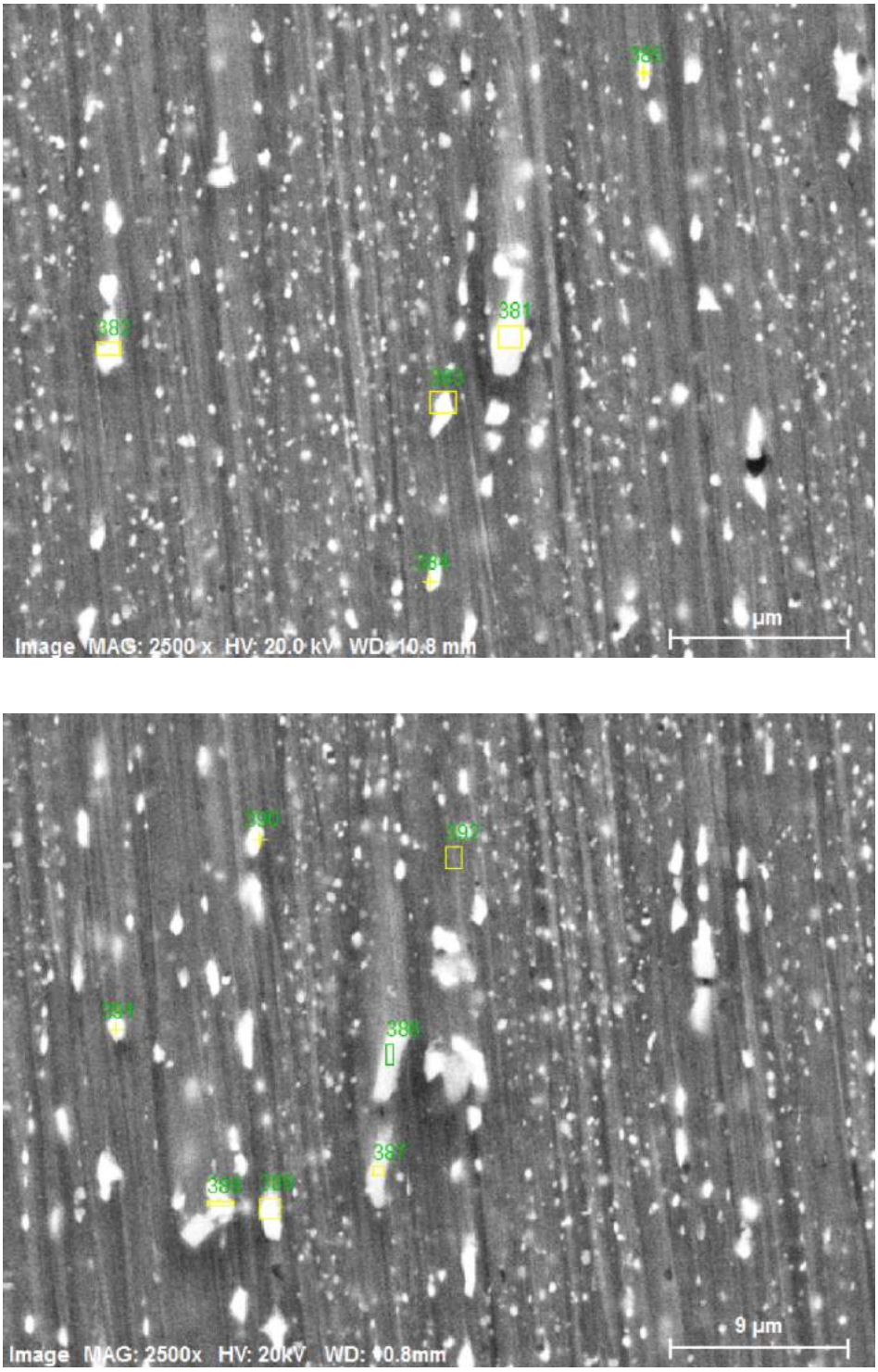

Figure C.6: Scanned areas of the AA7021.50 rolled sample.

Table C.4: Normalized EDS results for each scanned area of the AA7021.50 rolled sample in wt%.

	381	**382**	**383**	**384**	**385**	**386**	**387**	**388**	**389**	**390**	**391**	**392**	**397**
Al	70.06	73.18	80.97	71.88	70.79	77.77	78.20	69.07	76.98	86.10	66.44	93.77	93.00
Fe	20.09	1.96	0.02	0.02	0.01	17.81	16.11	5.62	0.13	0.02	0.02	0.02	0.23
Si	1.85	0.55	0.27	0.35	0.30	0.26	0.54	1.22	0.29	0.17	0.84	0.18	0.21
Mg	1.62	4.82	3.88	5.70	5.27	1.70	2.28	5.81	4.24	2.65	7.85	1.90	1.94
Zn	3.72	17.71	13.48	20.18	21.67	1.66	2.09	16.31	6.64	10.08	22.78	3.58	3.90
Cu	2.10	1.15	0.73	1.07	1.14	0.17	0.20	1.43	1.00	0.54	1.29	0.09	0.21
Zr	0.51	0.62	0.65	0.81	0.81	0.53	0.53	0.54	0.69	0.45	0.76	0.44	0.50
Mn	0.07	0.02	0.00	0.00	0.00	0.10	0.06	0.01	0.03	0.00	0.01	0.03	0.01

D True stress–strain curves

D.1 Hot tensile testing

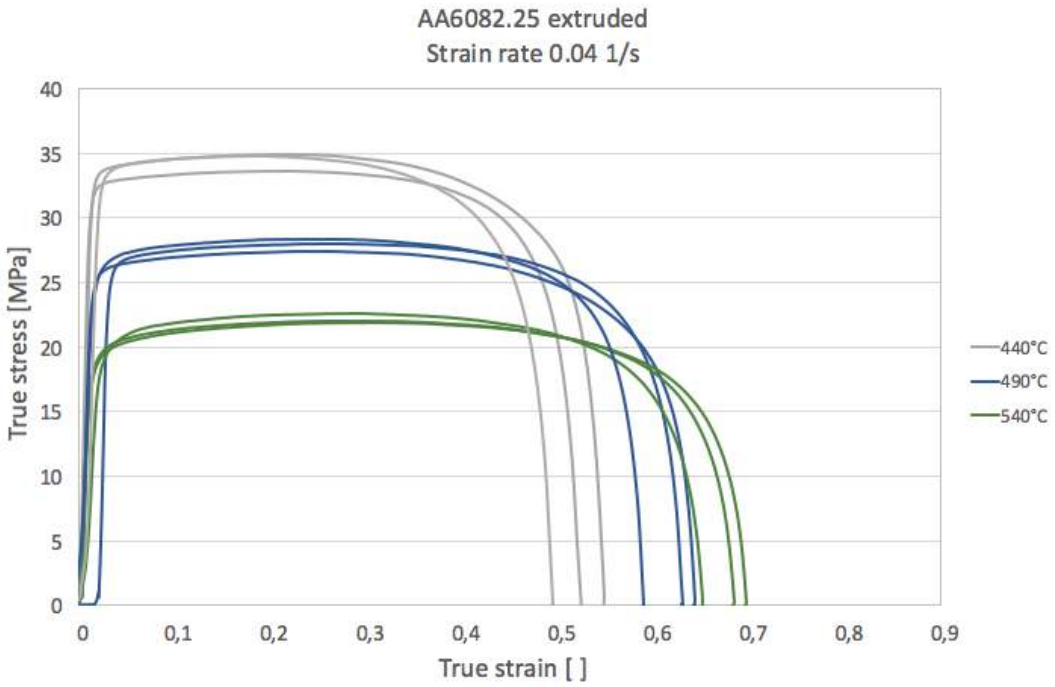

Figure D.1

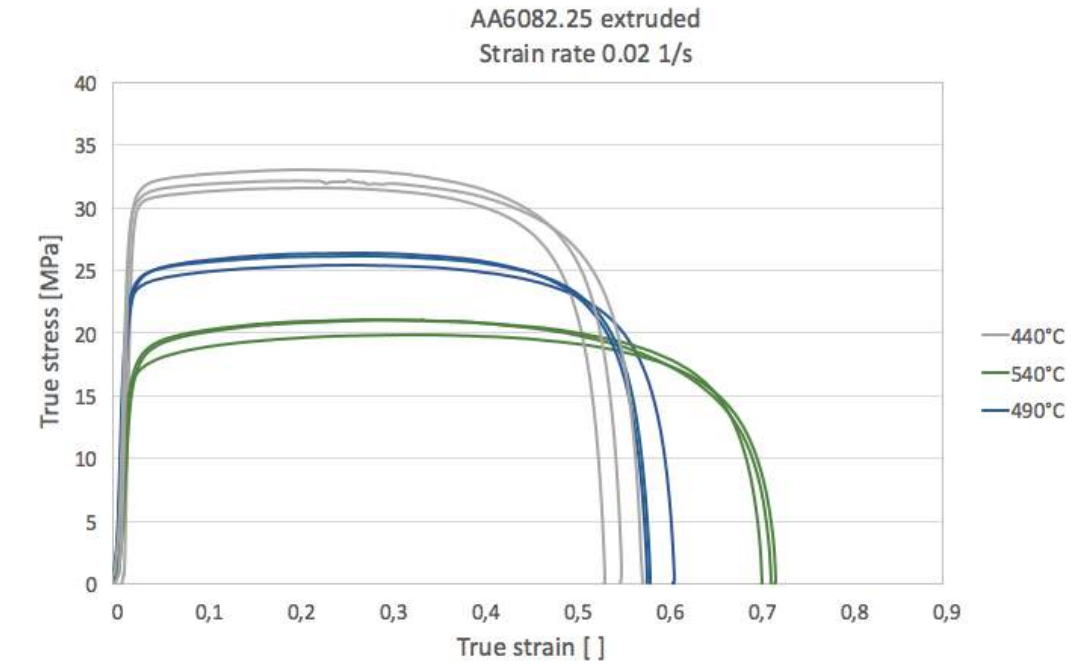

Figure D.2

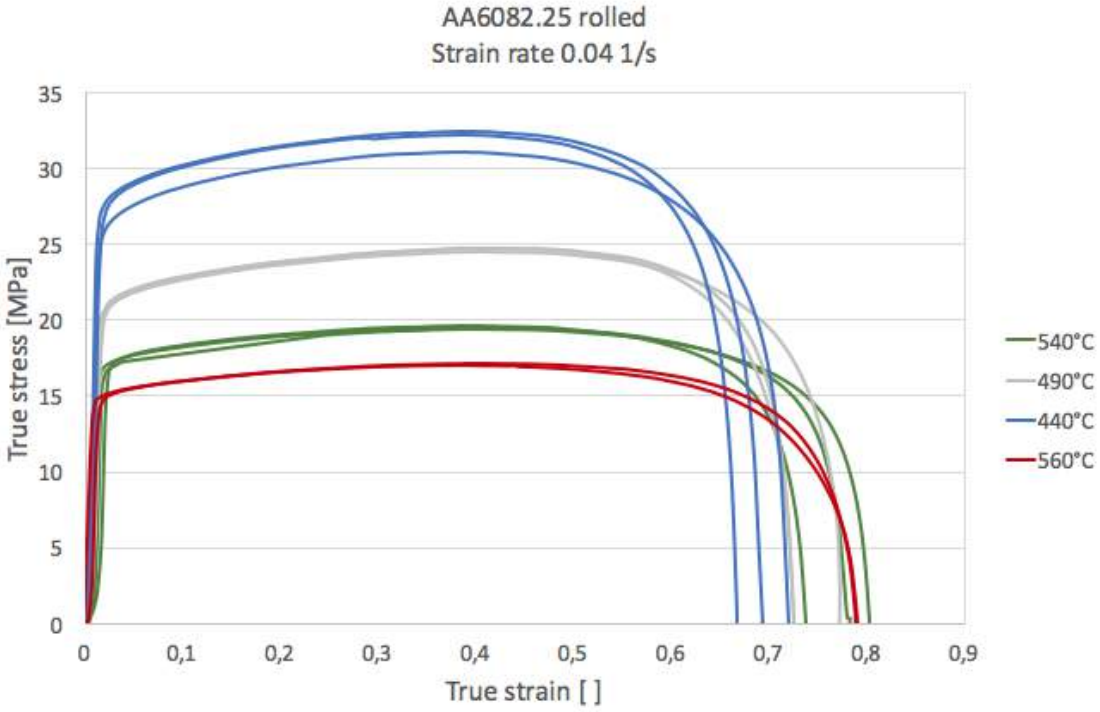

Figure D.3

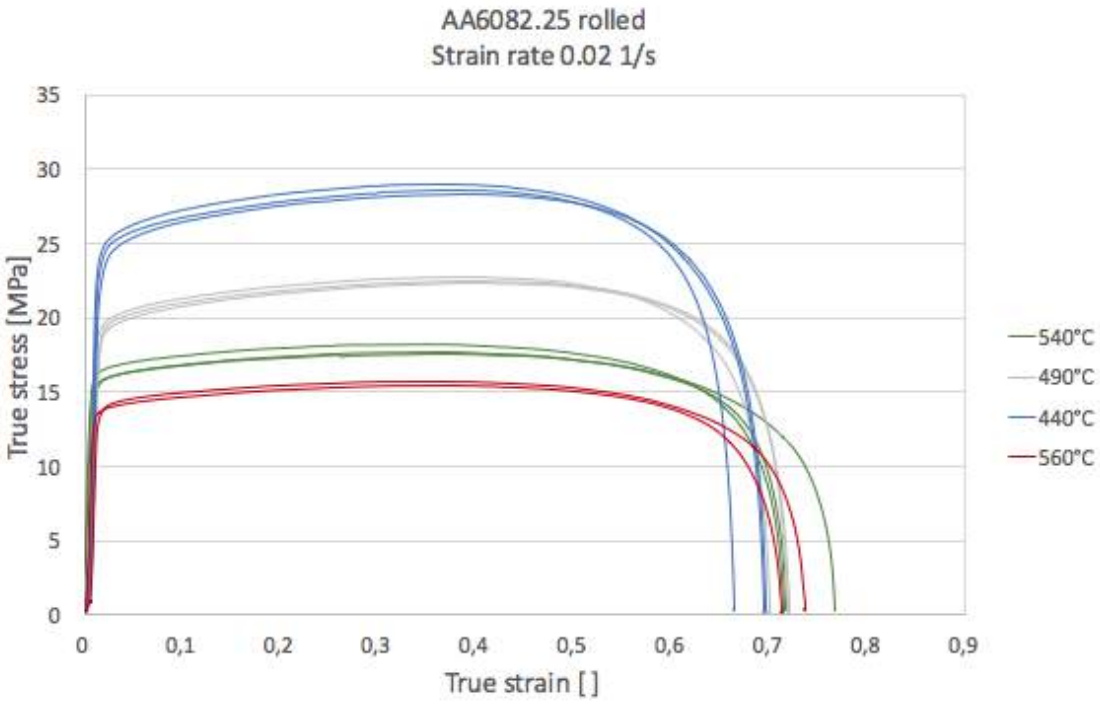

Figure D.4

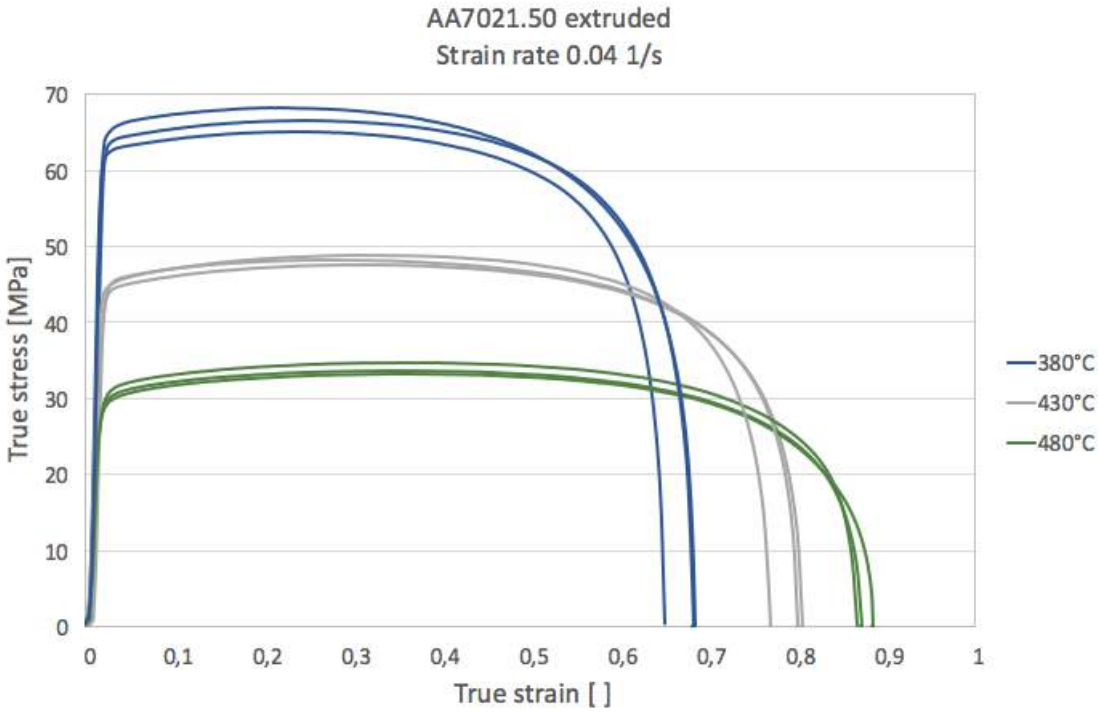

Figure D.5

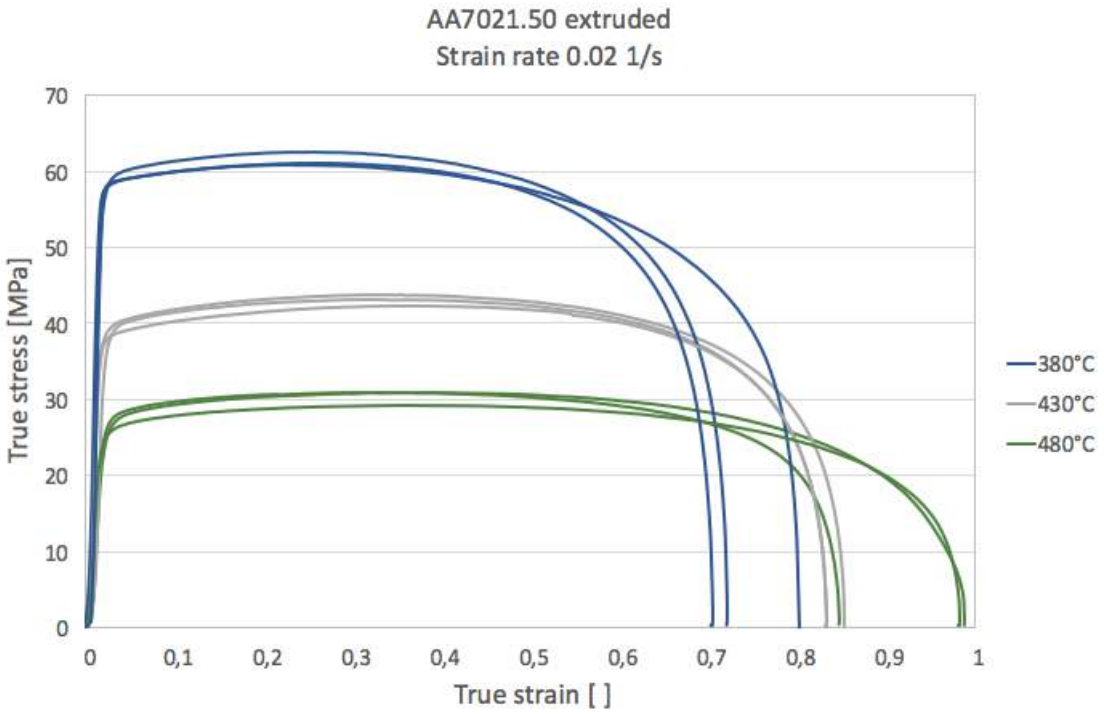

Figure D.6

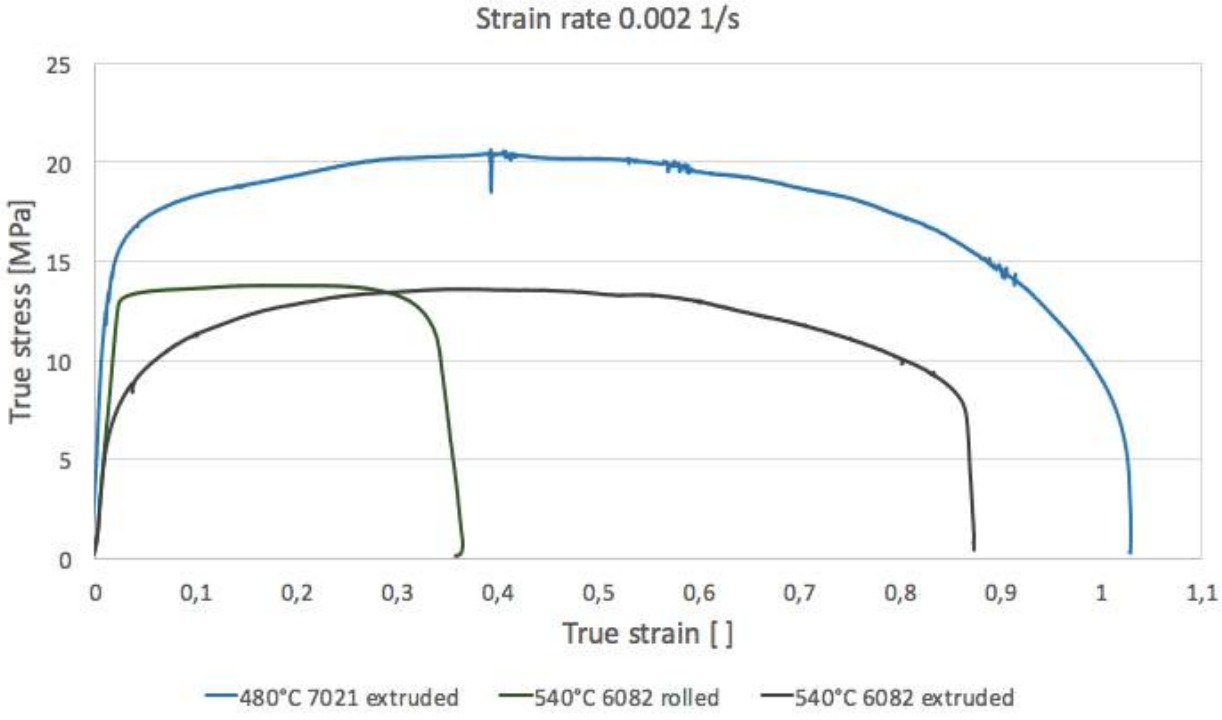

Figure D.7

E Areas scanned during EBSD

E.0.1 The base material

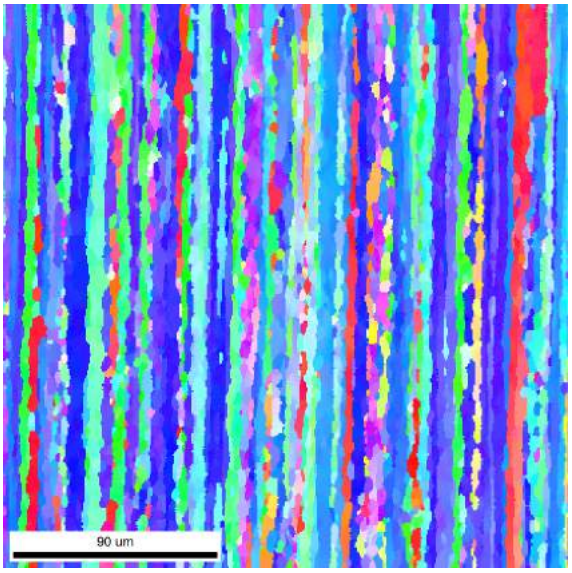

(a) AA6082.25 extruded.

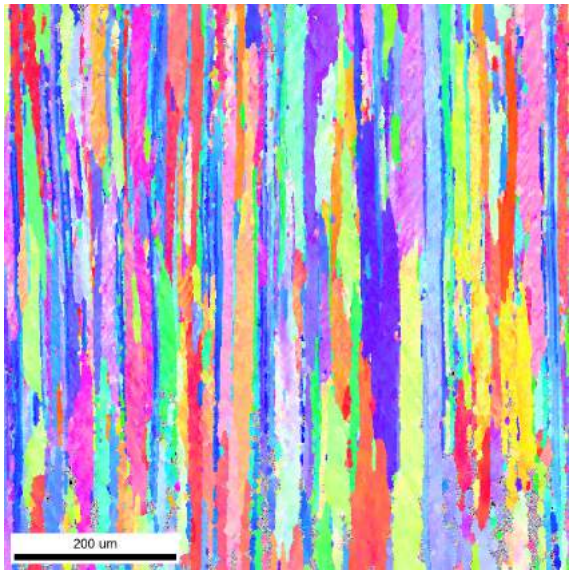

(b) AA6082.25 rolled.

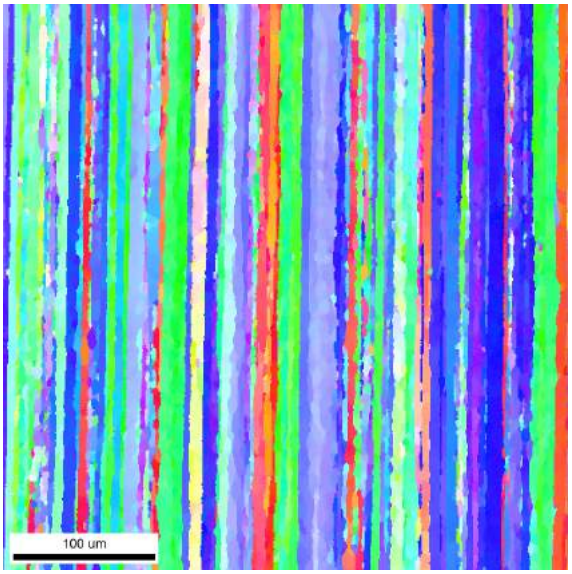

(c) AA7021.50 extruded.

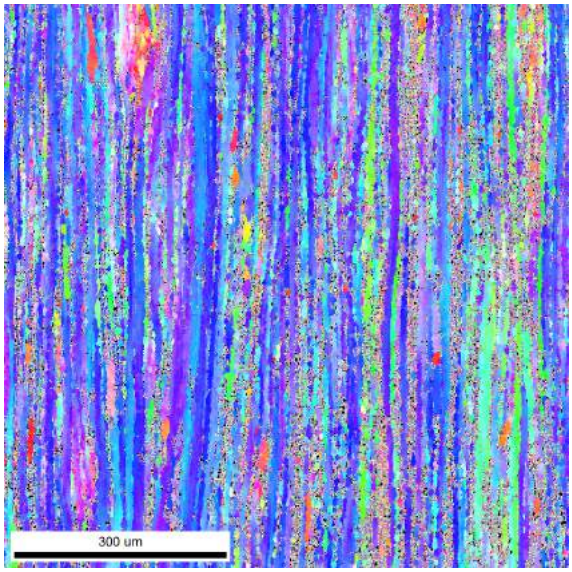

(d) AA7021.50 rolled.

Figure E.1: Scanned areas of the base materials.

E.0.2 Recrystallized material

Figure E.2: Scanned area of the recrystallized AA6082.25 rolled material.

References

[1] W. S Miller, L. Zhuang, J. Bottema, A. J. Wittebrood, P. De Smet, A. Haszler, and A. Vieregge. Recent development in aluminium alloys for the automotive industry. *Materials Science and Engineering*, A280:37–49, 2000.

[2] J. Jeswiet, M. Geiger, U. Engel, M. Kleiner, M. Schikorra, J. Duflou, R. Neugebauer, P. Bariani, and S. Bruschi. Metal forming progress since 2000. *CIRP Journal of Manufacturing Science and Technology*, 1:2–17, 2008.

[3] A. Mayyas, A. Qattavi, M. Omar, and D. Shan. Design for sustainability in automotive industry: A comprehensive review. *Renewable and Sustainable Energy Reviews*, 16:1845–1862, 2012.

[4] I. N. Fridlyander, V. G. Sister, O. E. Grushko, V. V. Berstenev, L. M. Sheveleva, and L. A. Ivanova. Aluminium alloys: Promising materials in the automotive industry. *Metals Science and Heat Treatment*, 44(9-10), 2002.

[5] Norsk Hydro ASA. Why aluminium - physical properties.
Available at http://www.hydro.com/en/About-aluminium/Why-aluminium/Physical-properties/, January 2013.

[6] Oddvin Reiso. Extrusion and al metallurgy. Lecture notes in the course TMT4266 Metal Fabrication and Forming - Microstructure and Crystal Plasticity at NTNU, 2015.

[7] J. Lin, T.A. Dean, R.P. Garrett, and A.D. Foster. Process for forming metal alloy sheet components, 2008. British Patent vol. WO2008059242.

[8] Raufoss Technology. I-PAl project description. Internal document, March 2014.

[9] Ola Jensrud, Knut Erik Snilsberg, and Arne Kolbu. Press form hardening of high strength aluminium alloys, conceptual testing. Presented at the 9th Aluminium Two Thousand Congress and 5th International Conference ICEB, 2015.

[10] R. P. Garrett, J. Lin, and T. A. Dean. Solution heat treatment and cold die quenching in forming AA 6xxx sheet components: Feasibility study. *Advanced Materials Research*, 6-8: 673–680, May 2005-a.

[11] X. Fan, Z He, S. Yuan, and P. Lin. Investigation on strengthening of 6A02 aluminium alloy sheet in hot forming-quenching integrated process with warm forming-dies. *Material Science and Engineering: A*, 587:221–227, 2013-b.

[12] X. Fan, Z. He, S. Yuan, and K. Zheng. Experimental investigation of hot forming-quenching integrated process of 6A02ß aluminium alloy sheet. *Material Science and Engineering: A*, 573:154–160, 2013-a.

[13] S. Yuan, X. Fan, and Z. He. Hot forming-quenching integrated process with cold-hot dies for 2A12 aluminium alloy sheet. *Procedia Engineering*, 81:1780–1785, 2014.

[14] G. E. Dieter. *Mechanical Metallurgy*. McGraw-Hill Book Company (UK) Limited, SI metric edition, 1988.

[15] Lars Lodgaard. *Precipitation of dispersoids containing Mn and/or Cr in Al-Mg-Si-alloys*. PhD thesis, The Norwegian University of Science and Technology, 2000.

[16] Paul A Rometsch, Yong Zhang, and Steven Knight. Heat treatment of 7xxx series aluminium alloys - some recent developments. *Transactions of Nonferrous Metals Society China*, 34, 2014.

[17] William D. Callister, jr. *Materials Science and Engineering, An Introduction*. John Wiley & Sons, Inc, 7 edition, 2007.

[18] The Aluminium Association. Sheet & plate.
Available at http://www.aluminum.org/industries/processing/sheet-plate.

[19] J.R. Davis, J.R.D. Associates, and A.S.M.I.H. Committee. *Aluminum and Aluminum Alloys*. ASM specialty handbook. ASM International, 1993. ISBN 9780871704962.

[20] Ø. Ryen, O. Nijs, E. Sjölander, B. Holmedal, Hans-Erik Ekström, and E. Nes. Strengthening mechanisms in solid solution aluminum alloys. *Metallurgical and materials transactions A*, 37A, 2005.

[21] George E. Dieter, Howard A. Kuhn, and S. Lee Semiatin. *Handbook of Workability and Process Design.* ASM International, 2003.

[22] D.M. Stefanescu, editor. *Science and Engineering of Casting Solidification.* Kluwer Academic/Plenum Publisher, 2002.

[23] University of Cambridge. The effects of grain size on yield strength. Avaiable at http://www.doitpoms.ac.uk/tlplib/mechanical-testing/grainsize.php, 2004-2015.

[24] J. Dennis, P. S. Bate, and F. J. Humphreys. Abnormal grain growth in metals. *Materials Science Forum*, 558-559:717–722, 2007.

[25] B. Verlinden, J. Driver, I. Samajdar, and D. Roger, editors. *Thermo-Mechanical Processing of Metallic Materials.* Pergamon Materials Series. Pergamon, 2015.

[26] M. Hatherly and W. B. Hutchinson. *An introduction to texture in metals.* Institution of Metallurgists (Great Britain), 1979.

[27] F. J. Humphreys and M. Hatherly. *Recrystallization and Related Annealing Phenomena.* Elsevier Ltd, 2 edition, 2004.

[28] Hugh J. McQueen and W. J. McGregor Tegart. The deformation of metals at high temperatures. *Scientific American*, 232(4):116–125, 1975.

[29] G. E. Totten and D. S. Mackenzie, editors. *Handbook of Aluminium*, volume 1: Physical Metallurgy and Processes. CRC Press, 2003.

[30] The Free Dictionary By Farlex. Dislocations. http://encyclopedia2.thefreedictionary.com/Dislocations. Obtained 13.12.2015., 2015.

[31] S. L. Semiatin and J. J. Jonas. *Formability & Workability of Metals: Plastic instability & flow localization.* American Society for Metals, 1984.

[32] T. H. Courtney. *Mechanical Behavior of Materials*. The McGraw-Hill Companies, Inc., 2 edition, 2000.

[33] Bjørn Holmedal. Lecture notes from the course TMT4266 at NTNU. Published on Itslearning during the course, 2015.

[34] Brian Taylor. *Metalworking: Sheet Forming*, volume 14B. ASM International, 2006.

[35] Edward M. Mielnik. *Metalworking Science and Engineering*. McGraw-Hill Book Company, 1991.

[36] Z. Marciniak, J. L. Duncan, and S.J. Hu. *Mechanics of Sheet Metal Forming*. Butterworth Heinemann, 2002.

[37] E. Romhanji, M. Dudukovska, and D. Glišić. The effect of temperature on strain-rate sensitivity in high strength Al-Mg alloy sheet. *Journal of Materials Processing Technology*, 125-126:193–198, 2002.

[38] Raufoss Technology. Raufoss technology standard materials. Internal document, 02 2015.

[39] Jan Ketil Solberg. Teknologiske metaller og legeringer. Lecture Compendium, Norwegian University of Science and Technology, 2011.

[40] G.A. Edwards, K. Stiller, G.L. Dunlop, and M.J. Couper. The precipitation sequence in Al-Mg-Si alloys. *Acta Materialia*, 46(11):3893 – 3904, 1998.

[41] C. D. Marioara, S. J. Andersen, J. Jansen, and H. W. Zandbergen. Atomic model for GP-zones in a 6082 Al-Mg-Si system. *Acta Materialia*, 49(2):321–328, 2001.

[42] S. J. Andersen, H. W. Zandbergen, J. Jansen, C. Træholt, U. Tundal, and O. Reiso. The crystal structure of the β'' phase in Al-Mg-Si alloys. *Acta Materialia*, 46(9):3283–3298, 1998.

[43] X. Fang, M. Song, K. Li, and Y. Du. Precipitation sequence of an aged Al-Mg-Si alloy. *Journal of Mining and Metallurgy*, 46(2):171–180, 2010.

[44] R. Vissers, M. A. van Huis, J. Jansen, H. W. Zandbergen, C. D. Marioara, and S. J. Andersen. The crystal structure of the β' phase in Al-Mg-Si alloys. *Acta Materialia*, 55:3815–3823, 2007.

[45] Iris De Graeve and Jürgen Hirsch. Alloying. Published on www.aluminium.matter.org.uk by the European Aluminium Association and MATTER (The University of Liverpool), 2001-2010.

[46] Raufoss Technology. PressFormHardening materials. Internal document, 01 2016.

[47] Iris De Graeve and Jürgen Hirsch. 7xxx series alloys.
Published on www.aluminium.matter.org.uk by the European Aluminium Association and MATTER (The University of Liverpool), 2001-2010.

[48] X. Fang, Y. Du, M. Song, K. Li, and C. Jiang. Effects of cu content on the precipitation process of Al-Zn-Mg alloys. *Journal of Materials Science*, 47:8174–8187, 2012.

[49] Park D. S. and Nam S. W. On the characteristics of mn dispersoid in al-zn-mg alloys. *Journal of Materials Science Letters*, 13:716–718, 1994.

[50] H. C. Fang, K. H. Chen, L. P. Huang, G. S. Peng, and B. Y. Huang. Effect of zr, cr and pr additions on microstructures and properties of ultra-high strength Al-Zn-Mg-Cu alloys. *Materials Science and Engineering: A*, 528:7606–7615, 2011.

[51] Terje Iveland. Aksiell temperaturfordeling i standard rund strekkstav. Personal communication, e-mail recieved 11.03.2016.

[52] Synnøve Krog. Press form hardening of aluminium. TMT4500 Specialization Project, Department of Materials Science and Engineering, NTNU. Internal report, 12 2015.

[53] Dynamic Systems Inc. Gleeble 3500 system.
Available at http://gleeble.com/products/gleeble-3500.html, 2015.

[54] T. Furu T. Børvik O. S. Hopperstad I. Westermann, K. O. Pedersen. Effects of particles and solutes on strength, work-hardening and ductile fracture of aluminium alloys. *Mechanics of Materials*, 79:58–72, 2014.

[55] X. Fan, Z. He, W. Zhou, and S. Yuan. Formability and strengthening mechanism of solution heat treated Al-Mg-Si alloy sheet under hot stamping conditions. *Journal of Materials Processing Technology*, 228:179–185, 2016.

[56] Professor II Ola Jensrud. Personal communication, 2016.

[57] F. Roters, D. Raabe, and H. Weiland. Roughening of coated aluminium sheets during plastic straining. *Materials Science Forum*, 519-521:711–716, 2006.

[58] K. Teichmann, C. D. Marioara, S. J. Andersen, K. O. Pederesen, S. Gulbrandsen-Dahl, M. Kolar, R. Holmestad, and K. Marthinsen. Hrtem study of the effect of deformation on the early precipitation behaviour in an AA6060 Al-Mg-Si alloy. *Philosophical Magazine*, 2011.

[59] M. Kolar, K. Pedersen, S. Gulbrandsen-Dahl, and K. Marthinsen. Combined effect of deformation and artificial aging on mechanical properties of Al-Mg-Si alloy. *Transactions of Nonferrous Metals Society China*, 22(1824-1830), 2012.

[60] Raufoss Technology. Candidate alloys february 15. Internal document.